

**ELECTROMECHANICAL CHARACTERIZATION OF ORGANIC FIELD-  
EFFECT TRANSISTORS WITH GENERALIZED SOLID-STATE AND  
FRACTIONAL DRIFT-DIFFUSION MODELS**

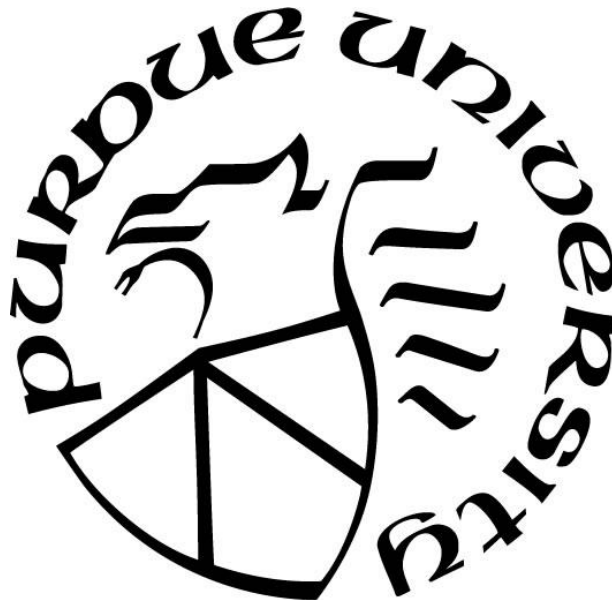
by  
**Yi Yang**

**A Dissertation**

*Submitted to the Faculty of Purdue University*

*In Partial Fulfillment of the Requirements for the degree of*

**Doctor of Philosophy**



School of Engineering Technology

West Lafayette, Indiana

May 2021

**THE PURDUE UNIVERSITY GRADUATE SCHOOL**  
**STATEMENT OF COMMITTEE APPROVAL**

**Dr. Haiyan Zhang, Co-Chair**

School of Engineering Technology

**Dr. Richard Voyles, Co-Chair**

School of Engineering Technology

**Dr. Robert Nawrocki, Committee Member**

School of Engineering Technology

**Dr. Xiumin Diao, Committee Member**

School of Engineering Technology

**Dr. Lizhe Tan, Committee Member**

School of Electrical and Computer Engineering, Purdue Northwest

**Approved by:**

Dr. Kathyne Newton

*I dedicate this dissertation to my parents for their love and support throughout my life.*

## **ACKNOWLEDGMENTS**

First of all, I would like to express my sincere and heartfelt gratitude to my co-advisors, co-chairs of my Ph.D. committee, Dr. Haiyan H. Zhang and Dr. Richard M. Voyles, for their extraordinary advising, strong supports and constant encouragement.

I would also like to extend my gratitude to my committee members, Dr. Robert Nawrocki, Dr. Xiumin Diao, Dr. Lizhe Tan for their selfless helps and valuable suggestions in my research. I also want to thank all my fellow colleagues and staff members in the department, especially, Dr. Kathryne Newton, Dr. Duane Dunlap, Dr. Xin Ma, Dr. Hao Xiong, Mr. Mochen Li, Mr. Siming Ma, Ms. Niedra Mcleland, Ms. Amanda Wilson, Ms. Debbie Hulsey, and Ms. Felicia Anderson for their helps and kindness.

Special thanks should also be given to National Science Foundation (USA) under grant CNS-1726865 and US Department of Agriculture under grant 2019-67021-28990 for providing partial financial support for my research.

## TABLE OF CONTENTS

LIST OF TABLES .....	8
LIST OF FIGURES .....	9
LIST OF ABBREVIATIONS .....	13
ABSTRACT.....	15
CHAPTER 1. INTRODUCTION .....	16
1.1 Problem Statement .....	16
1.2 Significance.....	16
1.3 Research Question .....	18
1.4 Scope.....	18
1.5 Assumptions.....	20
1.6 Limitation.....	20
1.7 Delimitation .....	21
1.8 Dissertation Layout.....	21
CHAPTER 2. REVIEW OF LITERATURE .....	22
2.1 Overview of OFETs.....	22
2.1.1 Layouts of OFETs.....	22
2.1.2 Electromechanical Modeling of OFETs .....	24
2.1.2.1 Mechanical Characterization of TFTs .....	24
2.1.2.2 Electrical Characterization of Undeformed OFETs .....	26
2.1.2.3 Electromechanical Characterization of Deformable OFETs .....	33
2.2 Overview of Fractional Calculus Theory.....	39
2.2.1 Definitions of Fractional Operators .....	40
2.2.2 Caputo's Linear Fractional Differential Equation .....	42
2.2.3 Approximations of Fractional Integral and Fractional Derivatives .....	43
2.3 Summary .....	45
CHAPTER 3. RESEARCH METHODOLOGY .....	46
3.1 Study of Strained TFT Based on Mass-Spring-Damper Model .....	46
3.1.1 Derivation of Finite Element Model.....	46
3.1.2 Derivation of 1D Mass-Spring-Damper Model .....	48

3.1.3	Derivation of 2D Mass-Spring-Damper Model .....	50
3.1.4	Strain-Induced Electrical characteristics of the ZnO TFT .....	52
3.1.4.1	Strain Effects on Carrier Transport Mobility .....	53
3.1.4.2	Strain Effects on Threshold Voltage .....	55
3.1.4.3	Post-Stress Dynamics of ZnO TFT .....	57
3.2	Study of Bendable OFETs Based on Generalized Solid State Model .....	58
3.2.1	Geometry and Band Structure of OFETs.....	58
3.2.2	Carrier Density and Surface Potential Modeling.....	60
3.2.3	Field-Effect Mobility Model.....	63
3.2.4	Generalized Current-Voltage Equations.....	65
3.2.5	Electromechanical Coupling Model .....	67
3.3	Study of Strained OSC Devices Based on Fractional Drift-Diffusion Model .....	69
3.3.1	Derivation of the Computational Scheme.....	70
3.3.1.1	Discretization of Transient-State Fr-DD Model .....	71
3.3.1.2	Discretization of Steady-State Fr-DD Model .....	77
3.3.1.3	Special Case When $\alpha = 1$ and $\beta = 1$ .....	78
3.3.2	Consistency and Convergence Analysis .....	79
3.3.2.1	Consistency of the Computational Scheme .....	79
3.3.2.2	Convergence of the Computational Scheme .....	81
3.3.3	Study of Strain Effects on the Fractional Parameters .....	82
3.4	Summary .....	84
CHAPTER 4. RESULTS AND DISCUSSION .....		86
4.1	Study of Strained TFT Based on Mass-Spring-Damper Model .....	86
4.1.1	Simulation Setup.....	87
4.1.2	Comparison of FEA and MSD Models .....	92
4.1.3	Strain-Induced Shifts of Mobility and Threshold Voltage .....	94
4.1.4	Strain Effects on ZnO-TFT Characteristics .....	97
4.2	Study of Bendable OFETs Based on Generalized Solid-State Model.....	100
4.2.1	Simulation Setup.....	101
4.2.2	Surface Potentials .....	103
4.2.3	Overall Effective Mobility .....	104

4.2.4	Electrostatic Potentials, Current Flows and Hole Concentration .....	105
4.2.5	Tuning of Model Parameters .....	107
4.2.6	Comparison of Pre-bent and Post-bent OFET Characteristics .....	108
4.3	Study of Strained OSC Devices Based on Fractional Drift-Diffusion Model .....	111
4.3.1	Numerical Examples.....	111
4.3.2	Experimental Validation of the Fr-DD Model for Pre-bent OFET .....	119
4.3.3	Experimental Validation of the Fr-DD Model for Post-bent OFET .....	123
4.4	Summary .....	125
CHAPTER 5. CONCLUSION AND FUTURE WORK .....		127
5.1	Contribution .....	127
5.2	Recommendations .....	128
REFERENCES .....		130
PUBLICATIONS.....		149

## LIST OF TABLES

Table 3.1. Dilation and uniaxial (shear) deformation potentials for Si, Ge and ZnO. For the same deformation potential, values extracted from different literatures may vary from each other due to different doping conditions and calculation errors. ....	57
Table 4.1. Material properties and layer thickness for different material layers (Y. Yang et al., 2020). ....	87
Table 4.2. The MSD parameters of the PET layer under different MSD sizes (assume damping ratio $\zeta = 0.005$ ) (Y. Yang et al., 2020). ....	90
Table 4.3. Mesh sizes and simulation results of the FEA model under five groups of meshes (Y. Yang et al., 2020). ....	92
Table 4.4. The strain-free parameters of ZnO (Siddiqui, 2012). ....	96
Table 4.5. Fitted model parameters and basic material properties for the generalized solid-state model (Y. Yang et al., 2021a). ....	102
Table 4.6. The errors, numerical convergence order in time and CPU time under different temporal step sizes $\tau$ with fixed spatial step size $\Delta x = 0.01$ and fixed space-derivative order $\beta = 1$ (Y. Yang et al., 2021b). ....	113
Table 4.7. The errors, numerical convergence order in time and CPU time under different temporal step sizes $\tau$ with fixed spatial step size $\Delta x = 0.01$ and fixed time-derivative order $\alpha = 1$ (Y. Yang et al., 2021b). ....	114
Table 4.8. The errors, numerical convergence order in space and CPU time under different spatial step sizes $\Delta x$ with fixed temporal step size $\tau = 1e - 5$ and fixed space-derivative order $\beta = 1$ (Y. Yang et al., 2021b). ....	114
Table 4.9. The errors, numerical convergence order in space and CPU time under different spatial step sizes $\Delta x$ with fixed temporal step size $\tau = 1e - 5$ and fixed time-derivative order $\alpha = 1$ (Y. Yang et al., 2021b). ....	114
Table 4.10. The model parameters utilized for Example 4.2 (Y. Yang et al., 2021b). ....	116
Table 4.11. The model parameters utilized for Example 4.3 (Y. Yang et al., 2021b). ....	118



## LIST OF FIGURES

Figure 1.1 Bendable, stretchable and conformable biosensors are made possible as the conventional medical devices become thinner and miniaturized (H. Lee et al., 2016; Son et al., 2014). .....	17
Figure 1.2 Importance of transistors in the implementation of real-world ideas, the variations on the electrical outputs of transistors due to mechanical deformations can be reflected in the overall performance of the high-level circuits. ....	19
Figure 1.3 Comparison of single crystalline, polycrystalline and amorphous materials, inorganic semiconductors are mainly crystalline materials, and organic semiconductors can be polycrystalline or amorphous materials ( <i>Crystalline and Amorphous Solids: Explanation, Differences.</i> , 2021). ....	20
Figure 2.1 Four most commonly used configurations of OFETs. ....	23
Figure 2.2 The second naming convention for the four most commonly used configurations of OFETs (Y. Yang et al., 2021a). ....	24
Figure 2.3 A schematic energy diagram of OSCs with acceptor-like, donor-like shallow trap states and the deep trap states, the holes and electrons can be captured into or de-captured from the trap sites and transported between the lowest unoccupied molecule orbital (LUMO) and the highest occupied molecule orbital (HOMO) via multi-step hopping. ....	27
Figure 2.4 (a) Chemical formula of RR-P3HT, and (b) chemical formula of RRa-P3HT (Muntasir & Chaudhary, 2015). ....	32
Figure 2.5 Number of publications related to the research of flexible electronics (right-side y axis), piezoresistive effects (left-side y axis of the inset plot), modeling of strained effects in flexible electronics (left-side y axis), and the modeling of piezoresistive effects in flexible electronics (left-side y axis of the inset plot). The data were collected from Web of Science. (Heidari et al., 2017). ....	33
Figure 2.6 (a) Splitting mechanisms of the bonding and anti-bonding energy levels for a diatomic molecule; (b) Shifting of the Silicon bandgap under hydrostatic strain, negative strain means compressive stress applied and positive strain means tensile stress applied (Sun et al., 2010). ....	36
Figure 2.7 Band splitting diagrams for Si, Ge and GaAs when a uniaxial compressive stress is present with un-strained band denoted by “n.s.”, energy shifts due to hydrostatic strain denoted by “h.s.”, and energy splitting due to shear strain denoted by “s.s.” (Sun et al., 2010). ....	37
Figure 3.1 The schematic representation of the one-dimensional MSD model, the cellular unit is composed of a mass center, an ideal spring and an ideal damper (Y. Yang et al., 2020). ....	48
Figure 3.2 The schematic representation of a 2D MSD model (left) with its inclusion made of type-1 material and its external two layers filled by type-2 material, the cellular unit (right) is composed of a mass center, four bidirectional springs and four bidirectional dampers (Y. Yang et al., 2020). ....	50

Figure 3.3 A widely used fabrication layout of a $\langle 001 \rangle$ wafer plane, with channel current flow $J$ and the average stress $\sigma$ (Y. Yang et al., 2020).	53
Figure 3.4 (a) Simplified band structure of a p-type ISC with ionized donors (red) and ionized acceptors (blue); (b) of a p-type OSC with deep and shallow trap states with the density of states at energy level $E$ denoted by $N(E)$ (Y. Yang et al., 2021a).	60
Figure 3.5 The anatomy of a TCBG OFET with coordinate system positioning along the semiconductor-dielectric interface, the red portion is the accumulation layer for charge carrier transport between drain and source electrodes (Y. Yang et al., 2021a).	62
Figure 3.6 An illustration of the discretized (a) electron continuity equation with electron concentration denoted by $n_{i,jk}$ , $x$ -component of electron current density denoted by $IX_{i-1/2,jk}$ , and $y$ -component of electron current density denoted by $IY_{i,j-1/2k}$ ; (b) hole continuity equation with hole concentration denoted by $p_{i,jk}$ , $x$ -component of hole current density denoted by $JX_{i-1/2,jk}$ , and $y$ -component of hole current density denoted by $JY_{i,j-1/2k}$ (Y. Yang et al., 2021b).	70
Figure 3.7 An illustration of strain-dependent $\beta$ value under different $h$ values, the negative $\varepsilon$ indicates that the channel is under compression, the positive $\varepsilon$ means that the channel is under extension, $\varepsilon_{max} = -0.2$ , $\beta_a = 0.4$ and $\beta_b = 0.72$ in this example.	84
Figure 4.1 Schematics of the structure and material types for an encapsulated TFT, the active (semiconductor) layer is ZnO (Y. Yang et al., 2020).	86
Figure 4.2 The inverted staggered TFT under two types of external loadings, surface tension and normal vibration can be considered as two major sources of boundary excitation when the TFT is attached to the surface of human or animal skin (the top and bottom encapsulating layers are not shown) (Y. Yang et al., 2020).	87
Figure 4.3 (a) Stress distribution in the TFT under symmetric tensile stress at the skin-substrate interface (in MPa); (b) Stress distributions in the TFT with vibrational excitations at the skin-substrate interface (in MPa) (Y. Yang et al., 2020).	89
Figure 4.4 The mesh plots (left) generated by COMSOL and its corresponding stress distributions (right) in the longitudinal direction (Y. Yang et al., 2020).	91
Figure 4.5 The total displacement of the ZnO TFT from FEA model (Y. Yang et al., 2020).	92
Figure 4.6 The total displacement fields simulated via 14 MSD models of different sizes ranging from $44 \times 36$ to $616 \times 504$ (Y. Yang et al., 2020).	93
Figure 4.7 The linear relationship between stress and displacement for ZnO, the stress is positive (negative) when the channel is under tension (compression) (Y. Yang et al., 2020).	95
Figure 4.8 The average longitudinal stress (y axis to the left) and average transversal stress (y axis to the right) obtained by MSD models with different sizes (Y. Yang et al., 2020).	95
Figure 4.9 The strain-induced shifts on the carrier mobility (y axis to the left) and the threshold voltage (y axis to the right) in an inverted staggered ZnO TFT when it is under a sinusoidal vibrational boundary excitation (Y. Yang et al., 2020).	96

Figure 4.10 The transconductance curves of the ZnO-TFT under a sinusoidal boundary excitation, the transconductance is evaluated at $t=0.005\sim 0.015s$ , which is half a period of the boundary excitation (Y. Yang et al., 2020).....	97
Figure 4.11 The curves of drain current shifts with gate-source voltage at different moments within a boundary excitation cycle, the drain current shifts are evaluated at $t=0.005\sim 0.015s$ (Y. Yang et al., 2020).....	98
Figure 4.12 The output curves of the ZnO-TFT under a sinusoidal boundary excitation, the transconductance is evaluated at $t=0.005\sim 0.015s$ (Y. Yang et al., 2020).....	98
Figure 4.13 The curves of drain current shifts with drain-source voltage at different moments within a boundary excitation cycle, the drain current shifts are evaluated at $t=0.005\sim 0.015s$ (Y. Yang et al., 2020).....	99
Figure 4.14 The surface electric field varies as a function of surface potential (y axis to the left), and the gate-source voltage varies as functions of surface potential when the flab-band voltage is fixed to different values (y axis to the right) (Y. Yang et al., 2021a).....	103
Figure 4.15 The overall effective (field-effect) mobility (after considering multiple scattering effects) of DNTT as a function of the effective electric field when the density of trap states is fixed to different values (Y. Yang et al., 2021a). ....	104
Figure 4.16 The contour plot of the electrostatic potentials when the OFET is working under applied bias $V_{ds} = -1.5\text{ V}$ and $V_{gs} = -3\text{ V}$ (Y. Yang et al., 2021a). ....	105
Figure 4.17 The contour plot of the current flowlines with the accumulation layer for carrier transport when the OFET is working under applied bias $V_{ds} = -1.5\text{ V}$ and $V_{gs} = -3\text{ V}$ (Y. Yang et al., 2021a). ....	106
Figure 4.18 The contour plot of the hole concentration when the OFET is working under applied bias $V_{ds} = -1.5\text{ V}$ and $V_{gs} = -3\text{ V}$ (Y. Yang et al., 2021a). ....	106
Figure 4.19 Drain current versus gate-source voltage (transconductance) characteristic curves under different $\gamma$ values, the curve with $\gamma = 1.3$ has the best agreement with the experimental data (Y. Yang et al., 2021a). ....	107
Figure 4.20 Drain current versus drain-source voltage (output) characteristic curves under different $\gamma$ values, the curve with $\gamma = 1.3$ has the best agreement with the experimental data (Y. Yang et al., 2021a). ....	108
Figure 4.21 Comparison of the theoretically predicted ( $\gamma = 1.3$ ) and experimentally measured (symbols) drain current as a function of gate-source voltage (the transconductance curves) for fixed $V_{ds} = -5\text{ V}$ , both the pre-bent and post-bent cases are illustrated (Y. Yang et al., 2021a). ....	109
Figure 4.22 Comparison of the theoretically predicted ( $\gamma = 1.3$ ) and experimentally measured (symbols) drain current as a function of drain-source voltage (black lines) for fixed $V_{gs} = 0, -1, -2, -3, -4, -5\text{ V}$ , only the pre-bent case is illustrated (Y. Yang et al., 2021a). ....	110

Figure 4.23 Comparison of the theoretically predicted ( $\gamma = 1.3$ ) and experimentally measured (symbols) drain current as a function of drain-source voltage (black lines) for fixed $V_{gs} = 0, -1, -2, -3, -4, -5$ V, only the post-bent case is illustrated (Y. Yang et al., 2021a).....	110
Figure 4.24 The contour plots (top) and surface plots (bottom) for the electrostatic potentials $\varphi$ (left) and the electron concentration $n$ (right) at $t=0.02$ s (Y. Yang et al., 2021b).....	113
Figure 4.25 The geometry of a 2D top-contact bottom-gate (TCBG) OFET with the active layer made from a p-type organic semiconductor (Y. Yang et al., 2021b).....	115
Figure 4.26 The simulated electrostatic potentials and hole concentration in the OFET for space-derivative order $\beta = 1$ and $\beta = 0.8$ (Y. Yang et al., 2021b). ....	117
Figure 4.27 The simulated transient-state electrostatic potentials and hole concentration in the solar cell when (a) space-derivative order $\beta = 1$ is fixed and $\alpha = 0.8, 0.6$ and $0.4$ , respectively; (b) time-derivative order $\alpha = 0.9$ is fixed and $\beta = 1, 0.8$ and $0.6$ , respectively (Y. Yang et al., 2021b). ....	119
Figure 4.28 The solution domain of a 2D top-contact bottom-gate (TCBG) OFET device composed of a p-type organic semiconductor layer, a dielectric layer and encapsulating layers (top and bottom) (Y. Yang et al., 2021b).....	120
Figure 4.29 (a) The experimentally measured transconductance at a fixed $V_{ds} = -5$ V compared with the fitted theoretical transconductance curve obtained from the Fr-DD model; (b) The adjusted pre-bent $\beta$ values ( $\beta b$ ) under different $V_{gs}$ and a fixed $V_{ds} = -5$ V (Y. Yang et al., 2021b). ....	121
Figure 4.30 (a) The experimentally measured output curve (symbols) at a series of fixed $V_{gs} = -5 \sim -2$ V compared with the fitted theoretical output curve (black solid lines) obtained from the Fr-DD model; (b) The adjusted pre-bent $\beta$ values ( $\beta b$ ) under different $V_{ds}$ and a group of fixed $V_{gs} = -5 \sim -2$ V (Y. Yang et al., 2021b). ....	122
Figure 4.31 (a) The experimentally measured transconductance at a fixed $V_{ds} = -5$ V compared with the fitted theoretical transconductance curve obtained from the Fr-DD model; (b) The adjusted post-bent $\beta$ values ( $\beta \varepsilon$ ) under different $V_{gs}$ and a fixed $V_{ds} = -5$ V.....	122
Figure 4.32 (a) The experimentally characterized post-bent $\beta \varepsilon$ as a function of the pre-bent $\beta b$ (red stars), the solid curve is obtained by fitting Equation (3.131) to the experimental data; (b) The relationship curve for the fitted Equation (3.131) when strain-free (pre-bent) $\beta b = 0.78$ .	123
Figure 4.33 (a) The experimentally measured output curves (symbols) at a series of fixed $V_{gs} = -5 \sim -2$ V compared with the theoretically predicted output curves (black solid lines) obtained from the Fr-DD model; (b) The cross-validated post-bent $\beta$ values ( $\beta \varepsilon$ ) under different $V_{ds}$ and a group of fixed $V_{gs} = -5 \sim -2$ V obtained by applying Equation (3.131) to the adjusted pre-bent $\beta$ values ( $\beta b$ ).....	124

## LIST OF ABBREVIATIONS

ABBREVIATION	TERM
<b>TFT</b>	Thin Film Transistor
<b>OFET</b>	Organic Field Effect Transistor
<b>FET</b>	Field Effect Transistor
<b>MOSFET</b>	Metal-Oxide-Semiconductor Field Effect Transistor
<b>CMOS</b>	Complementary Metal Oxide Semiconductor
<b>OECT</b>	Organic Electrochemical Transistor
<b>ISC</b>	Inorganic Semiconductor
<b>OSC</b>	Organic Semiconductor
<b>MSD</b>	Mass-Spring-Damper
<b>MS</b>	Metal-Semiconductor
<b>Fr-DD</b>	Fractional Drift-Diffusion
<b>FEA</b>	Finite Element Analysis
<b>DFT</b>	Density Functional Theory
<b>Fr-PDEs</b>	Fractional Partial Differential Equations
<b>R2R</b>	Roll-to-Roll
<b>IoT</b>	Internet of Things
<b>EDA</b>	Electronic Design Automation
<b>BCTG</b>	Bottom-Contact Top-Gate
<b>BCBG</b>	Bottom-Contact Bottom-Gate
<b>TCTG</b>	Top-Contact Top-Gate
<b>TCBG</b>	Top-Contact Bottom-Gate
<b>PVD</b>	Physical Vapor Deposition

<b>CVD</b>	Chemical Vapor Deposition
<b>GIXRD</b>	X-Ray Diffraction
<b>SPDE</b>	Stochastic Partial Differential Equation
<b>DD</b>	Drift-Diffusion
<b>PDEs</b>	Partial Differential Equations
<b>LUMO</b>	Lowest Unoccupied Molecular Orbital
<b>HOMO</b>	Highest Occupied Molecular Orbital
<b>P3HT</b>	poly(3-hexylthiophene)
<b>RR-P3HT</b>	regio-regular poly(3-hexylthiophene)
<b>TIPS-P</b>	6,13-bis(triisopropylsilylethynyl) pentacene
<b>PDMS</b>	polydimethylsiloxane
<b>DNTT</b>	dinaphtho[2,3b:2',3'-f]thieno[3,2-b]thiophene
<b>RL</b>	Riemann-Liouville
<b>DoS</b>	Density of States
<b>TA</b>	Tail-Level Acceptor-Like
<b>TD</b>	Tail-Level Donor-Like
<b>GA</b>	Deep-Level Acceptor-Like
<b>GD</b>	Deep-Level Donor-Like
<b>PF</b>	Poole-Frenkel
<b>CT</b>	Caughey-Thomas
<b>PET</b>	Polyethylene terephthalate
<b>ITO</b>	Indium Tin Oxide
<b>PNP</b>	Poisson-Nernst-Planck

## ABSTRACT

The miniaturization and thinning of wearable, soft robotics and medical devices are soon to require higher performance modeling as the physical flexibility causes direct impacts on the electrical characteristics of the circuit – changing its behavior. As a representative flexible electronic component, the organic field effect transistor (OFET) has attracted much attention in its manufacturing as well as applications. However, as the strain and stress effects are integrated into multi-physics modelers with deeper interactions, the computational complexity and accuracy of OFET modeling is resurfacing as a limiting bottleneck.

The dissertation was organized into three interrelated studies. In the first study, the Mass-Spring-Damper (MSD) model for an inverted staggered thin film transistor (TFT) was proposed to investigate the TFT's internal stress/strain fields, and the strain effects on the overall characteristics of the TFT. A comparison study with the finite element analysis (FEA) model shows that the MSD model can reduce memory usage and raises the computational convergence speed for rendering the same results as the FEA. The second study developed the generalized solid-state model by incorporating the density of trap states in the band structure of organic semiconductors (OSCs). The introduction of trap states allows the generalized solid-state model to describe the electrical characteristics of both inorganic TFTs and organic field-effect transistors (OFETs). It is revealed through experimental verification that the generalized solid-state model can accurately characterize the bending induced electrical properties of an OFET in the linear and saturation regimes. The third study aims to model the transient and steady-state dynamics of an arbitrary organic semiconductor device under mechanical strain. In this study, the fractional drift-diffusion (Fr-DD) model and its computational scheme with high accuracy and high convergence rate were proposed. Based on simulation and experimental validation, the transconductance and output characteristics of a bendable OFET were found to be well determined by the Fr-DD model not only in the linear and saturation regimes, but also in the subthreshold regime.

# CHAPTER 1. INTRODUCTION

Flexible electronics are seen as the next electronics frontiers, and theoretical understanding of the influence of mechanical deformation on the performance of electronics can influence design strategy in both academic and commercial settings. The study aims to develop high-fidelity modeling approaches to characterize the pre- and post-stress characteristics of the OFETs. Chapter one presented the statement of the problem that motivates this study, and it also covered the discussions on the significance, scope, assumptions, limitations, and delimitations of this study.

## 1.1 Problem Statement

Flexible electronics is becoming more commonplace as wearables, soft robotics and medical devices become more mainstream. As shown in Figure 1.1, the miniaturization and thinning of health monitoring electronic equipment can provide more intimate, comfortable, and continuous medical diagnosis and reduce the cost of treatment via the use of flexible electronics. Since the thin-film flexible electronics demonstrates great conformability to human skins, the flexible electronics faces challenges for maintaining its own electronic performance under constant stretching and bending etc. Research on the subject has been mostly restricted to experimental characterization of a flexible device. The experimental characterization usually requires researchers to collect a huge amount of experimental data, preprocess the data, extract features from the data collection and analyze the post-processed data using statistical tools. However, these approaches based on statistics and empirical formulas are either redundant and costly or lack of reflection of the devices' physical nature. So far, attention has been rarely paid to the theoretical and physical modeling of the electrical characteristics of flexible electronics in presence of the strain effects, and this study focuses on this part.

## 1.2 Significance

The exciting new applications of flexible electronics range from thin-film display technologies for consumer electronics, wearable transducers that promote health monitoring, implantable electronics to enhance medical diagnosis and treatment, to improving the operational



efficiency of unmanned aerial vehicles and robots through insubstantial and flexible energy scavenging devices and sensors (Corzo et al., 2020). These different application scenarios reflect the special significance of flexible electronics compared to conventional (rigid) electronics, that is to maintain device performance and reliability no matter what types of mechanical deformation happen, such as bending and rolling of microchips in large scale photovoltaic devices, laminating biosensors onto the nonuniform cell surface, bending, warping, and stretching of encapsulated OFET required for electronic skins (Schischke et al., 2020).

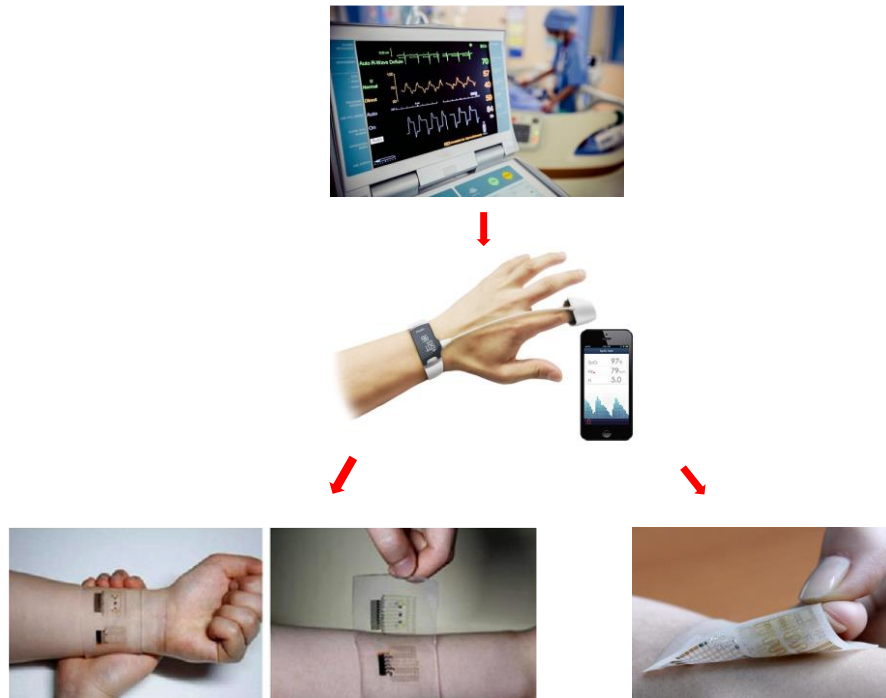


Figure 1.1 Bendable, stretchable and conformable biosensors are made possible as the conventional medical devices become thinner and miniaturized (H. Lee et al., 2016; Son et al., 2014).

The values of the global market for the flexible electronics were estimated around \$23.64 billion in 2019, and this number is expected to attain \$42.48 billion by 2030s (Corzo et al., 2020; Humbare et al., 2020). The flexible electronics market share can increase rapidly within the expected time frame due to the spreading of Internet of Things (IoT) technologies. Moreover, the growth of the market for implantable and intelligent electronic devices can further boost the market growth for flexible electronics. Because of these factors, it is forecast that the market of flexible electronics will experience exponential growth in the short term (Humbare et al., 2020).

Flexible electronics must have the capability of enduring mechanical deformations and at the same time preventing their electronic performance from impairing by internal stress (Harris et al., 2016). Modeling of flexible electronics is state-of-the-art research full of challenges and uncertainties. Scientific research conducted on flexible electronic modeling can shorten the design and manufacturing process of flexible electronics, thereby remarkably lowering the research expenditure of flexible electronics and accelerating the marketization of flexible electronics.

### 1.3 Research Question

This study addressed the challenges in the electromechanical characterization of OFETs through its modeling, simulation and experimental verification. The uniqueness of the approaches used in this study is that the conventional solid-state physics theories for inorganic semiconductors (ISCs) were generalized to organic polymers, and new mathematical tools, such as fractional partial differential equations (Fr-PDEs) were utilized to explore the transient and steady-state dynamics of any-type OSC devices. The research questions of this study are (a) Which modifications should be added to the energy diagram to reflect the structural disorder of OSCs? (b) How does the channel strain affect the electronic properties of OFETs? (c) Is there a physical model that can uniformly describe the pre- and post-strain dynamics of OSC devices? (d) What are the advantages of the new models over existing models?

### 1.4 Scope

The scope of this research is limited to the electromechanical modeling of organic field effect transistors since OFET has its own significance and broader impact from solid state physics, digital design through programming and acts as the fundamental component of a general flexible circuitry. As shown in Figure 1.2, the transistor is essentially playing a central role in the implementation of real-world ideas. All electronics are based on transistors, which is the most complicated device (compared to diodes, capacitors, resistors, etc.). A transistor is a semiconductor device for switching electronic signals or amplifying electrical power, and it is a basic building block of digital gates. Very small changes in the stress/strain distribution within the transistor may give rise to significant shifts of the overall output performance of the flexible

circuit. By integrating the stress/strain-induced changes in the electrical properties of transistors into some established circuit analysis software, such as Protel, OrCAD, PSPICE etc., researchers can effectively analyze and predict the overall performance variations of flexible circuits under mechanical deformation. Therefore, rather than studying the effect of mechanical deformation on the high-level flexible circuit, this study focuses on the electromechanical modelling of deformable transistors.

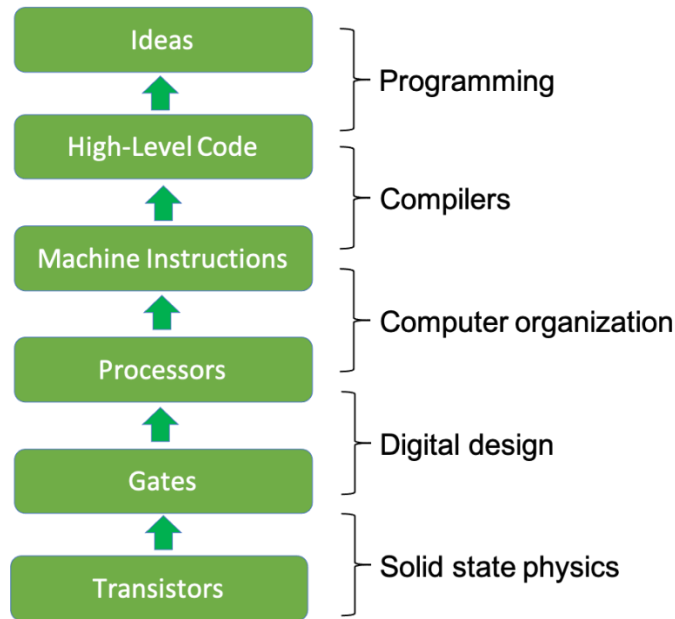


Figure 1.2 Importance of transistors in the implementation of real-world ideas, the variations on the electrical outputs of transistors due to mechanical deformations can be reflected in the overall performance of the high-level circuits.

In addition, this study attaches its emphasis on OFETs instead of (inorganic) FETs since many aspects and behaviors of the charge carriers in the active organic semiconductors are still unrevealing. Organic semiconductors often exist in polycrystalline or amorphous forms. The main difference among (single) crystalline, polycrystalline and amorphous solids is the length scale to maintain the translational symmetry (a.k.a., periodicity or long-range order) of atomic structures. As shown in Figure 1.3, the atomic structure repeats periodicity across its whole volume in single crystalline solids. Polycrystalline solids have smaller grains, each grain can be thought of as a single crystal, so the polycrystalline only repeats its periodicity across each grain. The amorphous solids have no periodicity at all. Instead of solving the chemical properties of a

specific type of OSC material by resorting to density functional theory (DFT) or other computational quantum chemistry approaches, this study developed novel approaches to solve for generalized solid-state physical properties of the OFETs. Moreover, this study did not involve molecular dynamics simulation which is usually computationally intensive and not applicable for general transistor modeling.

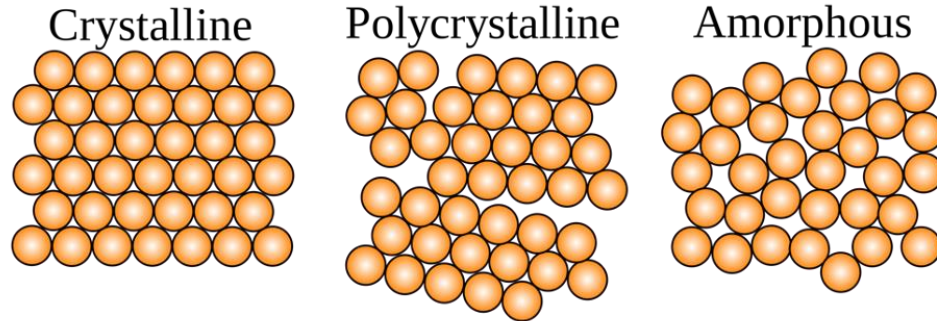


Figure 1.3 Comparison of single crystalline, polycrystalline and amorphous materials, inorganic semiconductors are mainly crystalline materials, and organic semiconductors can be polycrystalline or amorphous materials (*Crystalline and Amorphous Solids: Explanation, Differences.*, 2021).

### 1.5 Assumptions

The following assumptions were inherent to the study:

- The out-of-plane dimension is taken unity in two-dimensional (2D) models.
- Unless otherwise stated, all materials used in mechanical and electrical simulations are considered to be homogeneous.
- The gradual channel approximation is assumed in the generalized solid-state model.
- Unless specifically mentioned, the metal-semiconductor (MS) contacts are assumed to be ohmic.

### 1.6 Limitation

The following limitations were considered in this study:

- The electro-mechanical coupling relationships in the generalized solid-state model are limited to strained ISCs (e.g., Silicon.).

### 1.7 Delimitation

The study was conducted with the following delimitations:

- The electro-mechanical coupling relationships were derived from strained semiconductor theory (Yongke Sun et al., 2010). Utilizing the electro-mechanical coupling relationships to explain the strain effects (e.g., bending effects) on the mobility of ISCs was validated through experiments in many literatures (Bradley et al., 2001; Heidari et al., 2017; Lim et al., 2004; Wacker et al., 2011). Nevertheless, my research explored, for the first time, the applicability of these relationships for OSCs.

### 1.8 Dissertation Layout

The dissertation was organized into five chapters. The dissertation began with an introduction of the problem statement, significance, research question, scope, limitation and delimitation of this study in chapter one. Chapter two reviewed relevant literatures in the fields of OFET fabrication, layout and electromechanical modeling. In chapter three, the research methodology and framework were presented and discussed in detail. Three novel electromechanical models were proposed to explore the electrical characterization of OFETs or TFTs due to mechanical deformation in three interrelated studies. Chapter four provided the results and discussions of these three studies. The conclusions and recommendations were presented in chapter five.

## CHAPTER 2. REVIEW OF LITERATURE

This chapter reviewed the literature that is relevant to the fabrication, layouts, and electromechanical modelling approaches for OFETs. The basics of fractional calculus theory and deformation potential theory that are pertinent to model derivations were also summarized in this chapter.

### 2.1 Overview of OFETs

An OFET is a thin film transistor (TFT) based on polymers as semiconductors. Over the last few decades, OFETs have very quickly become a popular research topic, due to their wide range of applications in engineering and technology, such as the fabrication of stretchable and biocompatible transducers or actuators (Dimitrakopoulos & Malenfant, 2002; Dimitrakopoulos & Mascaró, 2001; Ebisawa et al., 1983; Garnier et al., 1990; Horowitz, 1998, 2004; Lin et al., 1997; Rogers et al., 2001; Zhu et al., 2019). The OFETs' rapid development is committed at achieving different applications from the silicon-based transistors, and at the same time lowering the cost of economical electronics by replacing inorganic semiconductors with potentially cheap organic alternatives (Root et al., 2017). Another benefit of OFETs, in contrast to inorganic TFTs, is their unparalleled physical flexibility (Kaltenbrunner et al., 2013; M. H. Lee et al., 2013; Nawrocki, 2019; Zhang et al., 2015), which enables the fabrication of imperceptible, ultra-flexible electronic skins (Nawrocki et al., 2016), chemically sensitive sensors (H. Li et al., 2019), and bioelectronic recording device for cardiomyocytes (Kyndiah et al., 2020). There are multiple approaches to fabricate OFETs, such as physical vapor deposition of small molecules, polymer solution casting, roll-to-roll (R2R) processing and mechanical lamination of a peeled layer of single-crystalline organics onto a substrate (Chang et al., 2017). The choice of fabrication method and the ease of the fabrication process are closely relevant to the layout of the OFET.

#### 2.1.1 Layouts of OFETs

As a fundamental and representative component in flexible circuitry, the OFET has gained much attention in its fabrications as well as usages. The OFET is mainly constituted by

three terminal electrodes (source, drain and gate), as well as two polymeric layers, namely the dielectric and semiconductor layers. In its general structures, the source and drain electrodes are placed on the two sides of the semiconductor, while the gate electrode is separated from the semiconductor layer by the dielectric insulator.

Four commonly used layouts exist for OFETs. As shown in Figure 2.1, the OFET is staggered when the gate island and the source/drain islands are positioned on the opposite sides of the semiconductor layer, and the OFET is coplanar if they are placed on the same side. In addition, if the gate island is deposited on the bottom layer of the dielectric insulator, the OFET is configured in an inverted layout (Nan, 2013).

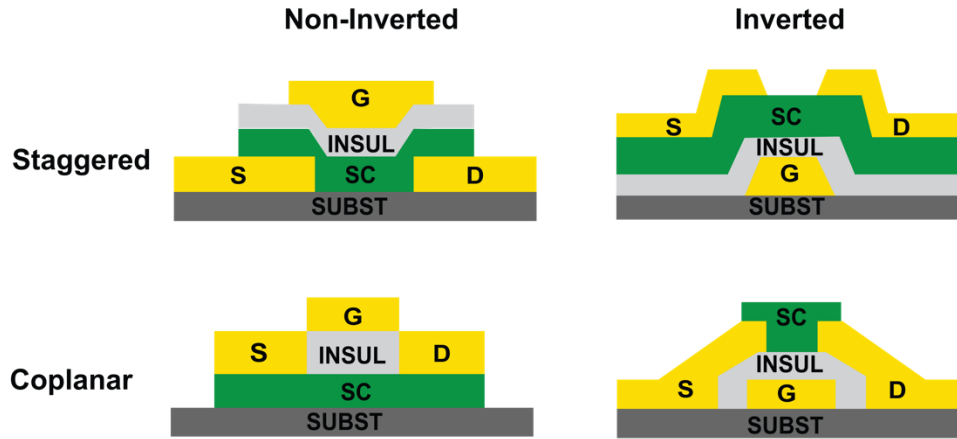


Figure 2.1 Four most commonly used configurations of OFETs.

Over the past decades, most research in OFETs has taken another naming convention for OFET layouts. As shown in Figure 2.2, OFETs can be grouped into four types: the bottom contact/top gate (BCTG), bottom contact/bottom gate (BCBG), top contact/bottom gate (TCBG) structures, and top contact/top gate (TCTG) structures. The choice of the OFET manufacturing layout is often affected by fabrication and environment conditions, such as the temperatures, humidity, availability of solvents and chemicals, as well as the interfacial reactions of individual layers (Nawrocki et al., 2016). And also, for a given device, everything being the same except for the location of electrodes vis-à-vis OSC (e.g., TCBG vs BCBG DNTT OFET), there can be more than one order of magnitude difference for the drain current  $I_d$ . Among these four configurations, the TCBG OFET showed enhanced output performance over the other OFET configurations in the effective carrier mobility and the  $I_{on}/I_{off}$  ratio (Vidor et al., 2016), and it

has also played an significant role in the development of multiphysics modelers and the understanding of associated fabrication limitations for flexible electronics. Therefore, the interest of my study was placed in the mechanical, electrical and electromechanical characterization of TCBG OFETs. However, it should be mentioned that the modeling approaches proposed in my work are also applicable to the other three OFET configurations.

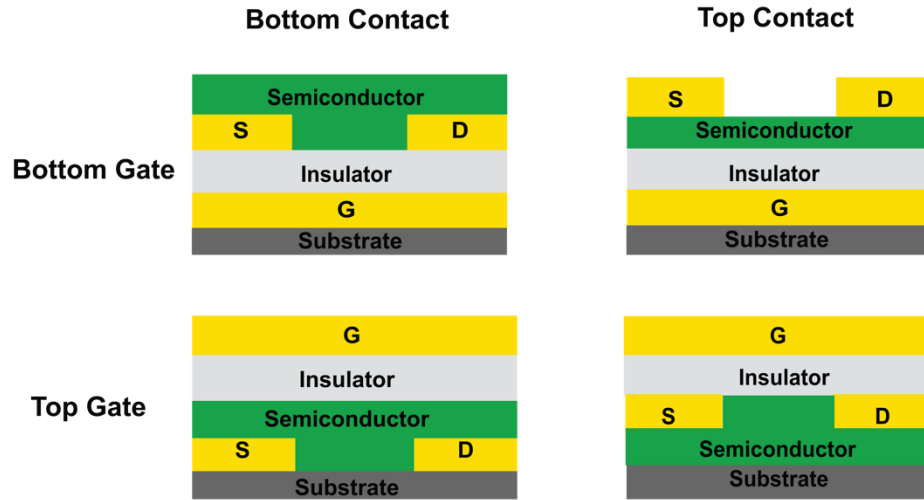


Figure 2.2 The second naming convention for the four most commonly used configurations of OFETs (Y. Yang et al., 2021a).

## 2.1.2 Electromechanical Modeling of OFETs

A precise and rapid gauge of OFET-based circuit performance is required by physically flexible organic electronics' commercial deployment in the process of electronic design automation (EDA), but exploring the OFET's analytic model is a continuing concern within the semiconductor industry. This section presented literature reviews relevant to modeling approaches utilized in the mechanical characterization of TFTs, the electrical characterization of undeformed OFETs and the electromechanical characterization of deformable OFETs.

### 2.1.2.1 Mechanical Characterization of TFTs

Several experimental techniques have been developed for the measurement of mechanical stress in TFTs (Gunda et al., 2017). The fabrication methods, such as chemical vapor deposition (CVD) and physical vapor deposition (PVD), can result in residual stresses in the thin films, and



the external loadings (e.g., stretching, compressing, twisting, and bending) are the major sources of loading stresses in the thin-film electronics. Both types of stresses are present in flexible electronics and the experimental measurements of them are essentially the same. However, since the magnitude of residual stresses is much smaller than loading stresses, the measurement of residual stresses requires a higher resolution of the measuring tool. The measurement methods can be divided into two main categories: the mechanical approaches (curvature-based measurement) and the optical approaches (x-ray diffraction and interferometry). In the curvature-based methods, Stoney's equation (See Equation (2.1)) can be utilized to evaluate the average mechanical stress  $\sigma_f$  in the thin film deposited on a much thicker substrate ( $t_f/t_s < 0.1$ ) (Feng et al., 2007).

$$\sigma_f = \frac{E_s t_s^2 K}{6 t_f (1 - \nu_s)} \quad (2.1)$$

where  $E_s$  is the Young's modulus of the substrate,  $t_s, t_f$  is the thickness of substrate and thin film, respectively,  $K$  is the curvature (the inverse of radius of curvature), and  $\nu_s$  is the Poisson ratio of the substrate. The x-ray diffraction method depends on x-rays and electron beams with high resolution to measure the residual stresses in the thin film (Noyan et al., 1987a, 1987b). Other stress-measurement approaches such as the traditional  $\sin^2 \Psi$  method and grazing incidence x-ray diffraction (GIXRD) geometry have similar working principles as the x-ray diffraction method (Kovalchuk et al., 1995; Lomov et al., 2000), and it is acknowledged that these optical-diffraction-based methods are the most commonly used non-destructive approaches for experimentally approximating the residual stresses in the thin films (Gunda et al., 2017). The interferometry approach is also an optical approach, but it utilizes a modified Stoney's equation to evaluate the mechanical stresses in the thin film deposited onto a flexible substrate (H. C. Chen et al., 2012). The test methods described so far are only capable of providing a measurement of the average mechanical stresses. For the full-field stresses measurement, experimental techniques based on the digital photoelasticity and thermoelasticity have been explored for flexible electronics and bulk materials, respectively (Jayamohan & Mujeeb, 2003; Wong et al., 1988). The photoelasticity-based method measures the optical retardations of the thin films before and after the mechanical deformations and then quantifies the stress field by applying the photoelastic equation (Y. C. Lee et al., 2012). The thermoelasticity-based approach exploits the coupling of mechanical deformation and thermal energy changes in elastic materials,

thus the changing rate of the principal stress sum can be directly related to the changing rate of temperature in a dynamically loaded body (Wong et al., 1988). Other efforts to measure the distributed mechanical stresses in multi-stacked thin films via strain gauges are also found in several literatures (Brown, 2007; Lynch, 1995; Quintero et al., 2006).

In addition to experimental measurement methods, the theoretical predictions of TFTs' internal stress/strain distributions based on numerical simulations are available as well. For instance, the stochastic partial differential equation (SPDE), which is a conventional method to predict the random stock market movements, has been utilized in simulating the deposition of thin films (Hu, Orkoulas, & Christofides, 2009; Ni & Christofides, 2005). Several effective and comprehensive thin-film models are directly established by a group of SPDEs, such as Kardar-Parsi-Zhang model, Edwards-Wilkinson model and ballistic deposition model. By considering the relaxation of the deposition surface in these SPDE models, the prediction accuracy of the optical reflectivity, the printed surface roughness, physical porosity of the thin films, and electrical conductivity can be improved (Forgerini & Marchiori, 2014). Besides the SPDE model, the solid mechanics model was also established and the solution can be obtained through finite element analysis (FEA) (Nan, 2013; Weinan & Lu, 2014). However, the SPDE model and the solid mechanics FEA model lack the ability to characterize important electrical properties of TFTs, such as charge carrier mobility, and the threshold voltage. Therefore, in addition to the mechanical properties of TFTs, it is also of great interest to study and explore the electrical properties of TFTs.

#### ***2.1.2.2 Electrical Characterization of Undeformed OFETs***

A substantial quantity of literature has been published on undeformed OFETs' modeling. Initial analysis of OFETs depended on inorganic MOSFET models derived from the square-law theory or the bulk charge theory (Alam et al., 1997; Fadlallah et al., 2007; Locci et al., 2008; Meixner et al., 2008; Necliudov et al., 2000; Pierret, 1996). However, MOSFET models cannot accurately characterize intricate OFET behaviors, for example determining the carrier mobility  $\mu$  and the threshold voltage  $V_{th}$ , because the effects such as trap states nor the intrinsic difference between inorganic MOSFETs and OFETs are not incorporated into the MOSFET models. It was indicated that the OFETs' carrier mobility extracted from the standard MOSFET equations is substantially overestimated (Bittle et al., 2016; Hamilton et al., 2004; Horowitz, 2009).

Investigating the transport properties of OSCs is meaningful for the normal operation of OFETs. The modeling of charge carrier transport behaviors in such organic materials is a specific problem, since, unlike the ISCs, the smooth transition of agitated charge carriers (electrons or holes) between the conduction band and the valence band is achieved by carriers' hopping between many localized trap states that are randomly distributed across the energy gap (Kaushik et al., 2016). As shown in Figure 2.3, the probability of a carrier being captured or released by a localized state is determined by the position and distribution density of the localized state in the energy gap. For example, electrons are more likely to be captured (released) in an acceptor-type (donor-type) localized state near the edge of the band gap, and holes are more likely to be trapped (detrapped) in a donor-type (acceptor-type) localized states near the band edges. Former researchers have explored the effects of trap states on the compact modeling of OFETs.

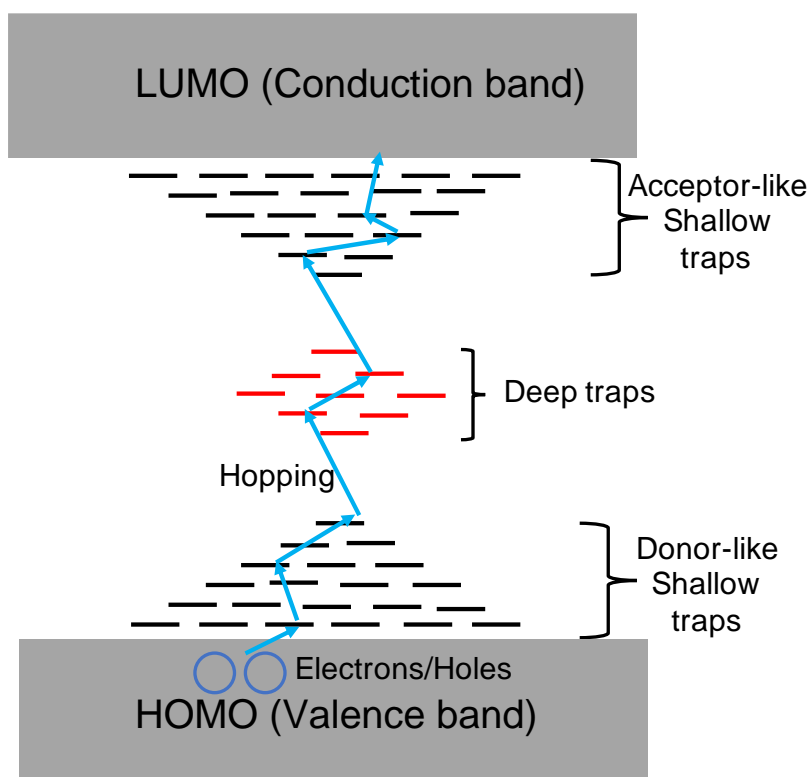


Figure 2.3 A schematic energy diagram of OSCs with acceptor-like, donor-like shallow trap states and the deep trap states, the holes and electrons can be captured into or de-captured from the trap sites and transported between the lowest unoccupied molecule orbital (LUMO) and the highest occupied molecule orbital (HOMO) via multi-step hopping.

For example, the finite element analysis (FEA) based program was developed in EDA software (e.g., Silvaco) to solve the carrier continuity equations with trap effects (Gupta et al., 2008). In a later work, a Matlab based analytical model that considers trap states in the OSCs was also developed, and it was shown that both the Matlab and FEA models display a sound agreement with reported experimental measurements (Wondmagegn & Pieper, 2009). Until now, multiple OFET models that involves trap states have been proposed, including the variable-range hopping transport model with double exponentially distributed trap states (L. Li et al., 2010), the HiSIM-Org model based on surface potentials (Maiti et al., 2014), the compact OFET models with variable density of trap states and channel length (Ana & Din, 2018; Ana & Najeeb-ud-Din, 2019), the UOFET model based on low-voltage Pentacene (Dwivedi et al., 2019), and the experimental measurements of trap state density in OSCs (Grünewald et al., 1980; Kalb & Batlogg, 2010). Provided with the high precision of trap density models in the characterization of OFET's electrical properties, a generalized OFET's transconductance and output characteristics that reflect the density of trap states and a unified description of field effect transistors' current-voltage equations are still largely missing. As one of my significant contributions to the OFETs' modeling, the generalized and unified current-voltage equations to characterize transconductance and outputs of OFETs were derived by me for the first time and these equations are suitable for OFETs made from different OSCs and fabricated in different configurations. In addition, the generalized current-voltage equations are applicable to both inorganic and organic field effect transistors (FETs), including ISC-TFTs, OFETs and MOSFETs, and it can reasonably reflect the difference in the concentration of trap states in OSCs and ISCs.

With the square-law theory and the bulk charge theory, only the drifting motion of charge carriers is considered in the modeling of transconductance and output characteristics of OFETs. However, for OFETs with short or medium channel length, the diffusive movement of carriers in response to concentration gradients will be a source of current that cannot be ignored. A good OFET model should account for both the diffusive and the drifting movement of carriers (Pierret, 1996). The unified description of the carriers' diffusive and drifting movement in ISCs is achieved via a group of coupled partial differential equations (PDEs), which can be established by applying Gauss' law to the electrical potential  $\varphi$ , and the continuity of the electron and hole current densities,  $J_n$  and  $J_p$ , respectively (Bank et al., 1983; Gartland, 1993). Besides modeling of ISCs, this system of coupled PDEs, forming the so called drift-diffusion (DD) model, has also

found its extensive applications in the modeling of many diffusion-reaction processes, such as ion exchanges in the electrochemical solvents (Lu & Zhou, 2011; Q. Zheng et al., 2011), and the transports of positive/negative particles within cell membranes (Bolintineanu et al., 2009; Pods et al., 2013). Depending on different application scenarios, the DD model can have various representation forms. In the Van Roosbroeck representation of the DD model, the current density equation can be augmented by Einstein's relation, which gives a fixed proportional relationship between the diffusion coefficients  $D_p$ ,  $D_n$  and the drift mobilities  $\mu_p$ ,  $\mu_n$  (Van Roosbroeck, 1950). To maintain its convention, the Van Roosbroeck representation of the DD model can be expressed in a closed-form as Equations (2.2)-(2.4),

$$-\Delta(\varepsilon_0 \varepsilon_r \varphi) = q(p - n + N_D^+ - N_A^-) \quad (2.2)$$

$$\frac{\partial n}{\partial t} = \frac{1}{q} \nabla \cdot J_n + G_n \quad (2.3)$$

$$\frac{\partial p}{\partial t} = -\frac{1}{q} \nabla \cdot J_p + G_p \quad (2.4)$$

where current density functions are given by  $J_n = -q\mu_n n \nabla \varphi + qD_n \nabla n$  and  $J_p = -q\mu_p p \nabla \varphi - qD_p \nabla p$ , Einstein's relations are  $\frac{D_n}{\mu_n} = \frac{D_p}{\mu_p} = V_T = \frac{kT}{q}$ ,  $V_T$  is the thermal voltage,  $k$  is the Boltzmann constant,  $T$  is the thermal temperature,  $q$  is the charge of an electron,  $\varepsilon_0$  is dielectric permittivity of vacuum,  $\varepsilon_r$  is the relative dielectric permittivity of the semiconductor,  $N_D^+$  and  $N_A^-$  are ionized donor and acceptor concentrations.  $G_n$  and  $G_p$  are the net generation-recombination rates for electrons and holes, respectively. Previous research data collected from Silicon/Germanium test experiments have revealed the effectiveness of the DD model for modeling the charge carrier transports in ISCs (Gupta et al., 2008). In the past several decades, plentiful numerical algorithms have been developed for solving Equations (2.2)-(2.4), including the finite element method (Tan et al., 1989), finite difference fractional step method (Yuan, 2005), mixed finite volume and modified upwind fractional difference method (Yuan et al., 2017), and monotone iterative method based on the adaptive finite element discretization (Chen & Liu, 2003; Li, 2007), etc. All of those numerical methods have one thing in common: an efficient iterative method, e.g., Newton's iteration, Gauss-Seidel iteration, or Gummel's iteration was utilized to decouple Equations (2.2)-(2.4). Among these iteration methods, Gummel's approach is generally more effective than other methods due to its flexibility in finding its initial guess and customizing the update formulas to improve the convergence and computational performance.

Moreover, the effectiveness, stability and convergence of Gummel's decoupling method and iteration for its application to DD simulations were also thoroughly and rigorously proved by mathematicians (Jerome, 1985, 1996; Jerome & Kerkhoven, 1991; Kerkhoven, 1988).

However, recent research revealed that the conventional (integer-order) DD model may not be able to characterize the charge carrier transports in OSCs, evident from the long-tail behavior of the photocurrent curve observed in OSCs (Sibatov & Uchaikin, 2009). Based on the DD model, Tsekov (2018) showed that the mean squared displacement (MSD) of the carrier trajectory should be proportional to its diffusion time, i.e.,  $E(x^2(t)) \propto t$ . However, the long-tail behavior of the photocurrent curve observed in OSCs implies that the MSD in this scenario is given by  $E(x^2(t)) \propto t^\alpha$ , for  $\alpha$  termed as the dispersive parameter of the OSC,  $0 < \alpha < 1$ , depending on the temperature and band structure disorders (Choo et al., 2017; Kniepert et al., 2011; Mozer et al., 2005; Scher & Montroll, 1975). This long-tail photocurrent phenomenon was first observed by time-of-flight measurements (Orenstein & Kastner, 1981), and the mechanism that underpins the dispersive carrier transports can be precisely explained by the “multiple trapping model” (Scher & Montroll, 1975; Tiedje & Rose, 1981), the “single trapping model” (Antoniadis & Schiff, 1991) and the “hopping model” (Ela & Afifi, 1979; Liu et al., 2017; Upreti et al., 2019), respectively. Relying on the “multiple trapping model”, the mobile carriers in OSCs can be classified as free (delocalized) charge carriers  $p_f, n_f$  and trap (localized) charge carriers  $p_t, n_t$ . The free charge carrier is the carrier that can hop freely between two localized trap centers and the trap charge carrier is the carrier that is permanently captured by a localized trap center. Sibatov & Uchaikin (2007) proved that the free hole density and the trap hole density in the p-type OSCs have a relationship as given in Equation (2.5),

$$\frac{\partial p_t(x, t)}{\partial t} = \frac{1}{\tau_0 c^\alpha} {}^{RL}\mathcal{D}_t^\alpha(p_f(x, t)) = \frac{1}{\tau_0 c^\alpha} \frac{1}{\Gamma(1-\alpha)} \frac{\partial}{\partial t} \int_0^t \frac{p_f(x, s)}{(t-s)^\alpha} ds \quad (2.5)$$

where  ${}^{RL}\mathcal{D}_t^\alpha$  is Riemann-Liouville (RL) fractional derivative of order  $0 < \alpha < 1$ ,  $\tau_0$  is the mean time of delocalization (expected free time for a free carrier moving between two entrapments),  $c$  is the charge carrier capture coefficient defined as  $c = \omega_0 [\sin(\pi\alpha) / \pi\alpha]^\alpha$ ,  $\omega_0$  is the capture rate of the trap charge carriers, and  $\alpha = kT/E_0$  is the dispersive parameter depending on the temperature  $T$  and the expected (mean) value of the exponential density of trap states  $E_0$ . The 1D

continuity equation for free charge carriers in p-type OSCs was also derived by Sibatov & Uchaikin (2007) as Equation (2.6),

$$\begin{aligned} \frac{\partial p_f(x, t)}{\partial t} + \frac{1}{\tau_0 c^\alpha} {}^{RL}\mathcal{D}_t^\alpha(p_f(x, t)) + \frac{\partial}{\partial x} [\mu_p E(x, t) p_f(x, t)] - D_p \frac{\partial^2 p_f(x, t)}{\partial x^2} \\ = p(x, 0) \delta(t) \end{aligned} \quad (2.6)$$

where  $E(x, t) = -\frac{\partial \varphi(x, t)}{\partial x}$  is the intensity of the electric field in the 1D domain, and  $p(x, 0)\delta(t)$  is the initial charge carriers agitated by impacting of photon beams. Consider that  $p = p_f + p_t$  and  $p_t \gg p_f$  in OSCs, substituting Equation (2.5) into Equation (2.6) can produce the continuity equation for total charge carrier density, as given by

$${}^{RL}\mathcal{D}_t^\alpha(p(x, t)) + \frac{\partial}{\partial x} [F_\alpha(x, t) p(x, t)] - D_\alpha \frac{\partial^2 p(x, t)}{\partial x^2} = p(x, 0) \frac{t^{-\alpha}}{\Gamma(1 - \alpha)} \quad (2.7)$$

where  $F_\alpha(x, t) = \tau_0 c^\alpha \mu_p E(x, t)$  is the anomalous advection coefficient and  $D_\alpha = \tau_0 c^\alpha D_p$  is the anomalous diffusion coefficient. The hole mobility  $\mu_p$  and hole diffusion coefficient  $D_p$  satisfy the Einstein relations. Equation (2.7) coupled with the 1D Poisson equation forms the 1D fractional drift-diffusion (Fr-DD) model. A discretization scheme, which discretizes the time-fractional derivative with backward finite difference method and the integer-order spatial derivatives with finite center difference method, was proposed to solve the 1D Fr-DD model (Choo et al., 2017; Choo & Muniandy, 2015). Choo et al. (2017) showed that the photocurrent curves obtained from the 1D Fr-DD model are in good agreement with the recorded transient photocurrents from regio-random OSCs poly(3-hexylthiophene) (RRa-P3HT) and regio-regular poly(3-hexylthiophene) (RR-P3HT). RRa-P3HT and RR-P3HT are two OSCs with their structures compared in Figure 2.4. In addition, Alaria et al. (2019) introduced the fractional reduced differential transform method to solve the 1D Fr-DD model and also suggested the existence of a general-form Fr-DD model with both time derivative and spatial derivatives fractionalized. The (general-form) Fr-DD model is described by a group of coupled fractional-order PDEs as presented in Equations (2.8)-(2.10),

$$-\Delta(\varepsilon_0 \varepsilon_r \varphi) = q(p - n) \quad (2.8)$$

$${}^C\mathcal{D}_t^\alpha(n(x, y, z, t)) = \frac{1}{q} \nabla \cdot I + G_n \quad (2.9)$$

$${}^C\mathcal{D}_t^\alpha(p(x, y, z, t)) = -\frac{1}{q} \nabla \cdot J + G_p \quad (2.10)$$

where  ${}^C_0\mathcal{D}_t^\alpha$  is the Caputo's time-fractional derivative of order  $0 < \alpha \leq 1$ , the fractional-order electron current density  $I$  and hole current density  $J$  are given by  $I = -q\mu_n n \nabla \varphi + qD_n {}^C\nabla_r^\beta n$  and  $J = -q\mu_p p \nabla \varphi - qD_p {}^C\nabla_r^\beta p$ , and  ${}^C\nabla_r^\beta = ({}^C_0\mathcal{D}_x^\beta \quad {}^C_0\mathcal{D}_y^\beta \quad {}^C_0\mathcal{D}_z^\beta)$  is the Caputo's fractional gradient operator of order  $0 < \beta \leq 1$  in 3D. Since the OSCs are typically treated as intrinsic materials without dopants, the ionized donors  $N_D^+$  and acceptors  $N_A^-$  can be omitted in Poisson's equation (Dev Dhar Dwivedi et al., 2020).

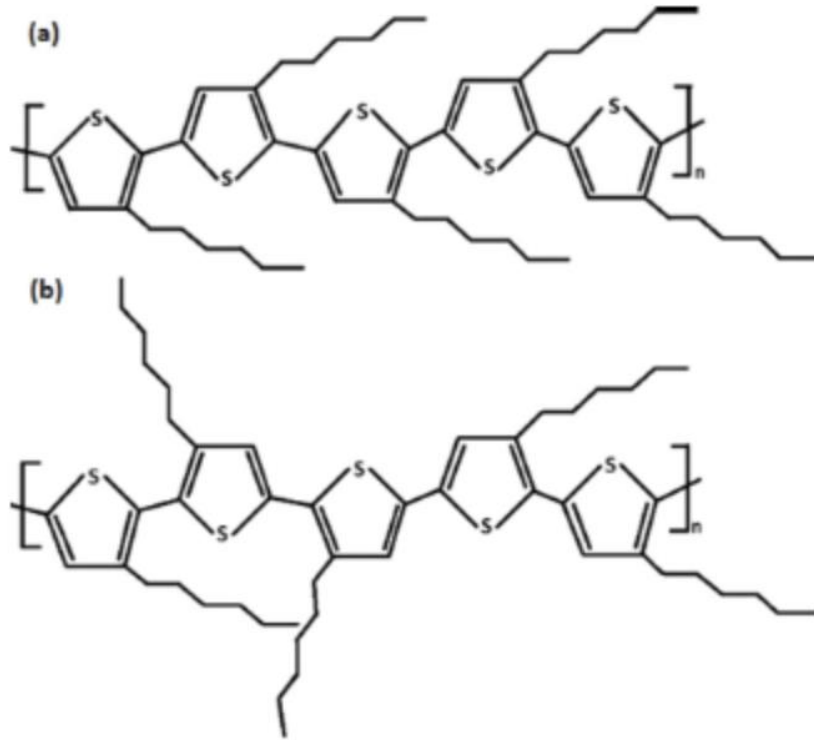


Figure 2.4 (a) Chemical formula of RR-P3HT, and (b) chemical formula of RRa-P3HT (Muntasir & Chaudhary, 2015).

As the Fr-DD model emerges as a useful tool for understanding the dispersive transport behavior of charge carriers in OSCs, investigating how to solve it is instrumental for predicting the steady-state and transient electrical responses of OSC devices, such as OFETs. Up to now, far too little attention has been paid to the development of a general Fr-DD model solver. The solver development for the Fr-DD model is very important since the fractional dynamics of devices made from irregular crystalline semiconductors cannot be revealed without a high-fidelity model solver. Although a certain number of studies have been carried out on developing



the solvers for the conventional (integer-order) DD model, the resulting DD model solvers often have low accuracy and high computational complexity. As one of major contributions of this dissertation, a solver with high accuracy and computational performance for the Fr-DD model was developed to predict the transient and steady-state dynamics of any kind of OSC devices. In particular, the transconductance and output characteristics of OFETs are the focus of attention and the shifts of its electrical properties under mechanical deformation can be predicted by the Fr-DD model.

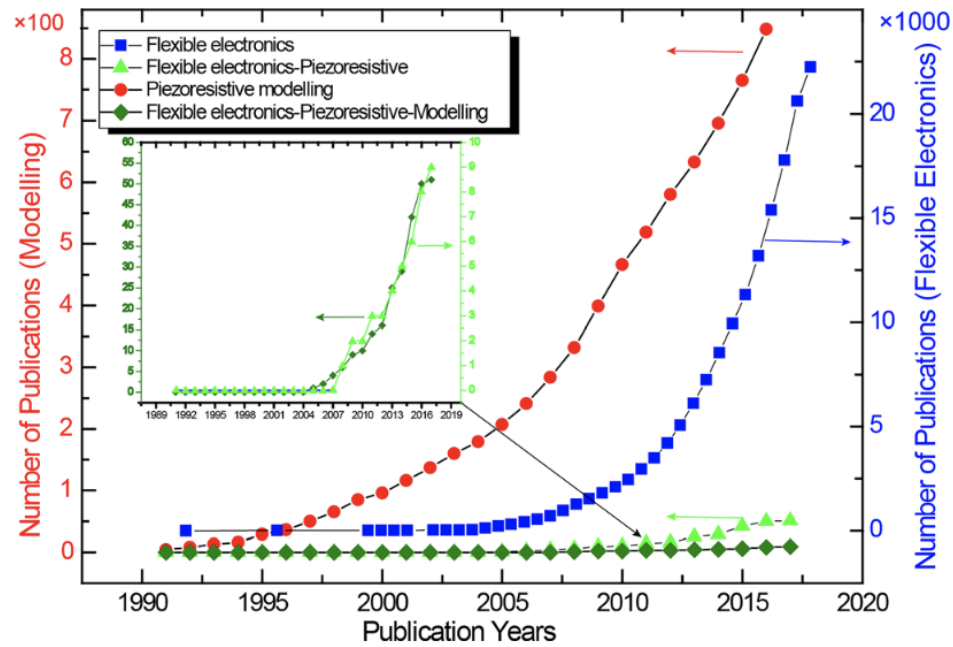


Figure 2.5 Number of publications related to the research of flexible electronics (right-side y axis), piezoresistive effects (left-side y axis of the inset plot), modeling of strained effects in flexible electronics (left-side y axis), and the modeling of piezoresistive effects in flexible electronics (left-side y axis of the inset plot). The data were collected from Web of Science. (Heidari et al., 2017).

### 2.1.2.3 Electromechanical Characterization of Deformable OFETs

Strain is an important concept in engineering physics. Process-induced strain was an original feature added to the silicon devices and its significant role in feature enhanced CMOS technology has received much attention in semiconductor industry (Sun et al., 2010). Prior to the strain technology in logic electronics, the piezoresistive sensors utilizing the strain effects in

Silicon and Germanium were fabricated much earlier, circa 1950s (Mason & Thurston, 1957). In recent years, a strong driving force has been formed to study strain-induced effects in flexible electronics, especially TFTs, since the electronic properties of flexible circuits cannot only be altered by strains, similar to Silicon-based logic and piezoresistive sensors, but it may be desirable to utilize those deformations as part of the computational compilation process to improve the computations themselves. Figure 2.5 presents the historical perspective of the rapid growing interest in the field of flexible electronics based on the data collected from Web of Science. It can be observed from Figure 2.5 that the number of publications in the field of flexible electronics has grown exponentially since early 1990s and a significant portion of these publications was devoted to the modeling of flexible electronics. In this study, the modeling of deformable OFETs was emphasized.

For general TFTs and MOSFETs made from ISCs, the raised thickness, the bonding effects and inhomogeneity among distinct layers will affect the distribution of its strain fields, and thus will lead strain induced shifts of the electrical characteristics as well. Aiming to efficiently and accurately predict the strain induced electrical characteristics, much of the research endeavors were devoted to Silicon-based MOSFET models. For instance, Sheu (2007) fully studied the influence of layouts on Nano-scale MOSFETs' performance and developed a stress-dependent dopant diffusion model to carry out numerical simulations. Wacker *et al.* (2011) utilized the BSIM3v3 transistor model to simulate a DC circuit and explored the influence of variable uniaxial mechanical stress on the overall performance of CMOS transistors. Similarly, Alius *et al.* (2014) presented the linear relationship between the strained variations on electrical parameters and the mechanical stress, i.e.,  $\frac{\Delta(\text{parameter})}{\text{parameter}} = \text{sensitivity} \times \text{stress}$ , and he validated this linear relationship via a bent-chip experiment. In a follow-up study, a bendable MOS compact model was proposed by Heidari *et al.* (2016) and it was experimentally verified that the stress-related sensitivity coefficients for the carrier mobility and the threshold voltage are both equal to the modified piezoresistive coefficients of the doped Silicon (Heidari et al., 2016). This observation motivates the developments of more statistics and empirical models for electromechanical characterization of transistors, and a more detailed discussion on the modeling of bending-induced TFTs was also presented in literature (Heidari et al., 2017). Although these statistics models of the Silicon-based MOSFETs accurately emulated the quantitative relationships between strained variations on electrical properties and the mechanical

deformation, the characterization process of these models was complex and costly. In addition, these statistics and empirical models were each only capable of targeting MOSFETs made from a specific semiconductor material and were not generalizable to the electromechanical characterization of TFTs and OFETs made from a different type of semiconductors or configuration layouts.

To improve the efficiency of predicting TFTs' electromechanical characteristics, some researchers have turned their attention to the development of theoretical models that follow modern physics. One of the archetypes of theoretical formulations for strain-induced performance in TFTs and MOSFETs is the study showing improved electron mobilities of n-type (100) Si/Si<sub>1-x</sub>Gex multi-facet heterostructures and hole mobilities of p-type (100) Si/I-Si<sub>1-x</sub>Gex/Si twofold heterostructures in the 1980s (Manasevit et al., 1982; People et al., 1984). The enhanced mobility phenomenon observed in those MOSFETs with heterostructures was suspected to be caused by the lattice mismatch in the strained Silicon. Another notable example is the investigations on piezoresistive effect, which was first observed in strained Germanium and Silicon by Smith (1954). The primary method to predict the mobility enhancement and the piezoresistive effect in strained ISCs is the deformation potential theory (Bardeen & Shockley, 1950; Herring & Vogt, 1956). Deformation potential theory was first proposed by Bardeen & Shockley (1950) to study the interaction of electrons and acoustic phonons. The vibrations of acoustic phonon create local strains in the semiconductor and thus results in the induced shift of energy band edges. Based on deformation potential theory, the band shift and the strain are related by

$$\Delta E = \sum_{i,j} \Xi_{i,j} \varepsilon_{i,j} \quad (2.11)$$

where  $\Xi$  are deformation potentials, and  $\varepsilon$  is the strain in the semiconductor channel. The strain tensor  $\varepsilon$  can be decomposed into the hydrostatic component (Equation (2.12)) and the shear component (Equation (2.13)).

$$\bar{\varepsilon}_{hydrostatic} = \frac{1}{3} \begin{bmatrix} \varepsilon_{xx} + \varepsilon_{yy} + \varepsilon_{zz} & 0 & 0 \\ 0 & \varepsilon_{xx} + \varepsilon_{yy} + \varepsilon_{zz} & 0 \\ 0 & 0 & \varepsilon_{xx} + \varepsilon_{yy} + \varepsilon_{zz} \end{bmatrix} \quad (2.12)$$

$$\bar{\epsilon}_{shear} = \frac{1}{3} \begin{bmatrix} 2\epsilon_{xx} - (\epsilon_{yy} + \epsilon_{zz}) & 0 & 0 \\ 0 & 2\epsilon_{yy} - (\epsilon_{zz} + \epsilon_{xx}) & 0 \\ 0 & 0 & 2\epsilon_{zz} - (\epsilon_{xx} + \epsilon_{yy}) \end{bmatrix} + \begin{bmatrix} 0 & \epsilon_{xy} & \epsilon_{xz} \\ \epsilon_{yz} & 0 & \epsilon_{yz} \\ \epsilon_{zx} & \epsilon_{zy} & 0 \end{bmatrix} \quad (2.13)$$

Different types of strain have different effects on the energy band of a semiconductor (Sun et al., 2007). According to deformation potential theory, the hydrostatic strain cannot affect the band degeneracy lifting, but it leads to the shifting of bandgaps. Consider the formation of a diatomic molecule as shown in Figure 2.6(a), the interactions between two atoms are altered when they are pushed together or pulled apart from each other. Under the influence of hydrostatic strain, the increased interatomic interactions will cause the bonding and anti-bonding energy states to move further away from each other. Under normal circumstances, the bandgap widens when a compressive hydrostatic stress is applied, and the bandgap narrows when a tensile hydrostatic stress is applied. For instance, the bandgap dependence on hydrostatic strain for Silicon is presented in Figure 2.6(b) (Sun et al., 2010).

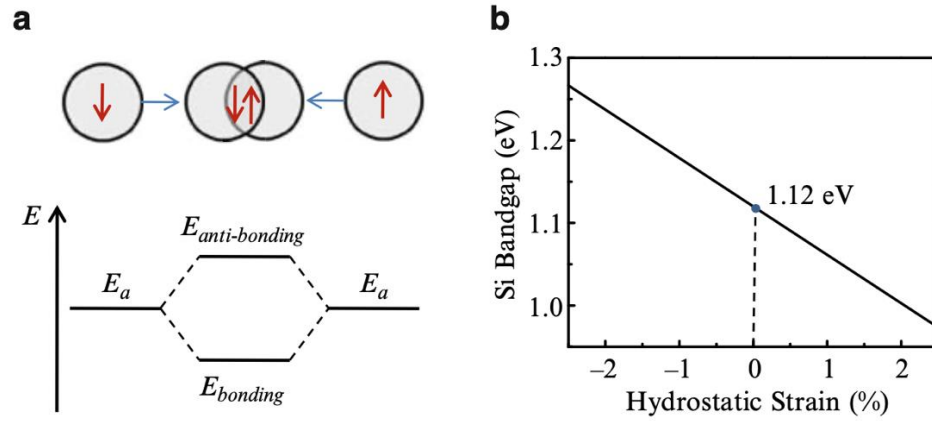


Figure 2.6 (a) Splitting mechanisms of the bonding and anti-bonding energy levels for a diatomic molecule; (b) Shifting of the Silicon bandgap under hydrostatic strain, negative strain means compressive stress applied and positive strain means tensile stress applied (Sun et al., 2010).

Unlike the hydrostatic strain, shear strain that destructs the symmetry of crystalline structure will lift the degeneracy of valence band maxima, and result in the splitting of original valence band into two or more same-level energy bands (Ding et al., 2015; Yixuan Wu et al.,

2020). The lifting of valence band degeneracy can enhance the density of states (DoS) by the degeneration factor. As a visual comparison, Figure 2.7 provides the diagrams of band splitting for Si, Ge and GaAs under a uniaxial compressive stress (Sun et al., 2010). It is observed in Figure 2.7 that the bandgap becomes larger under hydrostatic strain and the band degeneracy increases under shear strain. From a qualitative point of view, a wider bandgap due to hydrostatic strain will make it more difficult for electrons to hop from the conduction band to the valence band. However, the increased band degeneracy due to shear strain increases the number of measurable states on a same energy level, thus allowing more electrons to fill the valence band for charge carrier transfer. In other words, based on deformation potential analysis, it can be predicted that uniaxial compressive hydrostatic strain will weaken the conductivity (transconductance) of the semiconductor, but the uniaxial compressive shear strain will augment the conductivity of the semiconductor. The overall change in conductivity is determined by the collective effects of hydrostatic and shear strains, and it is also found that the conclusion based on the qualitative analysis is consistent with the results of several experimental studies (Han et al., 2010; Huang et al., 2019; Sun, 2007).

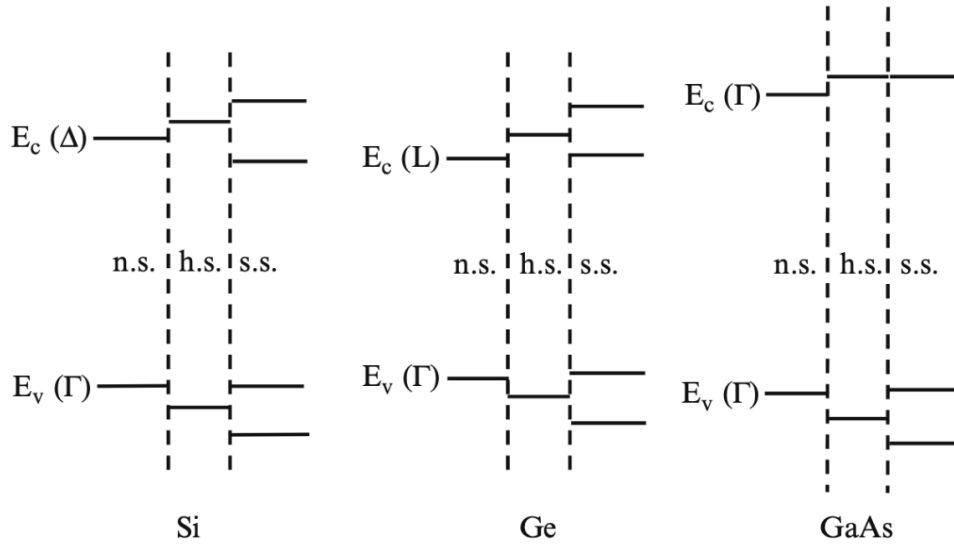


Figure 2.7 Band splitting diagrams for Si, Ge and GaAs when a uniaxial compressive stress is present with un-strained band denoted by “n.s.”, energy shifts due to hydrostatic strain denoted by “h.s.”, and energy splitting due to shear strain denoted by “s.s.” (Sun et al., 2010).

Since the strain effects on band structure are related to deformation potentials via Equation (2.11), the key to deformation potential theory is the calculation of deformation potentials  $\Xi$  under different strains and crystal structures (Dumke, 1956; Shuai et al., 2012). For a normal  $k$  point in the Brillouin zone, it is expected that three deformation potentials can portray the band energy shift. In points with high symmetry, counts of deformation potentials drop. For instance, some direct semiconductors, such as GaAs and CdTe, have only one deformation potential, namely the hydrostatic deformation potential  $\Xi_d^\Gamma$  to be needed at the symmetric band extrema point. Invoking the tight-binding model parameters, the deformation potentials can be evaluated by the overlap integrals (Mulliken, 1950; Ruedenbebg et al., 1966). For symmetric  $s$  orbitals, the overlap integral gives band edges as

$$E_{\pm s} = E_s \pm 4|V_{ss}| \quad (2.14)$$

where  $E_s$  is the on-site band edge for  $s$  orbitals, and  $V_{ss} = V_{ss\sigma}$  is the overlap integral between two neighboring  $s$  orbitals (Harrison, 2004). The “ $\pm$ ” means the bonding and anti-bonding states. Therefore, it can be easily deduced that the bandgap shift due to hydrostatic deformation potential is  $\Delta E = (\varepsilon_{xx} + \varepsilon_{yy} + \varepsilon_{zz}) \cdot (-8V_{ss})$ . In practice, however, deformation potentials should be experimentally measured, and the measured values can in turn determine the overlap integrals.

At the initial stage, for ISCs (e.g., Si, Ge, GaAs, ZnO, etc.) with single crystalline structures, the theoretical formulations based on deformation potential theory can accurately predict most of the strain-induced phenomenon in MOSFETs and TFTs (Fischetti & Laux, 1996; Gunda et al., 2017; Tserbak et al., 1993; Wacker et al., 2011; Z. Wang et al., 2012). Nevertheless, establishing the strain-induced electromechanical coupling relationships for OFETs is way more difficult than that for MOSFETs because the bonding and antibonding mechanisms for OSCs with irregular crystal structures can lead to more unrevealed modeling errors than ISCs (e.g., Si, Ge, GaAs, etc.) which have regular crystal structures. Over the last few decades, the development of electronic structure theory and relevant computational approaches, as well as high-performance computers, has made possible the use of quantum theory based first-principles, or *ab initio*, calculations for modeling of OFETs (Giustino, 2014; Kohanoff, 2006; Lejaeghere et al., 2016; Oba & Kumagai, 2018). Such first-principles calculations have provided useful insights in detailed understanding and delicate tailoring of defect states as well as bulk properties. For example, a first-principles calculation model was developed to study the

quantitative relationships between the molecular structures and the angular resolution anisotropic hole mobility (Wen et al., 2009). The mobilities of charge carriers coupled with molecular vibrations in an OSC were successfully evaluated by the first-principles calculation (Ishii et al., 2018). Density functional theory (DFT) based methods were applied in the prediction of optoelectronic and structural properties of inorganic-organic perovskites (a calcium titanium oxide mineral made of calcium titanate.) (Even et al., 2014). Unfortunately, most of these studies have targeted unstrained OSCs, while only a very few have explored the application of first-principles calculations to the prediction of post-strain/stress properties of deformable OSCs, such as the computational understanding of strain-controlled charge transport in 6,13-bis(triisopropylsilyl)ethynyl pentacene (TIPS Pentacene) (a p-type OSC) (Zheng et al., 2014), and the strain effects on the work function of polydimethylsiloxane (PDMS) (a silicone based organic polymer) (Wu et al., 2016). These limited studies are not sufficient to demonstrate the effectiveness of first-principles calculations for characterizing the electromechanical coupling relationships of OSCs, especially for the holistic modeling of OSC devices (e.g., OFETs) when complex physical characteristics of the interface are taken into account. In a broad sense, the physics based description and high-fidelity formulation of electromechanical coupling relationships for OSCs still remains a challenge.

## 2.2 Overview of Fractional Calculus Theory

Fractional calculus theory has its origins in a letter written by L'Hospital to Leibniz in 1695, when L'Hospital in the letter asked Leibniz what  $d^n y/dx^n$  is if  $n = 1/2$ . The theory grew from this informative dialogue with contributions from many mathematicians of later ages (Machado & Kiryakova, 2017). In recent years, fractional calculus is finding its applications in many fields of engineering and technology (Magin, 2006; Podlubny, 1999; Xue, 2017; Y. Yang & Zhang, 2019). It is an effective means for superior modeling and robust control of interdisciplinary systems (Del-Castillo-Negrete, 2006; Jiménez et al., 2017; Sakrajda & Wiraszka, 2018), distributive systems (Benson et al., 2013; Cartea & del-Castillo-Negrete, 2007; Francisco Gómez-Aguilar et al., 2015; Iyiola & Zaman, 2014), and complex systems (Benson et al., 2013; Magin, 2010; Maldon & Thamwattana, 2020), as well as for the characteristic identification of flexible electronics (Martynyuk & Ortigueira, 2015; Mitkowski & Skruch, 2013; Prasad et al., 2019; Quintana et al., 2006), transient analysis of ordinary engineering systems

(Macias & Sierociuk, 2013; Sierociuk et al., 2013; Sjöberg & Kari, 2002), and study of fluid flows in porous media (Choudhary et al., 2016; El-Amin, 2021). In light of the extensive adaptability of fractional calculus theory in the engineering modeling, this section aims to provide the basics of fractional calculus theory in preparation for the development of Fr-DD model.

### 2.2.1 Definitions of Fractional Operators

The Riemann-Liouville (RL) fractional derivative with order  $\gamma > 0$  is defined in Equation (2.15),

$${}^{RL}_a\mathcal{D}_t^\gamma(f(t)) = \frac{1}{\Gamma(n-\gamma)} \frac{d^n}{dt^n} \int_a^t \frac{f(\tau)}{(t-\tau)^{\gamma+1-n}} d\tau, \quad n-1 < \gamma < n \quad (2.15)$$

where  $\Gamma(n-\gamma)$  denotes the gamma function. Similarly, Caputo's fractional derivative with order  $\gamma > 0$  is defined in Equation (2.16).

$${}_a^C\mathcal{D}_t^\gamma(f(t)) = \frac{1}{\Gamma(n-\gamma)} \int_a^t \frac{f^{(n)}(\tau)}{(t-\tau)^{\gamma+1-n}} d\tau, \quad n-1 < \gamma < n \quad (2.16)$$

Both RL and Caputo's fractional derivatives can be considered as interpolation to integer-order derivatives, which means  ${}^{RL}_0\mathcal{D}_t^n(f(t)) = {}^C_0\mathcal{D}_t^n(f(t)) = f^{(n)}(t)$ . The Riemann-Liouville derivative can be related to Caputo's fractional derivative through the following lemma.

**Lemma 2.1** (Y. Yang & Zhang, 2019) *Assume  $f \in C^{n-1}([a, t])$  and  $n-1 < \gamma \leq n$ , then the following equality holds*

$${}_a^C\mathcal{D}_t^\gamma(f(t)) = {}^{RL}_a\mathcal{D}_t^\gamma(f(t)) - \sum_{k=0}^{n-1} \frac{f^{(k)}(a)}{\Gamma(k-\gamma+1)} (t-a)^{k-\gamma} \quad (2.17)$$

By directly utilizing the definitions of fractional derivatives, the composition rules for fractional derivatives are presented in the following lemma.

**Lemma 2.2** *Assume  $f \in C^{n+m-1}([a, t])$ ,  $n-1 < \gamma \leq n$ , and  $m > 0$  is an integer, then the following relations hold*

$$\frac{d^m}{dt^m} [{}^{RL}_a\mathcal{D}_t^\gamma(f(t))] = {}^{RL}_a\mathcal{D}_t^{\gamma+m}(f(t)) \quad (2.18)$$



$${}_a^C \mathcal{D}_t^\gamma \left( \frac{d^m}{dt^m} f(t) \right) = {}_a^C \mathcal{D}_t^{\gamma+m} (f(t)) \quad (2.19)$$

$${}^{RL}_a \mathcal{D}_t^\gamma \left( \frac{d^m}{dt^m} f(t) \right) = {}^{RL}_a \mathcal{D}_t^{\gamma+m} (f(t)) - \sum_{k=0}^{m-1} \frac{f^{(k)}(a)}{\Gamma(1+k-\gamma-m)} (t-a)^{k-\gamma-m} \quad (2.20)$$

$$\frac{d^m}{dt^m} [{}_a^C \mathcal{D}_t^\gamma (f(t))] = {}_a^C \mathcal{D}_t^{\gamma+m} (f(t)) + \sum_{k=n}^{n+m-1} \frac{f^{(k)}(a)}{\Gamma(1+k-\gamma-m)} (t-a)^{k-\gamma-m} \quad (2.21)$$

**Proof.** Equations (2.18) and (2.19) can be verified directly from the defining formulas of Riemann-Liouville and Caputo's fractional derivatives. The proofs of Equation (2.20) and Equation (2.21) are similar and only the proof of Equation (2.21) is provided here. From Lemma 2.1, it can be derived that

$$\begin{aligned} \frac{d^m}{dt^m} [{}_a^C \mathcal{D}_t^\gamma (f(t))] &= \frac{d^m}{dt^m} \left[ {}^{RL}_a \mathcal{D}_t^\gamma (f(t)) - \sum_{k=0}^{n-1} \frac{f^{(k)}(a)}{\Gamma(k-\gamma+1)} (t-a)^{k-\gamma} \right] \\ &= {}^{RL}_a \mathcal{D}_t^{\gamma+m} (f(t)) - \sum_{k=0}^{n-1} \frac{f^{(k)}(a) \cdot (k-\gamma) \cdots (1+k-\gamma-m)}{\Gamma(k-\gamma+1)} (t-a)^{k-\gamma-m} \\ &= {}_a^C \mathcal{D}_t^{\gamma+m} (f(t)) + \sum_{k=n}^{n+m-1} \frac{f^{(k)}(a)}{\Gamma(1+k-\gamma-m)} (t-a)^{k-\gamma-m} \end{aligned}$$

which completes the proof for Equation (2.21).

It can be observed that both Riemann-Liouville and Caputo's fractional derivatives can be composed with an integer-order derivative from both sides, but the commutative law does not hold for the combination of integer-order and fractional operators. Next, let us give the Laplace transformation of Riemann-Liouville and Caputo's fractional derivatives in the following lemma.

**Lemma 2.3** (Y. Yang & Zhang, 2019) *Assume  $f \in C^{n-1}([a, t])$  and  $n-1 < \gamma \leq n$ , then the Laplace transform of Riemann-Liouville and Caputo's fractional derivatives are given by*

$$\mathcal{L}\{ {}^{RL}_a \mathcal{D}_t^\gamma (f(t)) \} = s^\gamma F(s) - \sum_{k=0}^{n-1} s^k \cdot {}^{RL}_a \mathcal{D}_t^{\gamma-k-1} f(a) \quad (2.22)$$

$$\mathcal{L}\{ {}_a^C \mathcal{D}_t^\gamma (f(t)) \} = s^\gamma F(s) - \sum_{k=0}^{n-1} s^{\gamma-k-1} \cdot f^{(k)}(a) \quad (2.23)$$

One important formula which gives the Laplace transform of two-parameter Mittag-Leffler function  $\mathcal{E}_{\alpha,\beta}(at^\alpha)$  is given in Equation (2.24) (Haubold et al., 2011).

$$\mathcal{L}\{t^{\beta-1}\mathcal{E}_{\alpha,\beta}(\pm at^\alpha)\} = \frac{s^{\alpha-\beta}}{s^\alpha \mp a}, \quad \mathcal{R}(s) > 0, \mathcal{R}(\alpha) > 0, \mathcal{R}(\beta) > 0 \quad (2.24)$$

### 2.2.2 Caputo's Linear Fractional Differential Equation

In the case of  $0 < \gamma \leq 1$ , the following theorem gives an analytic solution to Caputo's linear fractional differential equation.

**Theorem 2.4** Consider the Caputo's linear fractional differential equation (Equation (2.25)) defined in a discretized one-dimensional domain where  $x \in [x_{i-1}, x_i]$  and  $0 < \gamma \leq 1$ , let  $u(x)$  be the state variable and  $v(x)$  be the input variable.

$${}_{x_{i-1}}^C \mathcal{D}_x^\gamma u(x) = Au(x) + Bv(x) \quad (2.25)$$

Then, the analytic solution to Equation (2.25) is given by

$$u(x) = \Phi(x - x_{i-1})u(x_{i-1}) + \int_0^{x-x_{i-1}} \Phi(x - x_{i-1} - y)B\hat{v}(y)dy \quad (2.26)$$

where  $\Phi(x) = \mathcal{E}_\gamma(Ax^\gamma)$  is the generalized state transition function,  $\mathcal{E}_\gamma(t)$  is the one-parameter Mittag-Leffler function, and the fictitious input function  $\hat{v}(y)$  is obtained by  $\hat{v}(x) = \mathcal{L}^{-1}\{V(s)s^{1-\gamma}\}$ .

**Proof.** Taking Laplace transform on both sides of Equation (2.25) generates

$$s^\gamma U(s) - s^{\gamma-1}u(x_{i-1}) = AU(s) + BV(s) \quad (2.27)$$

Rearrange both sides of Equation (2.27) and apply inverse Laplace transform, it begets

$$\begin{aligned} u(x) &= \mathcal{L}^{-1}\{(s^\gamma Id - A)^{-1}BV(s) + (s^\gamma Id - A)^{-1}s^{\gamma-1}u(x_{i-1})\} \\ &= \mathcal{L}^{-1}\{(s^\gamma Id - A)^{-1}s^{\gamma-1}\}u(x_{i-1}) + \mathcal{L}^{-1}\{(s^\gamma Id - A)^{-1}s^{\gamma-1}\} * B\mathcal{L}^{-1}\{s^{1-\gamma}V(s)\} \\ &= \mathcal{E}_\gamma(A(x - x_i)^\gamma)u(x_{i-1}) + \int_0^{x-x_i} \mathcal{E}_\gamma(A(x - x_{i-1} - y)^\gamma)B\hat{v}(y)dy \end{aligned}$$

where  $Id = 1$  or  $Id$  is the identity matrix in case  $u, v$  are vector variables. The last step complies with Equation (2.24), i.e., the inverse Laplace transform of the Mittag-Leffler function, when  $\alpha = \gamma$  and  $\beta = 1$ . Then, the proof is finished by applying the convolution theorem to the last equation.

Theorem 2.4 establishes a link between two consecutive states defined on two adjacent nodes  $\Omega_h = \{x_i = i\Delta x, i = 0, 1, 2, \dots, N\}$  where node-to-node step size is  $\Delta x = L/N$ . By setting  $x = x_i$ , Equation (2.26) becomes

$$u(x_i) = \Phi(\Delta x)u(x_{i-1}) + \int_0^{\Delta x} \Phi(\Delta x - y)B\hat{v}(y)dy \quad (2.28)$$

Assume that the input function is constant  $v(t) = 1$ , the fictitious input function is then evaluated by  $\hat{v}(y) = \mathcal{L}^{-1}\{s^{-\gamma}\} = \frac{y^{\gamma-1}}{\Gamma(\gamma)}$ . Since the commutative law is satisfied for convolution integrals, Equation (2.28) in this special case becomes

$$u(x_i) = \Phi(\Delta x)u(x_{i-1}) + B \int_0^{\Delta x} \Phi(y) \frac{(\Delta x - y)^{\gamma-1}}{\Gamma(\gamma)} dy \quad (2.29)$$

The second term on the right hand side of Equation (2.29) is the  $\gamma$ -fold fractional integral of  $\Phi(\Delta x)$ . In general, the  $\gamma$ -fold fractional integral of  $f(x)$  is defined in Equation (2.30) (Li et al., 2011).

$$\mathcal{I}_{0+}^{\gamma} f(x) = \frac{1}{\Gamma(\gamma)} \int_0^x \frac{f(y)}{(x-y)^{1-\gamma}} dy \quad (2.30)$$

In most cases, the  $\gamma$ -fold fractional integral cannot be evaluated analytically. However, the numerical approximations are always available. In the next section, numerical approximations of the  $\gamma$ -fold fractional integral and the  $\gamma$ -th order Caputo's fractional derivative are discussed.

### 2.2.3 Approximations of Fractional Integral and Fractional Derivatives

The following lemma gives a composite Simpson's rule for evaluating a  $\gamma$ -fold fractional integral to  $(3 + \gamma)$ -th order.

**Lemma 2.5** (Błaszczak et al., 2018) *Assume  $0 < \gamma \leq 1$  and  $f \in C^4([0, x])$ , then the following  $(3 + \gamma)$ -th order approximation of the  $\gamma$ -fold fractional integral can be obtained.*

$$\mathcal{I}_{0+}^{\gamma} f(x) = (\Delta x)^{\gamma} \left[ \sum_{k=0}^n b_{2k}^{(\gamma)} f(x_{2k}) + \sum_{k=1}^n b_{2k-1}^{(\gamma)} f(x_{2k-1}) \right] + \mathcal{O}(\Delta x^{3+\gamma}) \quad (2.31)$$

where  $x_j = j\Delta x$  with a positive integer  $j$  and step size  $\Delta x$ . Since  $x = x_{2n}$ , the coefficients  $b_j^{(\gamma)}$  can be determined by following relations:

$$b_{2k-1}^{(\gamma)} = -2 \frac{(2n-2k+2)^{2+\gamma} - (2n-2k)^{2+\gamma}}{\Gamma(3+\gamma)} + 2 \frac{(2n-2k+2)^{1+\gamma} + (2n-2k)^{1+\gamma}}{\Gamma(2+\gamma)}$$

$$b_{2k}^{(\gamma)} = \begin{cases} \frac{(2n)^{2+\gamma} - (2n-2)^{2+\gamma}}{\Gamma(3+\gamma)} - \frac{3(2n)^{1+\gamma} + (2n-2)^{1+\gamma}}{2\Gamma(2+\gamma)} + \frac{(2n)^\gamma}{\Gamma(1+\gamma)}, & k = 0 \\ \frac{(2n-2k+2)^{2+\gamma} - (2n-2k-2)^{2+\gamma}}{\Gamma(3+\gamma)} - \frac{(2n-2k+2)^{1+\gamma} + 6(2n-2k)^{1+\gamma} + (2n-2k-2)^{1+\gamma}}{2\Gamma(2+\gamma)}, & k = 1, \dots, n-1 \\ \frac{2^{2+\gamma}}{\Gamma(3+\gamma)} - \frac{2^{1+\gamma}}{2\Gamma(2+\gamma)}, & k = n \end{cases}$$

Since the fractional time-derivative is indispensable for transient dynamics simulation of Fr-DD model, the following lemma provides the first-order approximation for Caputo's fractional time-derivative of order  $0 < \gamma \leq 1$ .

**Lemma 2.6** Assume  $0 < \gamma \leq 1$  and  $f \in C^2([0, T])$ , then the following first-order approximation of the Caputo's time-fractional derivative can be obtained.

$${}_0^c \mathcal{D}_t^\gamma(f(t)) = \frac{1}{\Gamma(2-\gamma)} \sum_{m=0}^k \frac{f(t_{k+1-m}) - f(t_{k-m})}{\Delta t^\gamma} b_{m,k+1}^{(\gamma)} + \mathcal{O}(\Delta t) \quad (2.32)$$

where  $t_j = j\Delta t$  with a positive integer  $j$  and step size  $\Delta t$ . Let  $T = t_{k+1}$ , the coefficients  $b_{m,k+1}^{(\gamma)}$  are determined by  $b_{m,k+1}^{(\gamma)} = (m+1)^{1-\gamma} - m^{1-\gamma}$ .

**Proof.** The approximated expression in Equation (2.32) can be constructed by applying the piecewise quadrature, the estimate on truncation error is derived as follows,

$$\begin{aligned} & \left| {}_0^c \mathcal{D}_t^\gamma(f(t)) - \frac{1}{\Gamma(2-\gamma)} \sum_{m=0}^k \frac{f(t_{k+1-m}) - f(t_{k-m})}{\Delta t^\gamma} b_{m,k+1}^{(\gamma)} \right| \\ &= \left| {}_0^c \mathcal{D}_t^\gamma(f(t)) - \frac{1}{\Gamma(1-\gamma)} \sum_{m=0}^k \frac{f(t_{m+1}) - f(t_m)}{\Delta t} \int_{t_m}^{t_{m+1}} \frac{ds}{(t^{k+1} - s)^\gamma} \right| \\ &= \left| \frac{1}{\Gamma(1-\gamma)} \sum_{m=0}^k \int_{t_m}^{t_{m+1}} \left( f'(s) - \frac{f(t_{m+1}) - f(t_m)}{\Delta t} \right) \frac{ds}{(t^{k+1} - s)^\gamma} \right| \\ &\leq \frac{1}{\Gamma(1-\gamma)} \sum_{m=0}^k \int_{t_m}^{t_{m+1}} |f'(s) - f'(\xi_1)| \frac{ds}{(t^{k+1} - s)^\gamma} \\ &\leq \frac{1}{\Gamma(1-\gamma)} \sum_{m=0}^k \int_{t_m}^{t_{m+1}} \frac{ds}{(t^{k+1} - s)^\gamma} |f^{(2)}(\xi_2)| \Delta t \\ &\leq \frac{1}{\Gamma(1-\gamma)} \sum_{m=0}^k \int_{t_m}^{t_{m+1}} \frac{M ds}{(t^{k+1} - s)^\gamma} \Delta t = \frac{C \Delta t}{\Gamma(1-\gamma)} \end{aligned}$$

where  $M = \max_{t \in [0, T]} f^{(2)}(t)$  and  $C$  is a constant. Mean value theorem is applied on a compact domain  $[0, T]$  for  $f(t)$  and  $f'(t)$ .

### 2.3 Summary

This chapter provided an extensive survey of recent advances in the field of organic field-effect transistors and fractional calculus. The OFETs generally have two different naming conventions. The fabrication and layout of OFETs are dependent on the type of material, dimensions and operating environment of the semiconductors. The development of mechanical, electrical and electromechanical coupling models for organic FETs requires a good understanding of the physical properties of organic semiconductors, in particular the transport properties of carriers within semiconductors. The current most effective methods for describing the electromechanical coupling of inorganic semiconductors were to resort to strained semiconductor theory and deformation potential theory. However, no clear method exists for establishing electromechanical coupling relationships for organic semiconductors. Although first-principles simulations can solve for the electronic structure of specific organic molecules, such *ab initio* computational methods cannot provide a uniform physical description of organic devices in general, and the cost of such calculations is often prohibitive. In view of this, the exploration and development of OFET models based on solid-state physics and organic semiconductor theory is urgently needed. In addition, the fractional calculus theory, which has been gaining ground in various fields of engineering applications in recent years, has also been extended to the modelling of OFETs. However, OFET models based on fractional calculus theory are underdeveloped, so follow-up work is urgently needed to refine these models.

## **CHAPTER 3. RESEARCH METHODOLOGY**

This chapter presented the methodology and research framework for the modeling of OFETs under mechanical deformation. The modeling framework developed in this chapter was divided into four sections. The first section developed a Mass-Spring-Damper (MSD) model for simulation of internal stress/strain distribution in a thin film transistor. In the second section, the generalized solid-state model was proposed to model the pre- and post-bent dynamics of OFETs. The third section discussed the fractional drift-diffusion (Fr-DD) model that is capable of describing the transient and steady-state dynamics of generic organic semiconductor devices. A summary to this chapter was given in the last section. Sections 3.1, 3.2, and 3.3 of chapter three were revised based on the author's published papers (Y. Yang et al., 2020, 2021a, 2021b).

### **3.1 Study of Strained TFT Based on Mass-Spring-Damper Model**

Networked in according to a two-dimensional topology, a group of masses, springs and dampers can demonstrate its ability to simulate the internal strain/stress distribution in a Zinc Oxide (ZnO, an n-type ISC) thin-film transistor (TFT). In this section, the Mass-Spring-Damper (MSD) model of thin film electronics was proposed to study the mechanical properties of TFTs. Combined with an electromechanical coupling relationship that is derived from the deformation potential theory, the MSD model is capable of characterizing strain effects on TFT's electrical parameters. The fidelity of the MSD model for the mechanical characterization of an inverted staggered TFT can be evaluated by comparing its simulation results with that of a finite element analysis (FEA) model. When the strain induced shifts of carrier mobility and the threshold voltage are considered in the characteristic equations of the n-type MOSFET (dynamics of the inorganic TFT can be approximated by MOSFET characteristic equations), the post-stress dynamics of the ZnO TFT can be obtained.

#### **3.1.1 Derivation of Finite Element Model**

To derive the solid mechanics model, all the internal layers of the TFT are considered as linearly elastic and inviscid materials (Bauchau & Craig, 2009; Nan, 2013). In addition, the following assumptions all hold true.

- (a) All the solid materials are isotropic and homogeneous, the stress and strain follow Hooke's law, and the fourth-order stiffness tensor (elastic moduli)  $s$  is symmetric.
- (b) The thin-film electrical parameters are not affected by environment factors (e.g., room temperature, humidity, etc.).
- (c) The body force is omitted (i.e.,  $b = 0$ ), and heat source (i.e.,  $\varphi = 0$ ) is not considered in the simulation study.

In Eulerian description, twenty-three unknown variables, i.e., the mass density  $\rho$ , displacement  $u_i$ ,  $i = 1,2,3$ ., stress  $\sigma_{ij}$ ,  $i, j = 1,2,3$ ., strain  $\varepsilon_{ij}$ ,  $i, j = 1,2,3$ ., and temperature  $T$  are needed to represent mechanical states at a spatial point. By applying the balance law for mass, linear momentum, angular momentum and energy, Equations (3.1)-(3.6) can be formed to model the mechanical states of a solid body.

$$\dot{\rho} + \rho \dot{u}_{i,i} = 0 \quad (3.1)$$

$$\rho \ddot{u}_i - \sigma_{ji,j} = 0 \quad (3.2)$$

$$\sigma_{ij} = \sigma_{ji} \quad (3.3)$$

$$\rho c_v \dot{T} + \sigma_{ij} \dot{u}_{i,j} + k T_{k,k} = 0 \quad (3.4)$$

$$\varepsilon_{ij} = \frac{1}{2} (u_{i,j} + u_{j,i}) \quad (3.5)$$

$$\sigma_{ij} = s_{ijkl} \varepsilon_{kl} - \beta_{ij} (T - T_0) \quad (3.6)$$

where the indices in the equations obey Einstein's summation convention,  $c_v$  is the constant volume specific heat,  $k$  is the the heat conductivity,  $s_{ijkl}$  is the fourth-order stiffness tensor, and  $\beta_{ij}$  is the thermal-stress coupling coefficients in Duhamel-Neumann relation (Duhamel, 1837). Consider the symmetry of  $\sigma$ ,  $\varepsilon$  and  $s$ , by setting  $\beta_{ij} = 0$ , which is valid for homogeneous and isotropic materials, Equation (3.6) can be represented in a matrix form as Equation (3.7),

$$\begin{bmatrix} \varepsilon_{11} \\ \varepsilon_{22} \\ \varepsilon_{33} \\ 2\varepsilon_{23} \\ 2\varepsilon_{13} \\ 2\varepsilon_{12} \end{bmatrix} = \frac{1}{E} \begin{bmatrix} 1 & -\nu & -\nu & 0 & 0 & 0 \\ -\nu & 1 & -\nu & 0 & 0 & 0 \\ -\nu & -\nu & 1 & 0 & 0 & 0 \\ 0 & 0 & 0 & 2(1+\nu) & 0 & 0 \\ 0 & 0 & 0 & 0 & 2(1+\nu) & 0 \\ 0 & 0 & 0 & 0 & 0 & 2(1+\nu) \end{bmatrix} \begin{bmatrix} \sigma_{11} \\ \sigma_{22} \\ \sigma_{33} \\ \sigma_{23} \\ \sigma_{13} \\ \sigma_{12} \end{bmatrix} \quad (3.7)$$

where  $E$  is the Young's modulus and  $\nu$  is the Poisson's ratio. Equations (3.1)-(3.7) form the governing equations and couples twenty-three unknown variables for a continuum solid body. In case of simple body geometry with reduced boundary conditions, the equation system of

Equations (3.1)-(3.7) can be solved analytically (Evans, 2010; S. M. Yang & Tao, 2006). However, for solid bodies with complex geometry and boundary conditions, numerical solvers based on the finite element method (FEM) are always available. In this study, all the finite element simulations are performed with COMSOL.

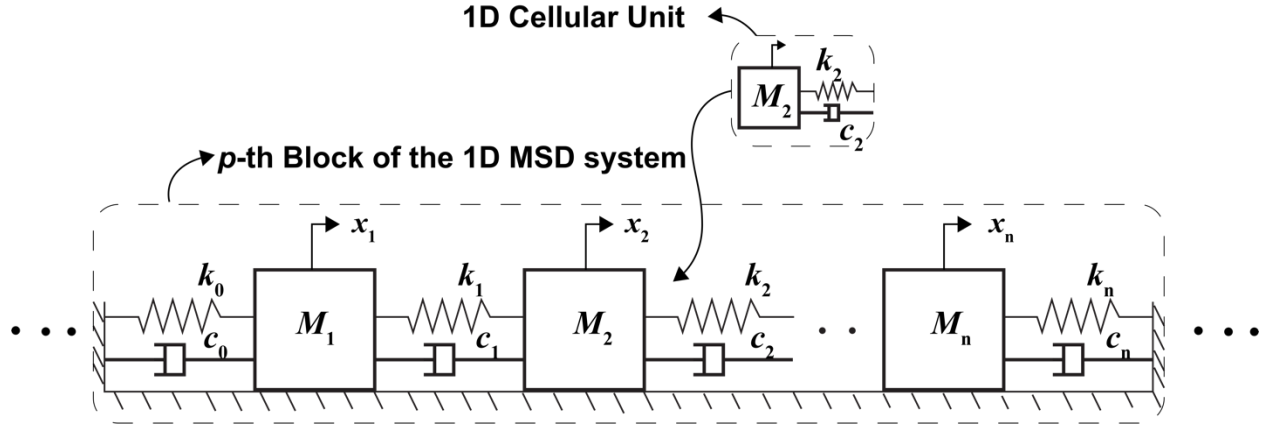


Figure 3.1 The schematic representation of the one-dimensional MSD model, the cellular unit is composed of a mass center, an ideal spring and an ideal damper (Y. Yang et al., 2020).

### 3.1.2 Derivation of 1D Mass-Spring-Damper Model

As shown in Figure 3.1, the one-dimensional MSD model is composed of a series of cellular units. Consider an infinite number of blocks of cellular units connected in the serial structure, the boundary conditions of the 1D MSD model vanish. In the case of infinite MSD structure with geometrical periodicity (all the blocks are the same), Bloch theorem implies that the system states should also be geometrically periodic. The dynamics of a 1D MSD system with infinite geometric periodicity is given by Equation (3.8),

$$m_j \ddot{u}_{p+j} - c_j (\dot{u}_{p+j+1} - \dot{u}_{p+j}) + c_{j-1} (\dot{u}_{p+j} - \dot{u}_{p+j-1}) - k_j (u_{p+j+1} - u_{p+j}) + k_{j-1} (u_{p+j} - u_{p+j-1}) = 0 \quad (3.8)$$

where  $u_{p+j}$  is the displacement of the  $j$ -th cellular unit in the  $p$ -th block,  $m_j$ ,  $c_j$  and  $k_j$  are the mass, damping ratio and spring stiffness of the  $j$ -th cellular unit in the  $p$ -th block, respectively. Here,  $p$ -th block is the  $p$ -th cluster of cellular units with repetitive pattern in an infinite series of cellular units. Jensen (2003) proved that Equation (3.8) has an analytic solution  $u_{p+j}(t) = A_j e^{(p+j)\gamma - i\omega t}$ , where  $A_j$  is the displacement amplitude of the  $j$ -th cellular unit in the  $p$ -th block,  $\gamma$  is the wave number and  $\omega$  is the wave frequency.



In a more general situation where the number of cellular units is finite and geometric periodicity loses, boundary effects need to be considered in the modeling. In this case, the one-dimensional MSD model is represented by Equations (3.9)-(3.11),

$$m_j \ddot{u}_j - c_j(\dot{u}_{j+1} - \dot{u}_j) - k_j(u_{j+1} - u_j) = f_j, \quad j = 1 \quad (3.9)$$

$$\begin{aligned} m_j \ddot{u}_j - c_j(\dot{u}_{j+1} - \dot{u}_j) + c_{j-1}(\dot{u}_j - \dot{u}_{j-1}) - k_j(u_{j+1} - u_j) + k_{j-1}(u_j - u_{j-1}) \\ = f_j, \quad \forall j = 2, \dots, N-1 \end{aligned} \quad (3.10)$$

$$m_j \ddot{u}_j + c_{j-1}(\dot{u}_j - \dot{u}_{j-1}) + k_{j-1}(u_j - u_{j-1}) = f_j, \quad j = N \quad (3.11)$$

where  $f_j$  is the external force acted on the  $j$ -th cellular unit,  $N$  is the number of cellular units in the 1D case. Consider a series of external forces with same and constant frequency, i.e.,  $f_j = \tilde{f}_j e^{i\omega t}$ , it can be easily verified that the solution to Equations (3.9)-(3.11) has a general form as  $u_j = \tilde{u}_j e^{i\omega t}$ . Substituting the external forces and the general-form solution into Equations (3.9)-(3.11) can produce Equation (3.12), which is the characteristic equation of the 1D MSD model,

$$(-\omega^2 M + i\omega C + K)\tilde{u} = \tilde{f} \quad (3.12)$$

where  $M$ ,  $C$  and  $K$  are the mass, damping, and spring matrix of the 1D MSD system. The parameter matrices are represented in Equations

$$K = \begin{bmatrix} k_1 & -k_1 & & & \\ -k_1 & k_1 + k_2 & -k_2 & & \\ & -k_2 & k_2 + k_3 & -k_3 & \\ & & \dots & \dots & \dots \\ & & & -k_{N-1} & k_{N-1} \end{bmatrix} \quad (3.13)$$

$$C = \begin{bmatrix} c_1 & -c_1 & & & \\ -c_1 & c_1 + c_2 & -c_2 & & \\ & -c_2 & c_2 + c_3 & -c_3 & \\ & & \dots & \dots & \dots \\ & & & -c_{N-1} & c_{N-1} \end{bmatrix} \quad (3.14)$$

$$M = \begin{bmatrix} m_1 & & & & \\ & m_2 & & & \\ & & m_3 & & \\ & & & \dots & \\ & & & & m_N \end{bmatrix} \quad (3.15)$$

The mass, spring stiffness and damping coefficients of each cellular unit can be determined from material's constitutive equation. For instance,  $m_j$  can be related to the size of the cellular unit and the density of the solid material,  $k_j$  is proportional to Young's modulus of

the material, and  $c_j$  is approximated by the material's viscosity. If cellular units are treated as perfect second-order harmonic oscillators, the damping coefficients  $c_j$  can be evaluated via Equation (3.16),

$$c_j = 2\zeta_j \sqrt{m_j \tilde{k}_j} \quad (3.16)$$

where  $\tilde{k}_j = m_j \omega_j^2$  is the equivalent stiffness with  $\omega_j = \sqrt{\frac{k_j + k_{j-1}}{m_j}}$  in 1D case, and  $\zeta_j$  is the damping ratio (viscosity) of the material (Hesam et al., 2019).

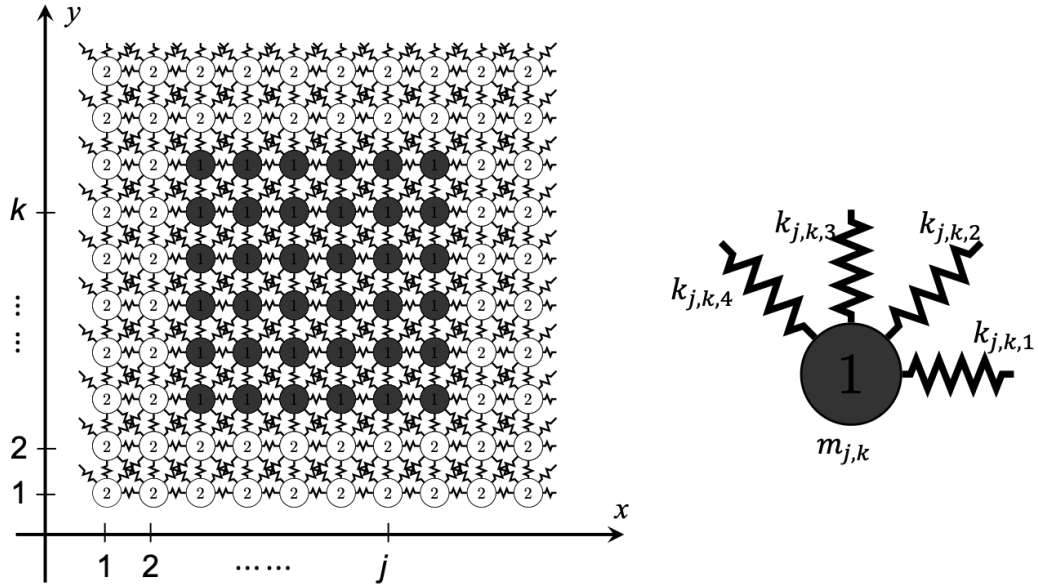


Figure 3.2 The schematic representation of a 2D MSD model (left) with its inclusion made of type-1 material and its external two layers filled by type-2 material, the cellular unit (right) is composed of a mass center, four bidirectional springs and four bidirectional dampers (Y. Yang et al., 2020).

### 3.1.3 Derivation of 2D Mass-Spring-Damper Model

The schematic representation of a two-dimensional MSD model is shown in Figure 3.2. The cellular unit of a 2D MSD model consists of a mass center, four bidirectional springs and four bidirectional dampers aligned along  $0^\circ$ ,  $45^\circ$ ,  $90^\circ$  and  $135^\circ$ , respectively. For a 2D MSD model with infinite geometric periodicity, Bloch theorem gives its solution as

$$u_{p+j,q+k} = A_{j,k} \exp \left( i \left( (p+j)\gamma_x + (q+k)\gamma_y - \omega t \right) \right) \quad (3.17)$$

$$v_{p+j,q+k} = B_{j,k} \exp\left(i\left((p+j)\gamma_x + (q+k)\gamma_y - \omega t\right)\right) \quad (3.18)$$

where  $A_{j,k}$  and  $B_{j,k}$  are the displacement magnitude,  $\omega$  is the displacement wave frequency,  $\gamma_x$  and  $\gamma_y$  are the two components of a wavenumber vector  $\gamma$ .

If the 2D MSD model has finite cellular units and loses its geometric periodicity, its dynamics is described by Equations (3.19) and (3.20),

$$\begin{aligned} m_{j,k} \ddot{u}_{j,k} - c_{j,k,1}(\dot{u}_{j+1,k} - \dot{u}_{j,k}) - k_{j,k,1}(u_{j+1,k} - u_{j,k}) \\ - 0.5c_{j,k,2}(\dot{u}_{j+1,k+1} - \dot{u}_{j,k} + \dot{v}_{j+1,k+1} - \dot{v}_{j,k}) \\ - 0.5k_{j,k,2}(u_{j+1,k+1} - u_{j,k} + v_{j+1,k+1} - v_{j,k}) \\ - 0.5c_{j,k,4}(\dot{u}_{j-1,k+1} - \dot{u}_{j,k} - \dot{v}_{j-1,k+1} + \dot{v}_{j,k}) \\ - 0.5k_{j,k,4}(u_{j-1,k+1} - u_{j,k} - v_{j-1,k+1} + v_{j,k}) \\ - c_{j-1,k,1}(\dot{u}_{j-1,k} - \dot{u}_{j,k}) - k_{j-1,k,1}(u_{j-1,k} - u_{j,k}) \\ - 0.5c_{j-1,k-1,2}(\dot{u}_{j-1,k-1} - \dot{u}_{j,k} + \dot{v}_{j-1,k-1} - \dot{v}_{j,k}) \\ - 0.5k_{j-1,k-1,2}(u_{j-1,k-1} - u_{j,k} + v_{j-1,k-1} - v_{j,k}) \\ - 0.5c_{j+1,k-1,4}(\dot{u}_{j+1,k-1} - \dot{u}_{j,k} - \dot{v}_{j+1,k-1} + \dot{v}_{j,k}) \\ - 0.5k_{j+1,k-1,4}(u_{j+1,k-1} - u_{j,k} - v_{j+1,k-1} + v_{j,k}) = f_{j,k,x} \end{aligned} \quad (3.19)$$

$$\begin{aligned} m_{j,k} \ddot{v}_{j,k} - c_{j,k,3}(\dot{v}_{j,k+1} - \dot{v}_{j,k}) - k_{j,k,3}(v_{j,k+1} - v_{j,k}) \\ - 0.5c_{j,k,2}(\dot{v}_{j+1,k+1} - \dot{v}_{j,k} + \dot{u}_{j+1,k+1} - \dot{u}_{j,k}) \\ - 0.5k_{j,k,2}(v_{j+1,k+1} - v_{j,k} + u_{j+1,k+1} - u_{j,k}) \\ - 0.5c_{j,k,4}(\dot{v}_{j-1,k+1} - \dot{v}_{j,k} - \dot{u}_{j-1,k+1} + \dot{u}_{j,k}) \\ - 0.5k_{j,k,4}(v_{j-1,k+1} - v_{j,k} - u_{j-1,k+1} + u_{j,k}) \\ - c_{j,k-1,3}(\dot{v}_{j,k-1} - \dot{v}_{j,k}) - k_{j,k-1,3}(v_{j,k-1} - v_{j,k}) \\ - 0.5c_{j-1,k-1,2}(\dot{v}_{j-1,k-1} - \dot{v}_{j,k} + \dot{u}_{j-1,k-1} - \dot{u}_{j,k}) \\ - 0.5k_{j-1,k-1,2}(v_{j-1,k-1} - v_{j,k} + u_{j-1,k-1} - u_{j,k}) \\ - 0.5c_{j+1,k-1,4}(\dot{v}_{j+1,k-1} - \dot{v}_{j,k} - \dot{u}_{j+1,k-1} + \dot{u}_{j,k}) \\ - 0.5k_{j+1,k-1,4}(v_{j+1,k-1} - v_{j,k} - u_{j+1,k-1} + u_{j,k}) = f_{j,k,y} \end{aligned} \quad (3.20)$$

where  $u_{j,k}$  and  $v_{j,k}$  are two components of the displacement vector in 2D,  $f_{j,k,x}$  and  $f_{j,k,y}$  are two components of the external force acted on mass center  $m_{j,k}$  in 2D. To solve Equations (3.19) and

(3.20), a set of boundary conditions has to be imposed on the boundary cellular units. By reference to the classification of boundary conditions in the PDE theory, boundary conditions of the 2D MSD model can be grouped into three classes: Dirichlet (D-type) condition, Neumann (N-type) condition and Robin (R-type) condition (Evans, 2010; Moin, 2010; Polyanin & Nazaikinskii, 2016). The three different boundary conditions are specified in Equations (3.21)-(3.23),

$$u_{j,k} = a_{j,k}(t), v_{j,k} = b_{j,k}(t) \quad (3.21)$$

$$\dot{u}_{j,k} = \alpha_{j,k}(t), \dot{v}_{j,k} = \beta_{j,k}(t) \quad (3.22)$$

$$u_{j,k} + c\dot{u}_{j,k} = \phi_{j,k}(t), v_{j,k} + d\dot{v}_{j,k} = \psi_{j,k}(t) \quad (3.23)$$

where  $a_{i,j}$ ,  $b_{i,j}$ ,  $\alpha_{i,j}$ ,  $\beta_{i,j}$ ,  $\phi_{i,j}$  and  $\psi_{i,j}$  are boundary excitations (functions of time),  $c$  and  $d$  are constant parameters, the index numbers for the boundary layer are  $j \in \{1, M\}$  and  $k \in \{1, N\}$ .

In 2D MSD model, let  $k_{j,k,2} = k_{j,k,4} = \frac{1}{2}k_{j,k,1} = \frac{1}{2}k_{j,k,3}$ , the damping coefficients can be determined via Equation (3.24),

$$c_{j,k,l} = \begin{cases} 2\zeta_{j,k}\sqrt{m_{j,k}\tilde{k}_{x,j,k}} & \text{for } l = 1 \\ 2\zeta_{j,k}\sqrt{m_{j,k}\tilde{k}_{y,j,k}} & \text{for } l = 3 \end{cases} \quad (3.24)$$

where  $\tilde{k}_{x,j,k} = m_{j,k}\omega_{x,j,k}^2$  and  $\tilde{k}_{y,j,k} = m_{j,k}\omega_{y,j,k}^2$  are the effective spring stiffness in the  $x$  and  $y$  directions, respectively. If  $l = 2$  or  $l = 4$ , the damping coefficients are given by  $c_{j,k,2} = c_{j,k,4} = \frac{c_{j,k,1} + c_{j,k,3}}{4}$ . In addition, the two components of wave frequency vector  $\omega_{x,j,k}^2$  and  $\omega_{y,j,k}^2$  are defined by Equations (3.25) and (3.26), respectively.

$$\omega_{x,j,k}^2 = \frac{k_{j,k,1} + k_{j-1,k,1} + 0.5(k_{j,k,2} + k_{j,k,4} + k_{j-1,k-1,2} + k_{j+1,k-1,4})}{m_{j,k}} \quad (3.25)$$

$$\omega_{y,j,k}^2 = \frac{k_{j,k,3} + k_{j,k-1,3} + 0.5(k_{j,k,2} + k_{j,k,4} + k_{j-1,k-1,2} + k_{j+1,k-1,4})}{m_{j,k}} \quad (3.26)$$

### 3.1.4 Strain-Induced Electrical characteristics of the ZnO TFT

Before proceeding to investigate how the electrical transconductance and outputs of an TFT change in response to the channel strain/stress, several notations from crystallography need to be reviewed. The triplet  $\langle h, k, l \rangle$ , a.k.a., the Miller index, denotes a lattice plane in a

Bravais lattice. The normal vector to plane  $\langle h, k, l \rangle$  is  $\vec{n} = h\vec{b}_1 + k\vec{b}_2 + l\vec{b}_3$ , where  $\vec{b}_i, i = 1, 2, 3$  are the unit basis vectors of the reciprocal lattice (Rogalski & Palmer, 2014). As shown in Figure 3.3, it is a convention in semiconductor industry to fabricate the TFT on the standard  $\langle 001 \rangle$  plane (wafer plane). In this configuration, the direction angles of the channel currents  $J$  and the average stress  $\sigma$  in the plane are given by angle  $\theta$  and  $\varphi$ , respectively. The stress  $\sigma$  is considered as the average stress combined by the longitudinal and lateral stress components. The longitudinal stress component is parallel to the semiconductor channel, and the lateral component is the in-plane stress perpendicular to the semiconductor channel. The transversal stress component (out-of-plane stress component) is neglected in this setting.

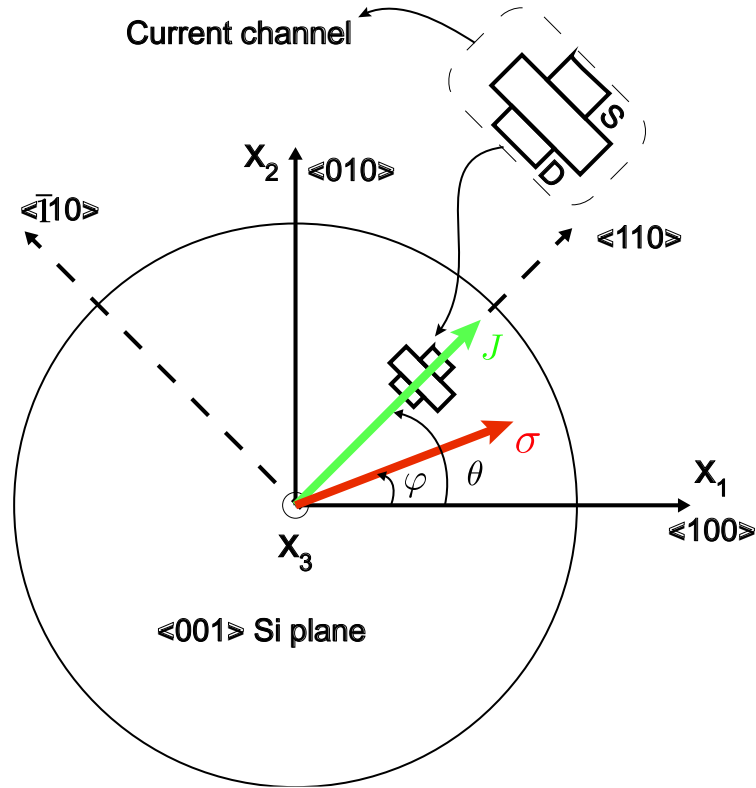


Figure 3.3 A widely used fabrication layout of a  $\langle 001 \rangle$  wafer plane, with channel current flow  $J$  and the average stress  $\sigma$  (Y. Yang et al., 2020).

#### 3.1.4.1 Strain Effects on Carrier Transport Mobility

Strain effects on carrier transport mobility can be qualitatively understood by Drude's model (Drude, 1900). Based on Drude's model, the carrier mobility at equilibrium state is given

by Equation (3.27),

$$\mu = \frac{e\tau}{m} \quad (3.27)$$

where  $e$  is the electron charge,  $m$  is the effective electron mass or effective hole mass, and  $\tau$  is the mean free time between ionic collisions. From Drude's model, it easily implies that mobility can be affected by strain via two ways, i.e., through changing the effective mass  $m$  or altering mean free time between ionic collisions  $\tau$ . The carrier effective mass can be changed by band edges shifting and the valence band splitting because the effective mass is dependent on the shape of  $E - k$  diagram. The mean free time between ionic collisions alteration is a little complicated, and its value is essentially determined by various scattering mechanisms, such as the carrier-to-carrier scattering, carrier-to-nuclei scattering, ionized impact scattering, etc. For lightly and moderately doped ISCs (Si, Ge, GaAs, ZnO), the influence of scattering events on mobility is negligible compared to the effects of bands shifting and splitting (S. S. Li, 2007). However, the scattering effects on the mobility of OSCs cannot be ignored.

To quantitatively study the strain effects on carrier transport mobility, it is necessary to understand the relationship between the carrier mobility  $\mu$  and the semiconductor conductivity  $\kappa$ . The drift current density resulting from an external electric field can be given in Equation (3.28),

$$J = J_e + J_p = (en\mu_e + ep\mu_h)F \quad (3.28)$$

where  $n, p$  are respectively the electron concentration and the hole concentration in the bulk semiconductor,  $\mu_e, \mu_h$  are respectively the electron mobility and the hole mobility, and  $F$  is the external electric field intensity. Ohm's law is then applied to obtain the drift current density in terms of the conductivity,

$$J = \kappa F \quad (3.29)$$

where  $\kappa$  is the conductivity of the bulk semiconductor. Therefore, it is available to relate  $\kappa$  to  $\mu$  through Equation (3.30).

$$\kappa = en\mu_e + ep\mu_h \quad (3.30)$$

In all the factors that affect the carrier mobility, the change of resistivity  $\rho = \frac{1}{\kappa}$  dominates in semiconductors. From Equation (3.30), it can be inferred that resistivity  $\rho$  is inversely proportional to the carrier mobility  $\mu$ , and thus strain-modified band structure, and subsequently altered mobility is a direct result of the piezoresistive effect. Here, the strain-induced shift on carrier mobility can be related to piezoresistive effect via Equation (3.31),

$$\frac{\Delta\mu_{eff}}{\mu_{eff}} \cong \frac{\Delta\rho}{\rho} = \Pi(\theta, \varphi) \cdot \sigma \quad (3.31)$$

where  $\Pi(\theta, \varphi)$  is the piezoresistive coefficient depending on the direction angles of the average stress and the current flow on  $\langle 001 \rangle$  plane. For the manufacturing layout shown in Figure 3.3,  $\Pi(\theta, \varphi)$  can be determined by Equation (3.32) (Wacker *et al.*, 2011),

$$\begin{aligned} \Pi(\theta, \varphi) = & \Pi_{11} \cdot (\cos^2 \theta \cdot \cos^2 \varphi + \sin^2 \theta \cdot \sin^2 \varphi) + \Pi_{12} \\ & \cdot (\cos^2 \theta \cdot \sin^2 \varphi + \sin^2 \theta \cdot \cos^2 \varphi) + 2 \cdot \Pi_{44} \cdot \sin \theta \cdot \cos \theta \\ & \cdot \sin \varphi \cdot \cos \varphi \end{aligned} \quad (3.32)$$

where  $\Pi_{11}$ ,  $\Pi_{12}$  and  $\Pi_{44}$  are three fundamental piezoresistive coefficients of the semiconductor. As mentioned before, ignoring the stress component in the transversal direction (i.e., in  $(0,0,1)$  direction.) may slightly deteriorate the accuracy of the strained mobility model. Without loss of the generality, we can assume  $\varphi = \theta$  so that the carrier flow direction can be the same as the stress direction in the  $\langle 001 \rangle$  plane. If the TFT is fabricated by following the style in Figure 3.3, with which  $\theta = 45^\circ$  can be imposed. In this scenario, the piezoresistive coefficient for doped Silicon was reported to be  $\Pi(45^\circ, 45^\circ) = (480 \pm 4) \times 10^{-12} \text{ Pa}^{-1}$  (Wacker *et al.*, 2011). In the case of the ZnO TFT, the gauge factor of ZnO was reported to be  $2.6 \pm 0.2$  (Cardoso *et al.*, 2014). Given that the elastic modulus of ZnO is 156 GPa, the piezoresistive coefficient for ZnO can be evaluated as  $(16.67 \pm 1.28) \times 10^{-12} \text{ Pa}^{-1}$ .

### 3.1.4.2 Strain Effects on Threshold Voltage

Strain-induced shift on threshold voltage is significant to account for performance benchmarking of strained TFTs. Although TFTs and MOSFETs operate on different principles, the electrical transconductance and output characteristics of TFTs can still be described by the electrical equations of MOSFETs over a range of bias (Perumal *et al.*, 2013). In traditional semiconductor theory, the threshold voltage of an n-type MOSFET is defined in Equation (3.33),

$$V_{th} = V_{fb} + 2(2m - 1)\psi_s \quad (3.33)$$

where  $V_{fb}$  is the flat-band voltage,  $m$  ( $\sim 1.2 - 1.4$ ) is the body-effect coefficient, and  $\psi_s$  is the potential difference between the extrinsic and intrinsic Fermi levels. The body-effect coefficient is slightly dependent on channel strain. However, strain can greatly take effects on the net shifts of the valence band and the conduction band, and thus induces the shift of the extrinsic Fermi

levels and the bandgap. Based on deformation potential theory, the threshold voltage shift of a strained n-type MOSFET is given by Equation (3.34) (Lim et al., 2004; Yongke Sun et al., 2010),

$$\Delta V_{th} = \frac{1}{e} \left\{ \Delta E_c + (m - 1) \left[ \Delta E_g + kT \cdot \log \frac{N_v(0)}{N_v(\sigma)} \right] \right\} \quad (3.34)$$

where  $\Delta E_c$  is the strain-induced shift on conduction band edges,  $\Delta E_g$  is the bandgap shift, and  $N_v$  is the valence band effective density of states (DOS),  $e$  is the electron charge. Because the contribution made by changes in valence band effective DOS is relatively small compared to the band structure changes in strained ZnO, the last term in Equation (3.34) can be neglected (Hur et al., 2006). Therefore, it remains to determine  $\Delta E_c$  and  $\Delta E_g$  in Equation (3.34).

ZnO has a direct and wide bandgap, and its band structure is symmetric in the near neighboring of band extrema (Janotti & Van De Walle, 2009; Zwicker & Jacobi, 1985). Because of the symmetry, Pikus & Bir (1974) proved that two effective masses and two deformation potentials are needed to describe the strain-induced shift on conduction band. In accordance with Herring and Vogt's notation, the edge shift of conduction band valley  $i$  can be expressed as Equation (3.35) (Van De Walle, 1989),

$$\Delta E_c^{(i)} = (\Xi_d \bar{1} + \Xi_u \{\hat{a}_i \hat{a}_i\}) : \bar{\epsilon} \quad (3.35)$$

where  $\bar{1}$  is the unit tensor,  $\hat{a}_i$  is the unit wavevector (a.k.a.,  $k$  vector) of valley  $i$ ,  $\{\}$  is the dyadic product,  $\Xi_d$  and  $\Xi_u$  are the dilation and uniaxial deformation potentials at the conduction band edges, and  $\bar{\epsilon}$  is the strain tensor. Then, it can be proved that the average shift of the conduction band edges is

$$\Delta E_{c,av} = \left( \Xi_d + \frac{1}{3} \Xi_u \right) \bar{1} : \bar{\epsilon} = \left( \Xi_d + \frac{1}{3} \Xi_u \right) \cdot \text{trace}(\bar{\epsilon}) \quad (3.36)$$

where  $\text{trace}(\bar{\epsilon})$  is the trace of the strain tensor, which is equal to the crystal volume change, the quantity  $\left( \Xi_d + \frac{1}{3} \Xi_u \right)$  represents the hydrostatic deformation potential for the conduction band.

The number before  $\Xi_u$  is 1/3 because the conduction band of most semiconductors, such as Si, GaAs and ZnO have three valleys (L-valley,  $\Gamma$ -valley and X-valley) in total. Table 3.1 summarizes several deformation potential values for Si, Ge, ZnO. These values have been calculated and experimentally verified in multiple literatures. The superscripts in Table 3.1 denote (1)(Yongke Sun et al., 2010), (2)(Tserbak et al., 1993), (3)(Fischetti & Laux, 1996), (4)(Janotti & Van De Walle, 2007), and (5)(Rowe et al., 1968). Values with asterisk mean  $\Xi_d +$



$\frac{1}{3}\Xi_u - a$ , where  $a$  is Pikus-Bir deformation potential. Values with double asterisks mean  $\Xi_d + \frac{1}{3}\Xi_u$ . All quantities in Table 3.1 are in eV. In addition to  $\Delta E_c$ , the magnitude of the threshold voltage shift depends on the bandgap shift  $\Delta E_g$  as well. Band structure analysis reveals that  $\Delta E_g$  is proportional to the strain in the semiconductor channel. Ojha *et al.* (2016) stated that  $\Delta E_g$  with strain is as few as meV in the advanced CMOS technology (Si), thus in normal cases the second term in Equation (3.34) can be ignored. However, Janotti & Van De Walle (2007) reported that the bandgap-narrowing deformation potential of ZnO is  $\Xi_g = -1.7$  eV, so in calculating  $\Delta V_{th}$  for ZnO,  $\Delta E_g$  should be evaluated.

Table 3.1. Dilation and uniaxial (shear) deformation potentials for Si, Ge and ZnO. For the same deformation potential, values extracted from different literatures may vary from each other due to different doping conditions and calculation errors.

	$\Xi_d$ (eV)			$\Xi_u$ (eV)		
Si	-6.0 <sup>(1)</sup>	-0.77 <sup>*(2)</sup>	2.5 <sup>*(3)</sup>	7.8 <sup>(1)</sup>	8.86 <sup>(2)</sup>	10.5 <sup>(3)</sup>
Ge	-9.1 <sup>(1)</sup>	-0.9 <sup>*(2)</sup>	5.75 <sup>*(3)</sup>	15.9 <sup>(1)</sup>	7.24 <sup>(2)</sup>	9.75 <sup>(3)</sup>
ZnO	-2.3 <sup>** (4)</sup>	-1.34 <sup>(5)</sup>		-2.3 <sup>** (4)</sup>	-2.66 <sup>(5)</sup>	

By substituting Equation (3.36) into Equation (3.34), the strain-induced shift of the threshold voltage can be determined. However, it needs to mention that the actual value of the deformation potential in Equation (3.36) depends not only on the type of semiconductor material, the form in which the semiconductor is present, the doping condition, but also on the environment (e.g., temperature, light intensity, humidity) around the semiconductor. In most cases, the deformation potentials  $\Xi_d$  and  $\Xi_u$  should be experimentally measured.

#### 3.1.4.3 Post-Stress Dynamics of ZnO TFT

For an enhancement-mode n-type MOSFET, its transconductance and output characteristics can be described by Equations (3.37) and (3.38) (Sedra & Smith, 2015; Shichman & Hodges, 1968), in which Equations (3.37) represents the dynamics of MOSFETs in the linear regime and Equation (3.38) represents the dynamics of MOSFETs in the saturation regime,

$$I_D = \mu_{eff} C_{ox} \frac{W}{L} \left[ (V_{GS} - V_{th}) V_{DS} - \frac{V_{DS}^2}{2} \right] \quad (3.37)$$

$$I_D = \frac{\mu_{eff} C_{ox} W}{2 L} (V_{GS} - V_{th})^2 [1 + \lambda (V_{DS} - V_{DSsat})] \quad (3.38)$$

where  $\mu_{eff}$  is the effective carrier mobility,  $C_{ox}$  is the per unit area gate oxide capacitance,  $W$  is the channel width (lateral size),  $L$  is channel length (longitudinal size),  $\lambda$  is the channel-length modulation parameter ( $\sim 0.01$ ),  $V_{GS}$  is the potential difference between gate and source electrodes, and  $V_{DS}$  is the applied bias between the drain and source electrodes.

Heidari *et al.* (2016) studied strain-induced changes on  $C_{ox}$  in the Verilog-A model, in which he found that the strained effects on  $C_{ox}$  is infinitesimal. Because the strain effects on the remaining electrical parameters (e.g.,  $C_{ox}$ ,  $W$ ,  $L$ ,  $\lambda$ ) are not so significant, only the strain-induced mobility and threshold voltage are considered in Equations (3.37) and (3.38) to model the post-stress dynamics of ZnO TFT.

### 3.2 Study of Bendable OFETs Based on Generalized Solid State Model

This section presented a generalized solid-state model that incorporates the density of trap states for a bendable OFET. This study aims at proposing a new modeling framework to characterize the bending induced electrical properties of an OFET quantitatively in the linear and saturation regimes. In this model, the charge carrier transport in the conduction channel was described by Poisson's equation which considers in the OSC's bandgap. The low-field enhancement and high-field degradation of the field-effect mobility under gradual channel approximation was taken into account in the overall mobility model. Accordingly, the generalized current-voltage equations that can reflect the transconductance and outputs of OFETs were derived for the first time. Moreover, a semiempirical electromechanical coupling relationship was proposed per the analogy between ISCs' and OSCs' band structures to quantify the influence of mechanical strain on the field-effect mobility, and the threshold voltage.

#### 3.2.1 **Geometry and Band Structure of OFETs**

The OFETs are generally made from three sorts of materials: the OSCs, the conductive electrodes, and the dielectric insulators. As shown in Figure 2.2, Four distinct configurations exist for OFETs (Singh et al., 2009). Because enhanced performance such as the high carrier

mobility and the  $I_{on}/I_{off}$  ratio can be demonstrated by the bottom-gate, top-contact (BGTC) OFET when it is compared to the other OFET configurations, this study is focused on the modeling of a BGTC OFET (Vidor et al., 2016). Nevertheless, the applicability of the modeling framework proposed in this study to the other four configurations of OFETs should also be mentioned here as well.

In the BGTC OFET, a soft layer of a specific OSC, such as dinaphtho[2,3b:2',3'-f]thieno[3,2-b]thiophene (DNTT), is deposited on top of a layer of dielectric insulator. Two neighboring conductive electrodes (source and drain) are placed on top of the OSC layer. The dielectric insulator layer which is made of Parylene is positioned below the OSC layer and isolating the OSC from the bottom gate electrode. The OSC is typically a type of conductive polymers with irregular crystalline (polycrystalline or amorphous) structures and influenced by the grain effects on the single crystal boundaries. Compared to the conventional inorganic semiconductors (ISCs, e.g., Si, Ge, GaAs, ZnO etc.), OSCs (organic matters forming a chain or net-like macromolecular structures) are mainly made up of carbon atoms and possess a considerable amount of localized trap density levels in the band structure due to strong  $\pi$  and  $\sigma$  bonds among carbon atoms. As shown in Figure 3.4, the highest energy levels occupied by unexcited holes and electrons in ISCs are respectively called valence band ( $E_v$ ) and conduction band ( $E_c$ ), and the two important energy levels that takes a similar role in OSCs are respectively named as HOMO (Highest Occupied Molecular Orbit) and LUMO (Lowest Unoccupied Molecular Orbit), in which the bandgap of OSCs is given by  $E_g = E_{LUMO} - E_{HOMO}$ .

Simplified band structures of ISCs and OSCs are given in Figure 3.4. As displayed in Figure 3.4(b), a substantial trap states (defects that can trap or detrap mobile carriers) exist in the bandgap of OSCs, while no trap state exists for ISCs. Depending on the polarity of the defects, the trap states can be classified into two groups: the donor-like trap states which are mainly distributed close to the LUMO edges, and the acceptor-like trap states that are distributed around HOMO edges. Due to their specific locations in the bandgap, the donor-like trap states can seize holes excited from the LUMO edges, and the acceptor-like trap state can capture electrons excited from the HOMO edges. The considerable amount of trap states in the OSCs reduces the density and concentration of majority carriers (i.e., holes in p-type OSC and electrons in n-type OSC) in the accumulation layer, therefore the current conduction capability of OFETs are generally weaker than Inorganic TFTs. In the OFETs' modeling, both the density of states (i.e.,

electrons and holes) and trap states (i.e., donor-like and acceptor-like trap states) need to be considered.

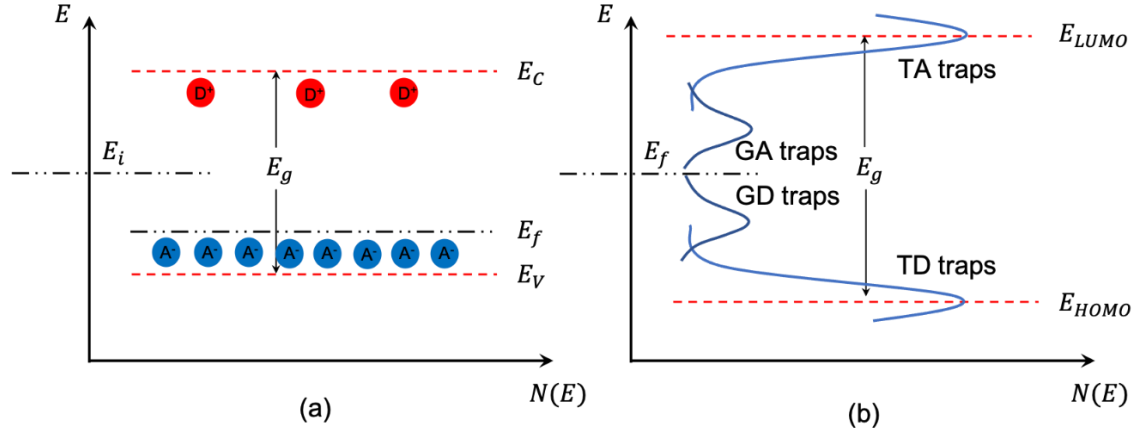


Figure 3.4 (a) Simplified band structure of a p-type ISC with ionized donors (red) and ionized acceptors (blue); (b) of a p-type OSC with deep and shallow trap states with the density of states at energy level  $E$  denoted by  $N(E)$  (Y. Yang et al., 2021a).

### 3.2.2 Carrier Density and Surface Potential Modeling

The electron and hole concentrations ( $n$  and  $p$ ) for an OSC in equilibrium conditions are dependent on temperatures and can be described by Equations (3.39) and (3.40),

$$n(T) = N_l(T) \exp\left(-\frac{E_{LUMO} - E_f}{kT}\right) \quad (3.39)$$

$$p(T) = N_h(T) \exp\left(-\frac{E_f - E_{HOMO}}{kT}\right) \quad (3.40)$$

where  $N_l$  and  $N_h$  are respectively the effective density of states (DoS) in the LUMO and HOMO edges, the values of  $N_l$  and  $N_h$  depend on the effective mass of carriers and temperature.  $T$  is the temperature in Kelvin,  $k$  is the Boltzmann constant and  $E_f$  is the Fermi level. In addition, it is usually assumed in the charge carrier concentration derivations that the semiconductor is nondegenerate so that the probability for an available state at an energy level  $E$  to be occupied by a mobile carrier can be determined by Boltzmann statistics. This assumption for the nondegeneracy of the energy band is valid for the OSCs since OSCs are typically undoped semiconductors, which have the Fermi level more than  $3kT$  away from both the HOMO and LUMO edges. As a result, an important formula that gives the carrier concentration  $n_i$  of an

intrinsic semiconductor can be obtained by evaluating the product of electron and hole concentrations for extrinsic semiconductors.

$$n_i^2 = n(T)p(T) = N_l(T)N_h(T) \exp\left(-\frac{E_g}{kT}\right) \quad (3.41)$$

As shown in Figure 3.4, both the donor- or acceptor-like trap states in deep levels are assumed to be distributed in Gaussian and the shallow trap states are assumed to be exponentially distributed. The density of tail-level acceptor-like (TA), tail-level donor-like (TD), deep-level acceptor-like (GA) and deep-level donor-like (GD) trap states are presented in Equations (3.42)-(3.45), respectively,

$$g_{TA}(E) = N_{TA} \exp\left(\frac{E - E_{LUMO}}{w_{TA}}\right) \quad (3.42)$$

$$g_{TD}(E) = N_{TD} \exp\left(\frac{E_{HOMO} - E}{w_{TD}}\right) \quad (3.43)$$

$$g_{GA}(E) = N_{GA} \exp\left(-\left(\frac{E_{GA} - E}{w_{GA}}\right)^2\right) \quad (3.44)$$

$$g_{GD}(E) = N_{GD} \exp\left(-\left(\frac{E_{GD} - E}{w_{GD}}\right)^2\right) \quad (3.45)$$

where  $N_{TA}$ ,  $N_{TD}$ ,  $N_{GA}$  and  $N_{GD}$  are band edge intercept densities.  $w_{TA}$ ,  $w_{TD}$ ,  $w_{GA}$ ,  $w_{GD}$ ,  $E_{GA}$  and  $E_{GD}$  are tunable model parameters. For a p-type OSC, more important role can be played by the donor-like trap states in the shallow (tail) level (i.e., TD traps) than the other types of trap states because TD traps are closer to the HOMO edges and the continuous trapping and detrapping activities participated by TD traps have a greater influence on the majority carrier concentrations in the accumulation layer. Based on Boltzmann statistical mechanics, the ionization probability for trap states can be derived. Since only the TD trap states are considered in this study, the ionization probability  $f_{TD}(E)$  of the TD trap states is given in Equation (3.46).

$$f_{TD}(E) = \frac{1}{1 + \exp\left(\frac{E - E_f}{kT}\right)} \quad (3.46)$$

To calculate the concentration of ionized trap states, the integral  $\int_{-\infty}^{+\infty} g_{TD}(E)(1 - f_{TD}(E))dE$  has to be evaluated. By setting  $w_{TD} = kT_1$ , where  $T_1$  is the characteristic temperature of the TD trap states, it can be shown that the integral is not convergent if  $T_1 < T$ . Thus, the integral only needs to be evaluated for  $T_1 \geq T$ , then the concentration of ionized TD trap states

can be obtained in Equation (3.47),

$$g_{TD}^+ = N_{TD0}(T) \exp\left(\frac{E_{HOMO} - E_f}{kT_1}\right) \quad (3.47)$$

and the edge intercept of the ionized TD trap state concentration  $N_{TD0}(T)$  is evaluated by Equation (3.48),

$$N_{TD0}(T) = \alpha(T)N_{TD} \frac{k^2 T_1^2}{kT_1 - kT} \quad (3.48)$$

where the dimensionless parameter  $\alpha(T) = 0.8 \sim 1$  solely depends on the temperature and can compensate the integration error.

Figure 3.5 shows the anatomy of an TCBG OFET, if the gate electrode is connected to a voltage source, a thin and conductive channel (typically with only a few angstroms thickness for OSCs) may form near the semiconductor-dielectric interface by majority carrier concentrations, and this thin channel aggregated by majority carriers is the accumulation layer (the red part in Figure 3.5) of the OFET.

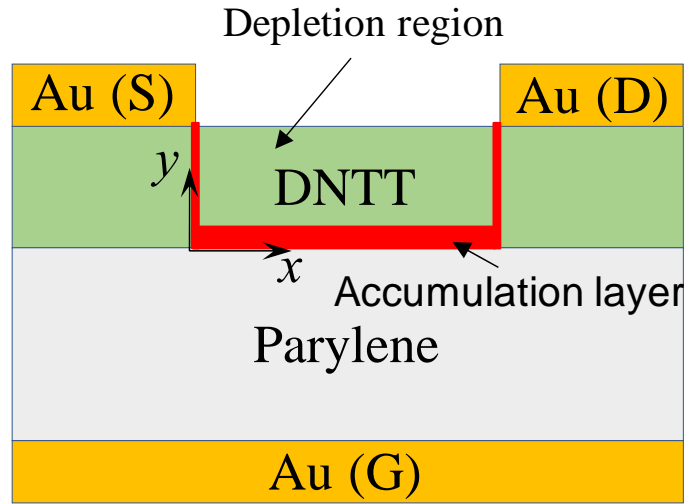


Figure 3.5 The anatomy of a TCBG OFET with coordinate system positioning along the semiconductor-dielectric interface, the red portion is the accumulation layer for charge carrier transport between drain and source electrodes (Y. Yang et al., 2021a).

Poisson's equation in electrostatics can be applied to approximate the electric potentials near the semiconductor-dielectric interface, as given in Equation (3.49),

$$\nabla^2 \varphi = -\frac{q}{\varepsilon_s} (p - n + N_D^+ - N_A^-) \quad (3.49)$$

where  $\varphi$  is the electrostatic potential of the OSC,  $N_D^+$  and  $N_A^-$  are respectively the concentrations of ionized donor-like and acceptor-like sites, including trap states and dopants. Since the OSCs can be treated as intrinsic semiconductors and only TD trap states are considered in the energy band structure of the OSC, it implies that  $n \approx 0$ ,  $N_A^- \approx 0$ , and  $N_D^+ \approx g_{TD}^+$ . Substituting Equations (3.40) and (3.47) into Equation (3.49) produces the electric field  $E(x, y)$  in the OSC as a function of the electrostatic potential  $\varphi$ ,

$$E(x, y) = \sqrt{\frac{2kTN_h}{\varepsilon_s}} \cdot F(\varphi) \quad (3.50)$$

where the electrostatic potential  $\varphi(x, y)$  can be evaluated via an implicit potential function  $F(\varphi)$ , which is presented in Equation (3.51).

$$F(\varphi) = \left[ \left( e^{-\frac{q\varphi}{kT}} + \frac{q\varphi}{kT} - 1 \right) + \frac{n_i^2}{N_h^2} \left( e^{\frac{q\varphi}{kT}} - \frac{q\varphi}{kT} - 1 \right) + \frac{N_{TD0}T_1}{N_hT} \left( e^{-\frac{q\varphi}{kT_1}} - 1 \right) \right]^{1/2} \quad (3.51)$$

By setting  $y = 0$ , the potential at the semiconductor-dielectric interface can be obtained  $\varphi_s = \varphi(x, 0)$ . Therefore, the gate voltage  $V_{gs}$  can also be analytically calculated via Equation (3.52) by assuming that the charge flux is continuous at the semiconductor-dielectric interface,

$$V_{gs} = \varphi_s + \frac{K_S}{K_O} x_o E_s + V_{fb} \quad (3.52)$$

where  $K_S$ ,  $K_O$  are the OSC's and insulator's relative permittivity coefficient, respectively.  $x_o$  is the thickness of insulator,  $E_s$  is the electric field intensity at the semiconductor-dielectric interface, and  $V_{fb}$  is the flat-band voltage that is determined by the difference of the electrode's workfunction and the semiconductor's workfunction.

### 3.2.3 Field-Effect Mobility Model

Both the band-like carrier transport model or the hopping energy model can be utilized to describe the effective field-effect mobility in the OSC layer of an OFET (Horowitz, 1998; Silvaco International, 2016). The hopping mechanism of charge carriers was developed for

disordered semiconductors by Ela & Afifi (1979), and it is revealed in recent research that the hopping mechanism leads to a similar field-effect mobility as the band-like carrier transport model (Giannini et al., 2018; Wang et al., 2012). This study adopts the band-like transport model to calculate the effective field-effect mobility in the OSCs. Many scattering mechanisms can affect the field-effect mobility in a semiconductor. For example, the lattice scattering mechanism can account for the reduced carrier mobilities caused by collisions among charge carriers and thermally excited OSC atoms, and the ionized impurity scattering event is a result of direct collisions or Coulombic interactions among charge carriers and acceptor/donor-like defects. In general, distinct mobility models are usually expected to be concatenated in Matthiessen rule to reflect the influence of different scattering mechanisms on the charge carrier transport. In particular, the ionized impurity scattering mechanism plays a central role in regulating the overall field-effect mobility of OFETs due to the existence of a substantial number of ionized acceptor/donor-like defects in the OSC's active channel. A well-known OSC's field-effect mobility model is the Poole-Frenkel (PF) model (Gill, 1972), which takes into account a field-dependent enhancement in the carrier mobility as presented in Equation (3.53),

$$\mu_{PF} = \mu_0 \exp\left(-\frac{\Delta}{kT}\right) \exp\left[\left(\frac{\beta}{kT} - \gamma_{pf}\right) \sqrt{E_x}\right] \quad (3.53)$$

where  $\mu_0$  is the field-free nonactivated field-effect mobility of OSCs,  $\Delta$  is the field-free activation energy,  $\beta$  and  $\gamma_{pf}$  are two fitting parameters, and  $E_x$  is the electric field parallel to the direction of the conductive channel. The Coulombic interactions among defects and charge carriers are explained by Coulombic scattering model (Shin et al., 1989), which is displayed in Equation (3.54),

$$\mu_{C,p} = \frac{N2P \cdot \left(\frac{T}{300}\right)^{1.5}}{N_{TD} \ln(1 + \gamma_{BHp}) - \frac{\gamma_{BHp}}{1 + \gamma_{BHp}}} \quad (3.54)$$

and Equation (3.55),

$$\gamma_{BHp} = \frac{N1P}{N_h} \cdot \left(\frac{T}{300}\right)^{ALPHA_p} \quad (3.55)$$

where  $N1P$ ,  $N2P$  and  $ALPHA_p$  are three fitting parameters for Coulombic scattering model,  $T$  is the temperature (Kelvin) in the conductive channel,  $N_{TD}$  is the edge intercept of the TD trap states concentration, and  $N_h$  is the effective DoS in HOMO edges. In addition to the



aforementioned two mobility models, it also requires a field-dependent mobility model to guarantee that the carrier's drift velocity will get saturated under high field region, a good mobility model for this purpose is the Caughey-Thomas (CT) model (Caughey & Thomas, 1967), which is given in Equation (3.56),

$$\mu_{CT} = \frac{\mu_0}{\left(1 + \left(\frac{\mu_0 E_{||}}{v_{sat}}\right)^{BETACT}\right)^{\frac{1}{BETACT}}} \quad (3.56)$$

where  $v_{sat}$  is the saturated carrier's drift velocity parallel to the direction of conductive channel,  $E_{||}$  is the component of the electric field that is parallel to the channel and  $BETACT$  is a fitting parameter in CT model. According to Matthiessen rule, the overall field-effect mobility  $\mu_{eff}$  of an OFET can be computed by Equation (3.57).

$$\frac{1}{\mu_{eff}} = \frac{1}{\mu_{PF}} + \frac{1}{\mu_{C,p}} + \frac{1}{\mu_{CT}} \quad (3.57)$$

### 3.2.4 Generalized Current-Voltage Equations

Figure 3.5 presents the structure of an BGTC OFET with channel length  $L$  and channel width  $W$ , the thickness of the accumulation layer is denoted by  $y_a(x)$ . Since in practical scenarios,  $y_a(x) \ll L$ , the changes of carrier concentration in the  $y$  direction can be ignored, thus the charge flux per  $\text{cm}^2$  can be evaluated as  $Q_p(x) = q \int_0^{y_a(x)} (p + g_{TD}^+) dy \approx q y_a \cdot (p + g_{TD}^+)$ . The mobile holes and ionized TD trap states contribute to the positive charges in  $Q_p$ , and the relationship between  $Q_p$  and the applied gate bias is given by Equation (3.58),

$$Q_p(x) = C_{ox}(V_{gs} - V_{th} - V(x)) \quad (3.58)$$

where  $C_{ox}$  is dielectric capacitance per unit area of gate,  $V_{gs}$  is the voltage bias between gate and source electrodes,  $V_{th}$  is the threshold voltage and  $V(x)$  is the electrostatic potential with respect to source electrode in the  $x$  direction. Substituting expressions for  $p$  and  $g_{TD}^+$  from Equations (3.40) and (3.47) into Equation (3.58), the charge-voltage equation can be produced as

$$p + p^{T/T_1} \left( \frac{N_{TD0}}{N_h^{T/T_1}} \right) = \frac{C_{ox}}{q y_a} (V_{gs} - V_{th} - V(x)) \quad (3.59)$$

Because the concentration of ionized trap states is far greater than the concentration of mobile holes in a p-type OFET, the first term on the left side of Equation (3.59) can be ignored.

Upon simplifications, the concentration of mobile holes in the conductive channel can be evaluated by Equation (3.60).

$$p = N_h \left[ \frac{C_{ox} (V_{gs} - V_{th} - V(x))}{q\gamma_a N_{TD0}} \right]^{T_1/T} \quad (3.60)$$

For an OFET with medium or long channel length, the diffusion motions of mobile carriers can be neglected. In this case, only the drift motions of carriers will take part in the formation of current flows in the channel. Consider that the change of the electric field along  $x$  direction is trivial compared to the change along the  $y$  direction (i.e., gradual channel approximation), the total current that flows through the channel can be evaluated from Equation (3.61).

$$I(x) = -\mu_{eff} W q \cdot \left( \int_0^{y_a(x)} p(x, y) dy \right) \cdot \frac{dV(x)}{dx} \quad (3.61)$$

By substituting Equation (3.60) into Equation (3.61) and integrating both sides of Equation (3.61) over  $[0, L]$ , the channel current can be obtained as Equation (3.62),

$$I_D = \frac{(q\gamma_a)^{1-\gamma} \mu_{eff} W N_h C_{ox}^\gamma}{(\gamma + 1) L N_{TD0}^\gamma} \left[ (V_{ds} + V_{th} - V_{gs})^{\gamma+1} - (V_{th} - V_{gs})^{\gamma+1} \right] \quad (3.62)$$

where  $\gamma = T_1/T$  is the fitting parameter to reflect the relative size of TD trap states in the OSC's bandgap over the effective DoS in the HOMO band edges, and  $V_{ds}$  is the voltage between drain and source electrodes. Moreover, if Taylor expansion is applied to Equation (3.62) at  $V_{ds} = 0$  and the first order terms are preserved in the expansion, it can be found that Equation (3.62) will be reduced to a self-explanatory form as shown in Equation (3.63).

$$I_D = -\frac{(q\gamma_a)^{1-\gamma} \mu_{eff} W N_h C_{ox}^\gamma}{L N_{TD0}^\gamma} \left[ (V_{gs} - V_{th}) V_{ds} - \frac{\gamma}{2} V_{ds}^2 \right] \quad (3.63)$$

Letting  $\gamma = 1$ , it can be easily proved that  $N_h$  and  $N_{TD0}$  are almost the same in magnitude. Thus, the generalized current-voltage equations in Equations (3.62) and (3.63) for OFETs degenerates to the current-voltage model for MOSFETs or inorganic TFTs, as reflected by Equation (3.64).

$$I_D = -\frac{\mu_{eff} W C_{ox}}{L} \left[ (V_{gs} - V_{th}) V_{ds} - \frac{1}{2} V_{ds}^2 \right] \quad (3.64)$$

When the magnitude of  $V_{ds}$  exceeds  $(V_{gs} - V_{th})$ , the pinch-off of the accumulation layer will force the drain current to get saturated. Then, the generalized current-voltage equation in the saturation regime becomes Equation (3.65).

$$I_{DSat} = -\frac{(q\gamma_a)^{1-\gamma}\mu_{eff}WN_hC_{ox}^\gamma}{(\gamma+1)LN_{TD0}^\gamma}(V_{th}-V_{gs})^{\gamma+1} \quad (3.65)$$

As the generalized current-voltage equations are derived for the OFETs, the thickness of the accumulation layer  $y_a(x)$  may not be considered as a constant value in practical situations. However,  $y_a$  in the model can be treated as the nominal thickness of the accumulation layer, so that  $y_a$  can be extracted from the Atlas simulation. It should be mentioned that the generalized current-voltage equations proposed in this study *cannot* explain the OFET characteristics in the subthreshold regime. For characterizing the transconductance of OFETs in the subthreshold regime, Equation (3.66), a variant form of (Meer et al., 2004), is considered,

$$I_D = I_{D0} \cdot \left(\frac{V_{gs}}{V_T}\right)^\alpha \exp\left(\frac{V_{th}-V_{gs}}{nV_T}\right) \quad (3.66)$$

where  $I_{D0}$  is the leakage current,  $V_T = kT/q$  is the thermal voltage,  $n$  is the slope parameter, and  $\alpha$  is a fitting parameter.

### 3.2.5 Electromechanical Coupling Model

The lattice mismatches during film growth in epitaxial heterostructures, phonon-agitated lattice vibrations, intrinsic strain in thin film depositions, and external loads can result in the mechanical strain inside bulk semiconductors (Sun et al., 2010). Because the bonding and antibonding mechanisms for OSCs (DNTT, TIPS Pentacene etc.) bring more unparallel modeling errors than ISCs (e.g., Si, Ge, GaAs, ZnO etc.), deriving the strain-related electromechanical coupling relationships for OFETs is way more difficult than MOSFETs and inorganic TFTs. Upon that, the method of superpositions is adopted and the semiempirical model is proposed to account for the influence of bending on the characteristics of OFETs. Consider the OFET structure shown in Figure 3.5, the mechanical strain developed at the semiconductor-dielectric interface can be given by Equation (3.67) (Fukuda et al., 2013; Oh et al., 2018),

$$\varepsilon = \left(\frac{d_s + d_f}{2R}\right) \frac{(1 + 2\chi\eta + \chi\eta^2)}{(1 + \eta)(1 + \chi\eta)} \quad (3.67)$$

where  $d_s$  and  $d_f$  are the thickness of the substrate and the active layer, respectively.  $\chi = Y_f/Y_s$ , which is the elastic moduli ratio of the OSC to the substrate.  $\eta = d_f/d_s$  and  $R$  is the radius of the bending curvature. In the experimental setup (Nawrocki et al., 2016), the insulator and the substrate are both made from Parylene, the thickness of the gold gate can be ignored so the total thickness of the insulator and the substrate is  $d_s$  in Equation (3.67). In addition, Drude's mobility model (Equation (3.27)) implies that the mechanical strain can affect OSC's field-effect mobility by interfering the scattering mechanisms, so multiple types of scattering effects are considered in the carrier mobility model (Equation (3.57)). According to analysis in section 3.1.4.1, the carrier mobility is also related to the semiconductor resistivity. In this study, a semiempirical expression in Equation (3.68) can be established to correlate the surface mechanical strain  $\varepsilon$  to the shift of the field-effect mobility  $\Delta\mu_{eff}$ ,

$$\frac{\Delta\mu_{eff}}{\mu_{eff}} \cong \frac{\Delta\rho}{\rho} = \Pi(\theta, \varphi) \cdot C\varepsilon \quad (3.68)$$

where  $\Pi(\theta, \varphi)$  is the piezoresistive coefficient,  $\theta$  and  $\varphi$  are direction angles depending on the crystal structure and OFET configurations.  $C$  is the normalized stiffness constant and  $\varepsilon$  is the average strain on the semiconductor-dielectric interface surface. Utilizing Equation (3.68) to predict the strain effects on the field-effect mobility of ISCs was experimentally validated in many literatures (Bradley et al., 2001; Heidari et al., 2017; Thompson et al., 2004; Wacker et al., 2011). However, it seems that this study is the first one to apply Equation (3.68) to predict the bending induced effects on the field-effect mobility of OSCs, and based on this study, it is found that Equation (3.68) can demonstrate a good agreement with the pre-bent and post-bent experimental data in the linear and saturation regimes.

Strain alters the threshold voltage by a different means. The OSCs' band structure will be changed by the mechanical strain in terms of the band splitting in LUMO and HOMO band edges, bandgap narrowing and band warping. By referring to Equation (3.34), it can be shown that the strain induced shift of the threshold voltage for a p-type OFET is given by Equation (3.69),

$$\Delta V_{th} = \frac{1}{q} \left\{ \Delta E_{HOMO} + (m - 1) \left[ \Delta E_g + kT \cdot \log \frac{N_l(0)}{N_l(\varepsilon)} \right] \right\} \quad (3.69)$$

where  $\Delta E_{HOMO}$  is the strain induced shift of the HOMO edges,  $\Delta E_g$  is the bandgap shift,  $N_l(\varepsilon)$  is the effective DoS at the LUMO edges under strain  $\varepsilon$ , and  $m$  ( $\sim 1.2 - 1.4$ ) is the body-effect

coefficient. For a p-type OFET, the band shift of the LUMO edges is very little so that the last term in Equation (3.69) is negligible. The deformation potential theory gives the shifts of HOMO band and bandgap as Equation (3.70),

$$\Delta E_g \approx \Delta E_{HOMO} = \left( \Xi_d + \frac{1}{3} \Xi_u \right) \cdot \text{trace}(\bar{\epsilon}) \quad (3.70)$$

where  $\Xi_d$ ,  $\Xi_u$  are dilation and shear deformation potentials at the HOMO edges.  $\text{trace}(\bar{\epsilon})$  is the trace of the strain tensor. By superposing  $\Delta\mu_{eff}$  and  $\Delta V_{th}$  to  $\mu_{eff}$  and  $V_{th}$  in Equations (3.62) and (3.65), the post-bent transconductance and outputs of a p-type OFET can be simulated. In summary, the pre- and post-bent characteristics can be described by a group of equations including Equations (3.57), (3.62), (3.65), (3.66), (3.68) and (3.69).

### 3.3 Study of Strained OSC Devices Based on Fractional Drift-Diffusion Model

Because charge carriers of many organic semiconductors (OSCs) exhibit fractional drift-diffusion (Fr-DD) transport properties, the need to develop the solver for Fr-DD model (Equations (2.8)-(2.10)) becomes more apparent. However, the current research on solving the governing equations of the Fr-DD model is practically nonexistent. In this study, an iterative solver with high precision was developed to obtain both the transient and steady-state dynamics of OSC devices. The Fr-DD model is composed of two fractional-order carrier (i.e., electron and hole) continuity equations and Poisson's equation. By treating the current density as constants within each pair of consecutive grid nodes, a Caputo's linear fractional differential equation can be produced, and its analytic solution gives an approximation to the carrier concentration. The convergence of the solver is guaranteed by implementing a successive over-relaxation (SOR) mechanism on each loop of Gummel's iteration. Based on this study, it can be shown that the Scharfetter-Gummel discretization method is essentially a special case of the discretization scheme. In addition, the consistency and convergence of the solver's two algorithms were proved, with three numerical examples designed to demonstrate the accuracy and computational performance of the solver. Finally, the Fr-DD model was validated for a steady-state organic field effect transistor (OFET) by fitting the simulated transconductance and output curves to the experimental data.

### 3.3.1 Derivation of the Computational Scheme

Without loss of the generality, the discretization scheme is implemented in a two-dimensional spatial domain. The spatial step size in the  $x$  and  $y$  directions are given by  $\Delta x = L_x/(N_x + 1)$  and  $\Delta y = L_y/(N_y + 1)$ , respectively. The spatial grid points are specified by  $x_i = i\Delta x, i = 0, 1, \dots, N_x + 1$  and  $y_j = j\Delta y, j = 0, 1, \dots, N_y + 1$ . The time step size is given by  $\Delta t = T/N$ , and the temporal grid points are specified by  $t_n = n\Delta t, n = 0, 1, 2, \dots, N$ . The notations utilized in the discretized continuity equations are demonstrated in Figure 3.6. For example, the electron concentration  $n$  at the spatial grid point  $(x_i, y_j)$  and the temporal grid point  $t_k$  is denoted by  $n_{i,j}^k$ . Similar rules apply to the hole concentration  $p$ , two components of the electron current density vector  $(IX, IY)$  and the hole current density vector  $(JX, JY)$ . The discretized current density is specified on the mid-grids, while the electrostatic potentials  $\phi_{i,j}^k$  are specified on the normal grids. If the OSC is inhomogeneous, its dielectric permittivity is not constant so that the discretized dielectric permittivity is specified on mid-grids as well, i.e.,  $\epsilon_{i+1/2,j+1/2}$ .

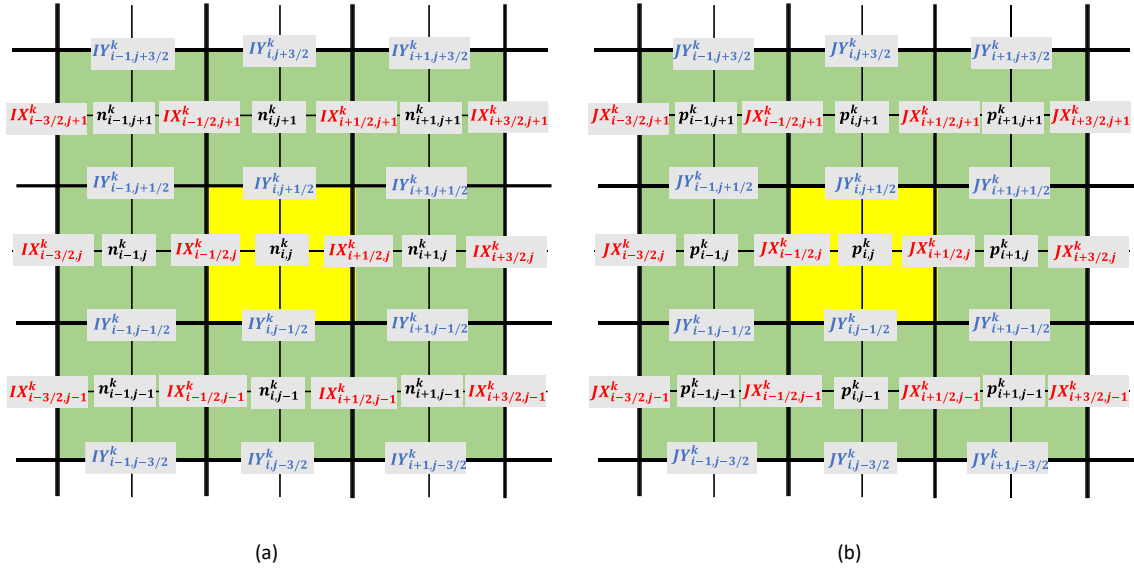


Figure 3.6 An illustration of the discretized (a) electron continuity equation with electron concentration denoted by  $n_{i,j}^k$ ,  $x$ -component of electron current density denoted by  $IX_{i-1/2,j}^k$ , and  $y$ -component of electron current density denoted by  $IY_{i,j-1/2}^k$ ; (b) hole continuity equation with hole concentration denoted by  $p_{i,j}^k$ ,  $x$ -component of hole current density denoted by  $JX_{i-1/2,j}^k$ , and  $y$ -component of hole current density denoted by  $JY_{i,j-1/2}^k$  (Y. Yang et al., 2021b).

### 3.3.1.1 Discretization of Transient-State Fr-DD Model

By applying the second-order finite center difference method, Poisson's equation can be discretized into Equation (3.71),

$$\begin{aligned} & \frac{\tilde{\varepsilon}_{i-1,j}\varphi_{i-1,j}^k - \tilde{\varepsilon}_{i,j,1}\varphi_{i,j}^k + \tilde{\varepsilon}_{i+1,j}\varphi_{i+1,j}^k}{\Delta x^2} + \frac{\tilde{\varepsilon}_{i,j-1}\varphi_{i,j-1}^k - \tilde{\varepsilon}_{i,j,2}\varphi_{i,j}^k + \tilde{\varepsilon}_{i,j+1}\varphi_{i,j+1}^k}{\Delta y^2} \\ & = -q(p_{i,j}^k - n_{i,j}^k) \end{aligned} \quad (3.71)$$

where the generalized dielectric permittivity are given by  $\tilde{\varepsilon}_{i-1,j} = (\varepsilon_{i-1/2,j-1/2} + \varepsilon_{i-1/2,j+1/2})/2$ ,  $\tilde{\varepsilon}_{i+1,j} = (\varepsilon_{i+1/2,j-1/2} + \varepsilon_{i+1/2,j+1/2})/2$ ,  $\tilde{\varepsilon}_{i,j-1} = (\varepsilon_{i+1/2,j-1/2} + \varepsilon_{i-1/2,j-1/2})/2$ ,  $\tilde{\varepsilon}_{i,j+1} = (\varepsilon_{i+1/2,j+1/2} + \varepsilon_{i-1/2,j+1/2})/2$ ,  $\tilde{\varepsilon}_{i,j,1} = \tilde{\varepsilon}_{i-1,j} + \tilde{\varepsilon}_{i+1,j}$ , and  $\tilde{\varepsilon}_{i,j,2} = \tilde{\varepsilon}_{i,j-1} + \tilde{\varepsilon}_{i,j+1}$ , respectively.

For  $i = 1, 2, \dots, N_x$  and  $j = 1, 2, \dots, N_y$ , at each time step  $t_k, k = 1, \dots, N$ , rearranging Equation (3.71) produces  $k$ -th step matrix equation,

$$A_\varphi \varphi^{(k)} = b_\varphi^{(k)} \quad (3.72)$$

where  $A_\varphi \in \mathbb{R}^{N_x N_y \times N_x N_y}$  is a pentadiagonal matrix composed of dielectric permittivity constants,  $\varphi^{(k)} = [\varphi_{1,1}^k, \varphi_{2,1}^k, \dots, \varphi_{N_x, N_y}^k]^T$  is the unknown electrostatic potentials and  $b_\varphi^{(k)} \in \mathbb{R}^{N_x N_y}$  is the known vector including the boundary potentials. Depending on the types of boundary conditions, the electrostatic potentials on the boundary should be updated either repeatedly at each time step or just once at the initial time step. The boundary conditions are given by Equations (3.73) and (3.74),

$$\varphi^k|_{\partial\Omega_D} = f_\varphi(\partial\Omega_D), \quad k = 0, 1, \dots, N \quad (3.73)$$

$$\varphi^k|_{\partial\Omega_N} = g_\varphi(\varphi^{k-1}|_\Omega), \quad k = 0, 1, \dots, N \quad (3.74)$$

where  $f_\varphi(\partial\Omega_D)$  is a known function defined on the Dirichlet boundary  $\partial\Omega_D$ , and  $g_\varphi(\varphi^{k-1}|_\Omega)$  is a known function defined on the interior discrete points, the form of  $g_\varphi$  is given by discretizing the gradient operators along boundary surface normal directions. Equation (3.73) and Equation (3.74) are the Dirichlet condition and the combined Neumann-Robin condition for Poisson's equation, respectively.

In carrier continuity equations, the diffusion coefficients  $D_p, D_n$  and carrier mobilities  $\mu_p, \mu_n$  can be spatially dependent parameters. Nevertheless, in the ensuing derivations,  $D_p, D_n, \mu_p$  and  $\mu_n$  are treated as constants within the whole domain to reduce the indicial complexity. To discretize carrier continuity equations in this study, the current densities between two

consecutive normal grid points are treated as a constant. For instance, at  $(k + 1)$ -th time step, two components of the electron current density vector are given by Equations (3.75) and (3.76),

$$IX_{i-1/2,j}^{k+1} = -q\mu_n n \frac{\partial \varphi}{\partial x} + qD_n \cdot {}_{x_{i-1}}^c \mathcal{D}_x^\beta n \quad (3.75)$$

$$IY_{i,j-1/2}^{k+1} = -q\mu_n n \frac{\partial \varphi}{\partial y} + qD_n \cdot {}_{y_{i-1}}^c \mathcal{D}_y^\beta n \quad (3.76)$$

where  $IX_{i-1/2,j}^{k+1}$  and  $IY_{i,j-1/2}^{k+1}$  are two different constants. Thus, by following Theorem 2.4, the electron concentrations at the two ending grid points can be given as

$$n_{i,j}^{k+1} = \Phi_2(\Delta x) n_{i-1,j}^{k+1} + \frac{IX_{i-1/2,j}^{k+1}}{qD_n} j_{0+}^\beta \Phi_2(\Delta x) \quad (3.77)$$

$$n_{i,j}^{k+1} = \Phi_1(\Delta y) n_{i,j-1}^{k+1} + \frac{IY_{i,j-1/2}^{k+1}}{qD_n} j_{0+}^\beta \Phi_1(\Delta y) \quad (3.78)$$

where  $\Phi_1(t)$  and  $\Phi_2(t)$  are the generalized state transition functions, which are defined as Equations (3.79) and (3.80), respectively.

$$\Phi_1(t) = \mathcal{E}_\beta \left( \frac{\varphi_{i,j}^{k+1} - \varphi_{i,j-1}^{k+1}}{V_T} t^{\beta-1} \right) \quad (3.79)$$

$$\Phi_2(t) = \mathcal{E}_\beta \left( \frac{\varphi_{i,j}^{k+1} - \varphi_{i-1,j}^{k+1}}{V_T} t^{\beta-1} \right) \quad (3.80)$$

Rearranging Equations (3.77) and (3.78), the discretized current densities can be obtained as Equations

$$IX_{i-1/2,j}^{k+1} = \frac{(n_{i,j}^{k+1} - \Phi_2(\Delta x) n_{i-1,j}^{k+1}) q D_n}{j_{0+}^\beta \Phi_2(\Delta x)} \quad (3.81)$$

$$IY_{i,j-1/2}^{k+1} = \frac{(n_{i,j}^{k+1} - \Phi_1(\Delta y) n_{i,j-1}^{k+1}) q D_n}{j_{0+}^\beta \Phi_1(\Delta y)} \quad (3.82)$$

Next, when the second-order finite center difference method is applied to approximate the divergence of electron current densities, it produces

$$(\nabla \cdot I)_{i,j}^{k+1} \approx \frac{IX_{i+1/2,j}^{k+1} - IX_{i-1/2,j}^{k+1}}{\Delta x} + \frac{IY_{i,j+1/2}^{k+1} - IY_{i,j-1/2}^{k+1}}{\Delta y} \quad (3.83)$$

By substituting Equations (3.81), (3.82) and relevant expressions for  $IX_{i+1/2,j}^{k+1}$ ,  $IY_{i,j+1/2}^{k+1}$  into Equation (3.83), the discrete current divergence  $(\nabla \cdot I)_{i,j}^{k+1}$  can be expressed in terms of  $n_{i-1,j}^{k+1}$ ,  $n_{i,j-1}^{k+1}$ ,  $n_{i,j}^{k+1}$ ,  $n_{i,j+1}^{k+1}$  and  $n_{i+1,j}^{k+1}$ . Then, substitute the expression of  $(\nabla \cdot I)_{i,j}^{k+1}$  and Equation



(2.32) into Equation (2.9), the discrete form of the electron continuity equation can be obtained in Equation (3.84),

$$\begin{aligned} \frac{1}{\Gamma(2-\alpha)} \sum_{m=0}^k \frac{n_{i,j}^{k+1-m} - n_{i,j}^{k-m}}{\Delta t^\alpha} b_{m,k+1}^{(\alpha)} \\ = C_{i,j-1}^{k+1} n_{i,j-1}^{k+1} + C_{i-1,j}^{k+1} n_{i-1,j}^{k+1} + C_{i,j}^{k+1} n_{i,j}^{k+1} + C_{i+1,j}^{k+1} n_{i+1,j}^{k+1} \\ + C_{i,j+1}^{k+1} n_{i,j+1}^{k+1} + G_n \end{aligned} \quad (3.84)$$

where  $b_{m,k+1}^{(\alpha)} = (m+1)^{1-\alpha} - m^{1-\alpha}$ , and coefficients  $C_{i,j-1}^{k+1}$ ,  $C_{i-1,j}^{k+1}$ ,  $C_{i,j}^{k+1}$ ,  $C_{i+1,j}^{k+1}$  and  $C_{i,j+1}^{k+1}$  are given in Equations (3.85)-(3.89).

$$C_{i,j-1}^{k+1} = \frac{\Phi_1(\Delta y)}{J_{0+}^\beta \Phi_1(\Delta y)} \frac{D_n}{\Delta y} \quad (3.85)$$

$$C_{i-1,j}^{k+1} = \frac{\Phi_2(\Delta x)}{J_{0+}^\beta \Phi_2(\Delta x)} \frac{D_n}{\Delta x} \quad (3.86)$$

$$C_{i,j}^{k+1} = \left[ -\frac{1}{J_{0+}^\beta \Phi_2(\Delta x)} - \frac{\Phi_3(\Delta x)}{J_{0+}^\beta \Phi_3(\Delta x)} \right] \frac{D_n}{\Delta x} + \left[ -\frac{1}{J_{0+}^\beta \Phi_1(\Delta y)} - \frac{\Phi_4(\Delta y)}{J_{0+}^\beta \Phi_4(\Delta y)} \right] \frac{D_n}{\Delta y} \quad (3.87)$$

$$C_{i+1,j}^{k+1} = \frac{1}{J_{0+}^\beta \Phi_3(\Delta x)} \frac{D_n}{\Delta x} \quad (3.88)$$

$$C_{i,j+1}^{k+1} = \frac{1}{J_{0+}^\beta \Phi_4(\Delta y)} \frac{D_n}{\Delta y} \quad (3.89)$$

Similar to  $\Phi_1(t)$  and  $\Phi_2(t)$  in Equations (3.79) and (3.80), the generalized state transition functions  $\Phi_3(t)$  and  $\Phi_4(t)$  are defined as

$$\Phi_3(t) = \varepsilon_\beta \left( \frac{\varphi_{i+1,j}^{k+1} - \varphi_{i,j}^{k+1}}{V_T} t^{\beta-1} \right) \quad (3.90)$$

$$\Phi_4(t) = \varepsilon_\beta \left( \frac{\varphi_{i,j+1}^{k+1} - \varphi_{i,j}^{k+1}}{V_T} t^{\beta-1} \right) \quad (3.91)$$

Follow Equation (2.31), the fractional integrals  $J_{0+}^\beta \Phi_1(\Delta y)$  can be approximated by Equation (3.92). Other fractional integrals  $J_{0+}^\beta \Phi_2(\Delta x)$ ,  $J_{0+}^\beta \Phi_3(\Delta x)$ , and  $J_{0+}^\beta \Phi_4(\Delta y)$  can be approximated similarly.

$$\begin{aligned}
j_{0+}^\beta \Phi_1(\Delta y) &= \frac{(\Delta y)^\beta}{2\Gamma(\beta)} \left[ \left( 1 - 2\Phi_1\left(\frac{\Delta y}{2}\right) + \Phi_1(\Delta y) \right) \left( \frac{4}{\beta} - \frac{8}{\beta+1} + \frac{4}{\beta+2} \right) \right. \\
&\quad \left. - \left( -3 - 4\Phi_1\left(\frac{\Delta y}{2}\right) + \Phi_1(\Delta y) \right) \left( \frac{2}{\beta} - \frac{2}{\beta+1} \right) - \frac{4}{\beta} \right]
\end{aligned} \tag{3.92}$$

By reference to the derivation of Equation (3.84), the discrete form to the hole continuity equation is given by Equation (3.93),

$$\begin{aligned}
\frac{1}{\Gamma(2-\alpha)} \sum_{m=0}^k \frac{p_{i,j}^{k+1-m} - p_{i,j}^{k-m}}{\Delta t^\alpha} b_{m,k+1}^{(\alpha)} \\
= D_{i,j-1}^{k+1} p_{i,j-1}^{k+1} + D_{i-1,j}^{k+1} p_{i-1,j}^{k+1} + D_{i,j}^{k+1} p_{i,j}^{k+1} + D_{i+1,j}^{k+1} p_{i+1,j}^{k+1} \\
+ D_{i,j+1}^{k+1} p_{i,j+1}^{k+1} + G_p
\end{aligned} \tag{3.93}$$

where the coefficients  $D_{i,j-1}^{k+1}$ ,  $D_{i-1,j}^{k+1}$ ,  $D_{i,j}^{k+1}$ ,  $D_{i+1,j}^{k+1}$  and  $D_{i,j+1}^{k+1}$  are given in Equations (3.94)-(3.98),

$$D_{i,j-1}^{k+1} = \frac{\widehat{\Phi}_1(\Delta y)}{j_{0+}^\beta \widehat{\Phi}_1(\Delta y)} \frac{D_p}{\Delta y} \tag{3.94}$$

$$D_{i-1,j}^{k+1} = \frac{\widehat{\Phi}_2(\Delta x)}{j_{0+}^\beta \widehat{\Phi}_2(\Delta x)} \frac{D_p}{\Delta x} \tag{3.95}$$

$$D_{i,j}^{k+1} = \left[ -\frac{1}{j_{0+}^\beta \widehat{\Phi}_2(\Delta x)} - \frac{\widehat{\Phi}_3(\Delta x)}{j_{0+}^\beta \widehat{\Phi}_3(\Delta x)} \right] \frac{D_p}{\Delta x} + \left[ -\frac{1}{j_{0+}^\beta \widehat{\Phi}_1(\Delta y)} - \frac{\widehat{\Phi}_4(\Delta y)}{j_{0+}^\beta \widehat{\Phi}_4(\Delta y)} \right] \frac{D_p}{\Delta y} \tag{3.96}$$

$$D_{i+1,j}^{k+1} = \frac{1}{j_{0+}^\beta \widehat{\Phi}_3(\Delta x)} \frac{D_p}{\Delta x} \tag{3.97}$$

$$D_{i,j+1}^{k+1} = \frac{1}{j_{0+}^\beta \widehat{\Phi}_4(\Delta y)} \frac{D_p}{\Delta y} \tag{3.98}$$

and the generalized reversed state transition functions  $\widehat{\Phi}_1(t)$ ,  $\widehat{\Phi}_2(t)$ ,  $\widehat{\Phi}_3(t)$  and  $\widehat{\Phi}_4(t)$  are defined by Equations (3.99)-(3.102).

$$\widehat{\Phi}_1(t) = \varepsilon_\beta \left( -\frac{\varphi_{i,j}^{k+1} - \varphi_{i,j-1}^{k+1}}{V_T} t^{\beta-1} \right) \tag{3.99}$$

$$\widehat{\Phi}_2(t) = \varepsilon_\beta \left( -\frac{\varphi_{i,j}^{k+1} - \varphi_{i-1,j}^{k+1}}{V_T} t^{\beta-1} \right) \tag{3.100}$$

$$\hat{\Phi}_3(t) = \varepsilon_\beta \left( -\frac{\varphi_{i+1,j}^{k+1} - \varphi_{i,j}^{k+1}}{V_T} t^{\beta-1} \right) \quad (3.101)$$

$$\hat{\Phi}_4(t) = \varepsilon_\beta \left( -\frac{\varphi_{i,j+1}^{k+1} - \varphi_{i,j}^{k+1}}{V_T} t^{\beta-1} \right) \quad (3.102)$$

Both the discrete-form electron continuity equation (Equation (3.84)) and the discrete form hole continuity equation (Equation (3.93)) can be represented in matrix forms, i.e., Equations (3.103) and (3.104),

$$A_n^{(k+1)} n^{(k+1)} = b_n^{(k+1)} \quad (3.103)$$

$$A_p^{(k+1)} p^{(k+1)} = b_p^{(k+1)} \quad (3.104)$$

where  $A_n^{(k+1)}$ ,  $A_p^{(k+1)}$  are two pentadiagonal matrices,  $n^{(k+1)}$ ,  $p^{(k+1)}$  are the unknown electron and hole concentrations within the interior domain at the  $(k+1)$ -th time step,  $b_n^{(k+1)}$ ,  $b_p^{(k+1)}$  are known vectors containing the information about the boundary points and the previous  $k$  steps. The boundary conditions and the initial value conditions for carrier continuity equations are given by Equations (3.105)-(3.107),

$$n^k|_{\partial\Omega_D} = f_n(\partial\Omega_D), \quad n^k|_{\partial\Omega_N} = g_n(n^{k-1}|_\Omega), \quad k = 0, 1, \dots, N \quad (3.105)$$

$$p^k|_{\partial\Omega_D} = f_p(\partial\Omega_D), \quad p^k|_{\partial\Omega_N} = g_p(p^{k-1}|_\Omega), \quad k = 0, 1, \dots, N \quad (3.106)$$

$$\begin{aligned} n_{i,j}^0 &= h_n(x_i, y_j), \quad p_{i,j}^0 = h_p(x_i, y_j), \\ i &= 0, 1, \dots, N_x + 1; j = 0, 1, \dots, N_y + 1 \end{aligned} \quad (3.107)$$

where  $f_n, f_p$  are known functions to account for Dirichlet conditions, and  $g_n, g_p$  are known functions to represent combined Neumann-Robin conditions.

Given the discrete forms and the relevant boundary conditions, a novel algorithm is proposed and formatted in Algorithm 1 to solve the numerical solutions of the transient-state Fr-DD model (Equations (2.8)-(2.10)).

---

**Algorithm 1:** To evaluate the numerical solution of the transient-state Fr-DD model

---

**Input:** Constant damping parameters  $\omega_n, \omega_p \in [0,1]$ ; Initial guess  $^{(0)}n_{i,j}^k$  and  $^{(0)}p_{i,j}^k$  for  $i = 1, 2, \dots, N_x; j = 1, 2, \dots, N_y; k = 1, \dots, N$

**Output:** Unknown interior variables at each time step  $\varphi_{i,j}^k, n_{i,j}^k, p_{i,j}^k$  for  $i = 1, 2, \dots, N_x; j = 1, 2, \dots, N_y; k = 0, 1, \dots, N$

**Step-1.0** Obtain initial potentials  $\varphi_{i,j}^0$  by solving Equation (3.72). The initial values of the electron and hole concentrations are given in Equation (3.107), and the boundary conditions for electrostatic potentials are in Equations (3.73) and (3.74)

**For** number of each time step  $k = 0, 1, \dots, N - 1$ , **do**

Initialize Gummel iteration count  $g = 0$ , old error  $err_0 = 1$ , and divergence count  $d = 0$ .

**While**  $err > Tol$ , **do** Gummel iterations

**Step-1.1** Generate  $^{(g)}\varphi_{i,j}^{k+1}$  by solving Equation (3.72) with the initial guess  $^{(g)}n_{i,j}^{k+1}$ ,  $^{(g)}p_{i,j}^{k+1}$  and the boundary conditions in Equations (3.73) and (3.74)

**Step-1.2** Generate  $^{(g+1)}n_{i,j}^{k+1}$ ,  $^{(g+1)}p_{i,j}^{k+1}$  by solving Equations (3.103) and (3.104) with Equations (3.105) and (3.106) and  $n_{i,j}^l, p_{i,j}^l$ , where  $l = 0, 1, \dots, k$ .

**Step-1.3** Update  $^{(g+1)}n_{i,j}^{k+1} = \omega_n \cdot ^{(g+1)}n_{i,j}^{k+1} + (1 - \omega_n) \cdot ^{(g)}n_{i,j}^{k+1}$  and  $^{(g+1)}p_{i,j}^{k+1} = \omega_p \cdot ^{(g+1)}p_{i,j}^{k+1} + (1 - \omega_p) \cdot ^{(g)}p_{i,j}^{k+1}$  to improve the convergence rate

**Step-1.4** Compute error  $err_1 = \left\| \frac{^{(g+1)}n_{i,j}^{k+1} - ^{(g)}n_{i,j}^{k+1}}{^{(g)}n_{i,j}^{k+1}} \right\|$ ,  $err_2 = \left\| \frac{^{(g+1)}p_{i,j}^{k+1} - ^{(g)}p_{i,j}^{k+1}}{^{(g)}p_{i,j}^{k+1}} \right\|$  and  $err = \max(err_1, err_2)$ . Update iteration count  $g = g + 1$

**Step-1.5** **If**  $err > err_0$

Update divergence counts  $d = d + 1$  and old error  $err_0 = err$

**Step-1.6** **If**  $d > 1000$

Update damping parameter  $\omega_n = \omega_n/2$  and  $\omega_p = \omega_p/2$  to improve the convergence performance, then reset divergence count  $d = 0$

---

---

**Algorithm 2:** To evaluate the numerical solution of the steady-state Fr-DD model

---

**Input:** Constant damping parameters  $\omega_n, \omega_p \in [0,1]$ ; Initial guess  $^{(0)}n_{i,j}$  and  $^{(0)}p_{i,j}$  for  $i = 1, 2, \dots, N_x; j = 1, 2, \dots, N_y$

**Output:** Unknown interior variables in steady state  $\phi_{i,j}, n_{i,j}, p_{i,j}$  for  $i = 1, 2, \dots, N_x; j = 1, 2, \dots, N_y$

Initialize Gummel iteration count  $g = 0$ , old error  $err_0 = 1$ , and divergence count  $d = 0$

**While**  $err > Tol$ , **do** Gummel iterations

**Step-1.1** Generate  $^{(g)}\phi_{i,j}$  by solving Equation (3.72) with the initial guess  $^{(g)}n_{i,j}, ^{(g)}p_{i,j}$  and the boundary conditions of potentials in Equations (3.73) and (3.74)

**Step-1.2** Generate second guess  $^{(g+1)}n_{i,j}, ^{(g+1)}p_{i,j}$  by solving Equations (3.108) and (3.109) with relevant boundary conditions

**Step-1.3** Update  $^{(g+1)}n_{i,j} = \omega_n \cdot ^{(g+1)}n_{i,j} + (1 - \omega_n) \cdot ^{(g)}n_{i,j}$  and  $^{(g+1)}p_{i,j} = \omega_p \cdot ^{(g+1)}p_{i,j} + (1 - \omega_p) \cdot ^{(g)}p_{i,j}$  to improve the convergence rate

**Step-1.4** Compute error  $err_1 = \left\| \frac{^{(g+1)}n_{i,j} - ^{(g)}n_{i,j}}{^{(g)}n_{i,j}} \right\|$ ,  $err_2 = \left\| \frac{^{(g+1)}p_{i,j} - ^{(g)}p_{i,j}}{^{(g)}p_{i,j}} \right\|$  and  $err = \max(err_1, err_2)$ . Update iteration counts  $g = g + 1$

**Step-1.5** **If**  $err > err_0$

Update divergence counts  $d = d + 1$  and old error  $err_0 = err$ .

**Step-1.6** **If**  $d > 1000$

Update damping parameter  $\omega_n = \omega_n/2$  and  $\omega_p = \omega_p/2$  to improve the convergence performance, then reset divergence counts  $d = 0$

---

### 3.3.1.2 Discretization of Steady-State Fr-DD Model

Since Caputo's fractional derivative of any constant is zero, the time-derivative terms in the carrier continuity equations vanishes in the steady state. Referring to the derivation of the discrete forms of the transient-state Fr-DD model, the discrete forms of the steady-state Fr-DD model are given by Equations (3.108) and (3.109).

$$C_{i,j-1}^{k+1}n_{i,j-1}^{k+1} + C_{i-1,j}^{k+1}n_{i-1,j}^{k+1} + C_{i,j}^{k+1}n_{i,j}^{k+1} + C_{i+1,j}^{k+1}n_{i+1,j}^{k+1} + C_{i,j+1}^{k+1}n_{i,j+1}^{k+1} = -G_n \quad (3.108)$$

$$D_{i,j-1}^{k+1}p_{i,j-1}^{k+1} + D_{i-1,j}^{k+1}p_{i-1,j}^{k+1} + D_{i,j}^{k+1}p_{i,j}^{k+1} + D_{i+1,j}^{k+1}p_{i+1,j}^{k+1} + D_{i,j+1}^{k+1}p_{i,j+1}^{k+1} = -G_p \quad (3.109)$$

The boundary conditions for Poisson's equation and the carrier continuity equations are exactly the same as the ones in the transient-state Fr-DD model. Rearranging Equations (3.71), (3.108) and (3.109), three matrix equations can be obtained:  $A_\varphi \varphi = b_\varphi$ ,  $A_n n = b_n$  and  $A_p p = b_p$ . Algorithm 2 presents a complete procedure to evaluate the numerical solutions to the steady-state Fr-DD model.

### 3.3.1.3 Special Case When $\alpha = 1$ and $\beta = 1$

When  $\alpha = 1$  and  $\beta = 1$ , the Fr-DD model degenerates into the conventional DD model which is widely used in the modeling of single crystalline ISCs (e.g., Si, Ge, etc.). It can be easily verified that in the case of  $\alpha = \beta = 1$ , Equations (3.84) and (3.93) become Equations (3.110) and (3.111),

$$\begin{aligned} \frac{n_{i,j}^{k+1} - n_{i,j}^k}{\Delta t} = & -\frac{\mu_n V_T}{\Delta x^2} [\mathcal{B}_{(i-1,i),j}^{k+1} n_{i-1,j}^{k+1} - (\mathcal{B}_{(i,i-1),j}^{k+1} + \mathcal{B}_{(i,i+1),j}^{k+1}) n_{i,j}^{k+1} \\ & + \mathcal{B}_{(i+1,i),j}^{k+1} n_{i+1,j}^{k+1}] \\ & -\frac{\mu_n V_T}{\Delta y^2} [\mathcal{B}_{i,(j-1),j}^{k+1} n_{i,j-1}^{k+1} - (\mathcal{B}_{i,(j,j-1)}^{k+1} + \mathcal{B}_{i,(j,j+1)}^{k+1}) n_{i,j}^{k+1} \\ & + \mathcal{B}_{i,(j+1),j}^{k+1} n_{i,j+1}^{k+1}] + G_n \end{aligned} \quad (3.110)$$

$$\begin{aligned} \frac{p_{i,j}^{k+1} - p_{i,j}^k}{\Delta t} = & \frac{\mu_p V_T}{\Delta x^2} [\mathcal{B}_{(i,i-1),j}^{k+1} p_{i-1,j}^{k+1} - (\mathcal{B}_{(i-1,i),j}^{k+1} + \mathcal{B}_{(i+1,i),j}^{k+1}) p_{i,j}^{k+1} \\ & + \mathcal{B}_{(i,i+1),j}^{k+1} p_{i+1,j}^{k+1}] \\ & + \frac{\mu_p V_T}{\Delta y^2} [\mathcal{B}_{i,(j,j-1)}^{k+1} p_{i,j-1}^{k+1} - (\mathcal{B}_{i,(j-1),j}^{k+1} + \mathcal{B}_{i,(j+1),j}^{k+1}) p_{i,j}^{k+1} \\ & + \mathcal{B}_{i,(j,j+1)}^{k+1} p_{i,j+1}^{k+1}] + G_p \end{aligned} \quad (3.111)$$

where the new coefficients are defined as  $\mathcal{B}_{(n,m),j}^{k+1} = \mathcal{B}\left(\frac{\varphi_{n,j}^{k+1} - \varphi_{m,j}^{k+1}}{V_T}\right)$  and  $\mathcal{B}_{i,(n,m)}^{k+1} =$

$\mathcal{B}\left(\frac{\varphi_{i,n}^{k+1} - \varphi_{i,m}^{k+1}}{V_T}\right)$ , in which  $\mathcal{B}(x) = \frac{x}{\exp(x)-1}$  is the Bernoulli function. It happens to realize that

Equations (3.110) and (3.111) are identical to the discrete forms derived from the Scharfetter-

Gummel method (Tan et al., 1989). Algorithm 1 and Algorithm 2 can be modified accordingly to solve the numerical solutions of the conventional DD model.

### 3.3.2 Consistency and Convergence Analysis

The following two sections discussed the consistency and convergence of the computational scheme developed for the transient-state Fr-DD model.

#### 3.3.2.1 Consistency of the Computational Scheme

The proposed computational scheme is consistent if the truncation error can be made to vanish as the mesh and time step sizes are reduced to zero. First of all, the consistency of the schemes obtained through the finite center difference method has been proved (Moin, 2010). Furthermore, it can be inferred from Lemma 2.5 and Lemma 2.6 that the truncation error of the discretized carrier continuity equations will also vanish as the spatial and time step sizes shrink to zero. Nevertheless, Equation (2.21) implies that the truncation error may be produced by the composing of Caputo's fractional derivative with an integer-order gradient operator. To test the influence of this newly generated truncation error on the consistency of Equations (3.84) and (3.93), Theorem 4.1 is proposed to give an evaluation of the shrinking order of the truncation error with respect to the spatial step sizes.

**Theorem 3.1** *Consider the two-dimensional divergence terms  $\nabla \cdot I$  and  $\nabla \cdot J$  in Equations (2.9) and (2.10) with  $I = -q\mu_n n \nabla \varphi + qD_n {}^C\nabla_r^\beta n$  and  $J = -q\mu_p p \nabla \varphi - qD_p {}^C\nabla_r^\beta p$ , then the following equations hold for  $0 < \beta < 1$ ,*

$$\begin{aligned} \nabla \cdot I = & -q\mu_n (n\Delta\varphi + \nabla n \cdot \nabla\varphi) + qD_n {}^C\nabla_r^{\beta+1} n + \nabla \\ & \cdot \left[ \frac{\left[\frac{\partial n}{\partial x}\right]_0 x^{1-\beta}}{\Gamma(2-\beta)} i_x + \frac{\left[\frac{\partial n}{\partial y}\right]_0 y^{1-\beta}}{\Gamma(2-\beta)} i_y \right] \end{aligned} \quad (3.112)$$

$$\begin{aligned} \nabla \cdot J = & -q\mu_p (p\Delta\varphi + \nabla p \cdot \nabla\varphi) - qD_p {}^C\nabla_r^{\beta+1} p - \nabla \\ & \cdot \left[ \frac{\left[\frac{\partial p}{\partial x}\right]_0 x^{1-\beta}}{\Gamma(2-\beta)} i_x + \frac{\left[\frac{\partial p}{\partial y}\right]_0 y^{1-\beta}}{\Gamma(2-\beta)} i_y \right] \end{aligned} \quad (3.113)$$

where  $i_x, i_y$  are unit vector in the  $x$  and  $y$  direction.

**Proof.** Since Equations (3.112) and (3.113) are similar to each other, it is sufficient to prove Equation (3.112) only. From Equation (2.17), it implies that

$${}_0^C\mathcal{D}_x^\beta(n(x, y)) = {}^{RL}_0\mathcal{D}_x^\beta(n(x, y)) - \frac{n(0, y)}{\Gamma(1 - \beta)}x^{-\beta} \quad (3.114)$$

Taking the first derivative on both sides of Equation (3.114) gives

$$\frac{\partial[{}_0^C\mathcal{D}_x^\beta(n(x, y))]}{\partial x} = {}^{RL}_0\mathcal{D}_x^{\beta+1}(n(x, y)) + \frac{\beta n(0, y)}{\Gamma(1 - \beta)}x^{-\beta-1} \quad (3.115)$$

According to Equation (2.17),  ${}^{RL}_0\mathcal{D}_x^{\beta+1}(n(x, y))$  can be expanded as

$${}^{RL}_0\mathcal{D}_x^{\beta+1}(n(x, y)) = {}_0^C\mathcal{D}_x^{\beta+1}(n(x, y)) + \frac{n(0, y)}{\Gamma(-\beta)}x^{-(\beta+1)} + \frac{\frac{\partial n}{\partial x}\big|_0}{\Gamma(1 - \beta)}x^{-\beta} \quad (3.116)$$

Substitute Equation (3.116) into Equation (3.115), and given that  $\Gamma(1 - \beta) = -\beta\Gamma(-\beta)$ , it gives

$$\frac{\partial[{}_0^C\mathcal{D}_x^\beta(n(x, y))]}{\partial x} = {}_0^C\mathcal{D}_x^{\beta+1}(n(x, y)) + \frac{\frac{\partial n}{\partial x}\big|_0}{\Gamma(1 - \beta)}x^{-\beta} \quad (3.117)$$

Then, it can be easily verified that Equation (3.112) is a corollary to Equation, which completes the proof.

In the derivation of Equations (3.84) and (3.93), the current densities  $I$  and  $J$  are treated as constants to solve the Caputo's fractional differential equation defined in the interval between two grid points. Theorem 3.1 can be applied to get Equation (3.118),

$$\begin{aligned} \nabla \cdot \left[ \bar{I} - \frac{\frac{\partial n}{\partial x}\big|_{x_i}}{\Gamma(2 - \beta)}i_x - \frac{\frac{\partial n}{\partial y}\big|_{y_j}}{\Gamma(2 - \beta)}i_y \right] \\ = \left[ -q\mu_n(n\Delta\varphi + \nabla n \cdot \nabla\varphi) + qD_n {}^C\nabla_r^{\beta+1}n \right]_{i,j} \end{aligned} \quad (3.118)$$

where  $\bar{I} = X_{i+1/2,j} \cdot i_x + IY_{i,j+1/2} \cdot i_y$  is the electron current density vector. Equation (3.118) shows that the discretized current density can be composed with an integer-order gradient operator from its left side to leave a vanishing truncation error. By forcing  $\Delta x, \Delta y \rightarrow 0$ , the truncation error will decay to a fractional order of  $1 - \beta$ . Therefore, the consistency of the computational scheme is proved.



### 3.3.2.2 Convergence of the Computational Scheme

For convenience, the convergence analysis is only performed on Algorithm 2, but the analysis also applies to Algorithm 1 since Algorithm 2 can be treated as an independent time step of Algorithm 1. Consider a finite dimensional vector space  $V := \{\varphi \in \mathbb{R}^{N_x N_y} : \|\varphi\|_\infty < \infty\}$  and a product vector space  $Y := \{[n, p] \in \mathbb{R}^{N_x N_y} \times \mathbb{R}^{N_x N_y} : \|n\|_\infty < \infty, \|p\|_\infty < \infty\}$ , the Gummel mapping is defined as  $\mathcal{A} : Y \rightarrow V \times Y$ , which relates the pair  $[n_1, p_1]$  to the triple  $(\varphi, n_2, p_2)$ . Under these settings, Gummel mapping in Algorithm 2 can be represented by three linear matrix expressions computed in a serial order,

$$A_\varphi \cdot {}^{(g)}\varphi = b_\varphi({}^{(g)}n, {}^{(g)}p, \varphi|_{\partial\Omega}) \quad (3.119)$$

$$A_n({}^{(g)}\varphi) \cdot {}^{(g+1)}\hat{n} = b_n({}^{(g)}\varphi, n|_{\partial\Omega}) \quad (3.120)$$

$$A_p({}^{(g)}\varphi) \cdot {}^{(g+1)}\hat{p} = b_p({}^{(g)}\varphi, p|_{\partial\Omega}) \quad (3.121)$$

where  $({}^{(g)}\varphi, {}^{(g+1)}n, {}^{(g+1)}p) = \mathcal{A}[{}^{(g)}n, {}^{(g)}p]$ . Next, it remains to show that Gummel mapping is a contraction mapping with contraction constant  $L < 1$ . Because if so, the fixed point theorem will guarantee the convergence of the computational scheme.

**Theorem 4.2** *Gummel mapping  $\mathcal{A}$  is a contraction mapping if we consider the successively over relaxation mechanism in each step of the Gummel iterations.*

**Proof.** Substitute  ${}^{(g)}\varphi$  into Equations (3.120) and (3.121), it gives Equations (3.122) and (3.123).

$${}^{(g+1)}\hat{n} = A_n^{-1}(A_\varphi^{-1}b_\varphi({}^{(g)}n, {}^{(g)}p, \varphi|_{\partial\Omega}))b_n(A_\varphi^{-1}b_\varphi({}^{(g)}n, {}^{(g)}p, \varphi|_{\partial\Omega}), n|_{\partial\Omega}) \quad (3.122)$$

$${}^{(g+1)}\hat{p} = A_p^{-1}(A_\varphi^{-1}b_\varphi({}^{(g)}n, {}^{(g)}p, \varphi|_{\partial\Omega}))b_p(A_\varphi^{-1}b_\varphi({}^{(g)}n, {}^{(g)}p, \varphi|_{\partial\Omega}), p|_{\partial\Omega}) \quad (3.123)$$

By implementing the successive over relaxation mechanism, the carrier concentrations can be updated via Equations (3.124) and (3.125).

$$\begin{aligned} & {}^{(g+1)}n \\ &= \omega_n \cdot A_n^{-1}(A_\varphi^{-1}b_\varphi({}^{(g)}n, {}^{(g)}p, \varphi|_{\partial\Omega}))b_n(A_\varphi^{-1}b_\varphi({}^{(g)}n, {}^{(g)}p, \varphi|_{\partial\Omega}), n|_{\partial\Omega}) \\ &+ (1 - \omega_n) \cdot {}^{(g)}n \end{aligned} \quad (3.124)$$

$$\begin{aligned} & {}^{(g+1)}p \\ &= \omega_p \cdot A_p^{-1}(A_\varphi^{-1}b_\varphi({}^{(g)}n, {}^{(g)}p, \varphi|_{\partial\Omega}))b_p(A_\varphi^{-1}b_\varphi({}^{(g)}n, {}^{(g)}p, \varphi|_{\partial\Omega}), p|_{\partial\Omega}) \\ &+ (1 - \omega_p) \cdot {}^{(g)}p \end{aligned} \quad (3.125)$$

Take quotient on both sides of Equations (3.124) and (3.125) and apply the triangular inequality, it yields

$$\begin{aligned} & \|\mathcal{A}\| \\ & \leq \omega_n \frac{\left\| A_n^{-1} \left( A_\varphi^{-1} b_\varphi \left( {}^{(g)}n, {}^{(g)}p, \varphi|_{\partial\Omega} \right) \right) b_n \left( A_\varphi^{-1} b_\varphi \left( {}^{(g)}n, {}^{(g)}p, \varphi|_{\partial\Omega} \right), n|_{\partial\Omega} \right) \right\|}{\|{}^{(g)}n\|} \end{aligned} \quad (3.126)$$

$$\begin{aligned} & + 1 - \omega_n \\ & \|\mathcal{A}\| \\ & \leq \omega_p \frac{\left\| A_p^{-1} \left( A_\varphi^{-1} b_\varphi \left( {}^{(g)}n, {}^{(g)}p, \varphi|_{\partial\Omega} \right) \right) b_p \left( A_\varphi^{-1} b_\varphi \left( {}^{(g)}n, {}^{(g)}p, \varphi|_{\partial\Omega} \right), p|_{\partial\Omega} \right) \right\|}{\|{}^{(g)}p\|} \end{aligned} \quad (3.127)$$

$$+ 1 - \omega_p$$

Since the relative sizes of  ${}^{(g+1)}\hat{n}$  and  ${}^{(g+1)}\hat{p}$  to  ${}^{(g)}n$  and  ${}^{(g)}p$  are indeterminable, the following two cases are considered: In the case of  $\|{}^{(g+1)}\hat{n}\| \geq \|{}^{(g)}n\|$  and  $\|{}^{(g+1)}\hat{p}\| \geq \|{}^{(g)}p\|$ , step 1.4, 1.5 and 1.6 in Algorithm 2 imply that  $\omega_n, \omega_p \rightarrow 0$  for divergence count  $d$  exceeds 1000. Thus,  $\|\mathcal{A}\| \leq 1$  and the Gummel iteration converges in large  $g$ . In another case when  $\|{}^{(g+1)}\hat{n}\| < \|{}^{(g)}n\|$  or  $\|{}^{(g+1)}\hat{p}\| < \|{}^{(g)}p\|$ , it can be inferred from Equations (3.126) and (3.127) that  $\|\mathcal{A}\| < 1$ .

### 3.3.3 Study of Strain Effects on the Fractional Parameters

From Equations (2.8)-(2.10), it can be found that the Fr-DD model has at most two parameters that can be freely adjusted, one being the order of the fractional time-derivative  $\alpha$  and the other being the order of the fractional spatial derivative  $\beta$  in the diffusive current density term. However, for the steady-state Fr-DD model, the only parameter that can be freely adjusted is  $\beta$ . Because the steady-state transconductance and output characteristics of OFETs are the focus of this study, there is a strong need to establish the coupling between  $\beta$  and the mechanical strain  $\bar{\epsilon}$ . Consider the hole current density function defined in Equation (3.128),

$$J = -q\mu_p p \nabla \varphi - qD_p {}^c\nabla_r^\beta p \quad (3.128)$$

where the drifting current  $J_{drift}$  is defined by  $J_{drift} = -q\mu_p p \nabla \varphi$  and the diffusive current  $J_{diff}$  is defined by  $J_{diff} = -qD_p {}^c\nabla_r^\beta p$ . By applying a low-precision approximation to Caputo's fractional gradient operator, the diffusive current density can be approximated by

$$J_{diff} \approx -qD_p \frac{\Delta p}{\Delta y^\beta} \quad (3.129)$$

By inspecting Equation (3.129), it can be found that the diffusive current density is inversely proportional to the spatial step size to the power of  $\beta$ . Assume that the spatial step size satisfies  $\Delta y \ll 1$  and the unit-step drop of the hole concentration  $\Delta p$  remains unchanged under different  $\beta$ , the following inequality holds for  $\beta_1 < 1 < \beta_2$ .

$$\frac{\Delta p}{\Delta y^{\beta_1}} < \frac{\Delta p}{\Delta y} < \frac{\Delta p}{\Delta y^{\beta_2}} \quad (3.130)$$

From Equation (3.130), it implies that smaller  $\beta$  is directly related to a smaller diffusive current density (weaker diffusive intensity) in the bulk semiconductor, and vice versa.

The mechanical strain/stress can alter the carrier diffusivity of the semiconductors. This phenomenon has been observed and studied by multiple researches, such as the simulation and modeling of strain-dependent diffusion in composite materials (Klepach & Zohdi, 2014), the influence of mechanical strain on the diffusion activities of amorphous Zr alloys (A. Y. Lee et al., 2017), the influence of hydrostatic stress on Silicon's diffusion (M. J. Aziz, 1998), and the effects of hydrostatic compressive stress on the diffusion of B and Sb in Si and Si-Ge alloys (Aziz et al., 2006). Since mechanical strain can modify carrier diffusivity, and  $\beta$  can directly reflect the carrier diffusive intensity, it is necessary for this study to develop a model to correlate  $\beta$  and mechanical strain  $\varepsilon$ .

Assume that the fractional parameter,  $\beta$ , is a function of the mechanical deformation in general, and specifically a function of the average strain  $\varepsilon$  on the semiconductor-dielectric interface as  $\beta = B(\varepsilon)$ , some simple arguments should be specified to construct the function B. For instance, if the material at the semiconductor-dielectric interface (inside the accumulation layer) is under continuous compression, it is reasonable to assume that the carrier diffusive currents will decrease to a lower limit (the material is fully densified and the carrier-to-atom scattering becomes severe), which can be related to a lower limit value for  $\beta$  as denoted by  $\beta_a$ . If there is no mechanical strain in the channel, i.e.,  $\varepsilon = 0$ , the beta value should be  $\beta_b$ . Therefore, the function B should satisfy:  $B(\varepsilon_{max}) = \beta_a$  and  $B(0) = \beta_b$ . A function that satisfies these two equalities can be represented by Equation (3.131),

$$B(\varepsilon) = \beta_b - (\beta_b - \beta_a) \frac{e^{h\varepsilon} - 1}{e^{h\varepsilon_{max}} - 1} \quad (3.131)$$

where  $h$  is a fitted parameter that is determined experimentally,  $\varepsilon_{max}$  is the strain due to maximum compressive stress,  $\beta_a$  is the lower limit  $\beta$  value when the bulk semiconductor is fully

compressed,  $\beta_b$  is the  $\beta$  value when there is no deformation in the semiconductor. The plot for Equation (3.131) is presented in Figure 3.7. It can be observed that  $\beta$  value will slip from  $\beta_a$  to  $\beta_b$  as the mechanical strain decreases from  $\varepsilon_{max}$  to 0. In the extension region, it exhibits a similar dependence relationship of  $\beta$  on tensile strain  $\varepsilon$ . It is also discovered that the shape of the dependence curve can be modified by varying  $h$ , which is determined by experimental data.

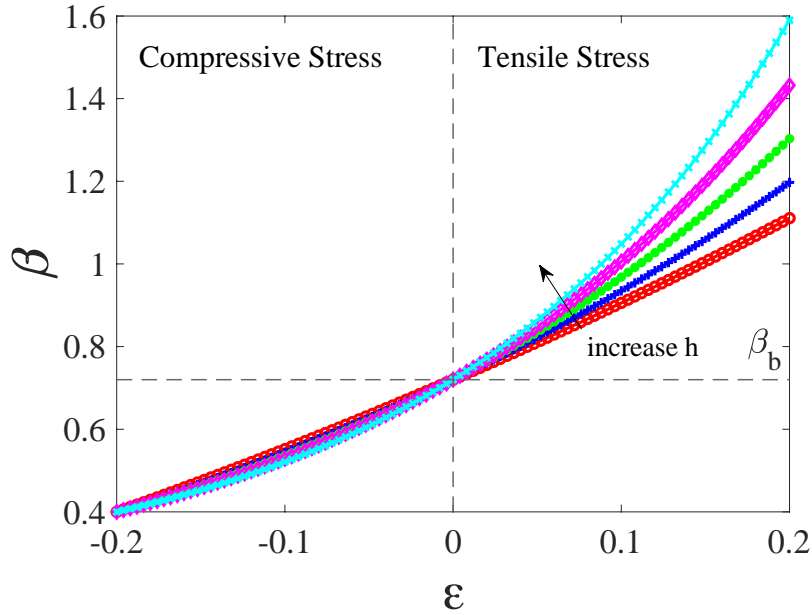


Figure 3.7 An illustration of strain-dependent  $\beta$  value under different  $h$  values, the negative  $\varepsilon$  indicates that the channel is under compression, the positive  $\varepsilon$  means that the channel is under extension,  $\varepsilon_{max} = -0.2$ ,  $\beta_a = 0.4$  and  $\beta_b = 0.72$  in this example.

### 3.4 Summary

In chapter three, the mass-spring-damper model was proposed in section 3.1 to characterize the mechanical strain and stress field in a ZnO TFT. The strain effects on the field-effect mobility and the threshold voltage of the TFT were analyzed, and the post-stress transconductance can be simulated by superimposing the strain-induced shifts of the field-effect mobility and the threshold voltage. For the modeling of OFETs, however, the influence of the multiple trap states on the band structure of OSCs cannot be ignored. In view of this, the generalized solid-state model was developed for OFETs to account for the considerable amount of trap states in OSCs. It was found that the generalized solid-state model cannot only model the

transconductance of OFETs but is also applicable for TFTs and MOSFETs made from ISCs if the parameter  $\gamma$  is set to one. In the case of  $\gamma = 1$ , the generalized solid state model automatically degenerates into the MOSFET model derived from the conventional MOSFET theory. In addition to the generalized solid-state model, the electromechanical coupling relationship was proposed in section 3.2 for the OFET to characterize its post-bent transconductance. The OFETs' electromechanical coupling relationship takes into consideration the influence of different scattering mechanisms on the mobility of OSCs, and it also quantifies the strain effects on the effective mobility and the threshold voltage. In section 3.3, the Fr-DD model was developed to simulate the transient and steady-state dynamics of any type of OSC devices, including the OFETs. Two algorithms were developed to solve for numerical solutions to the Fr-DD model. Rigorous proofs of the convergence and consistency of the algorithms were also presented. Furthermore, as the only freely adjustable model parameter, the order of the fractional gradient operator,  $\beta$ , is directly related to the mechanical strain in the electromechanical coupling relationship developed for the Fr-DD model.

## CHAPTER 4. RESULTS AND DISCUSSION

This chapter presented the simulations, experimental validations and discussions for the electromechanical characterization of OFETs based on the research methodologies developed in chapter three. Sections 4.1, 4.2 and 4.3 of chapter four were revised based on the author's published papers (Y. Yang et al., 2020, 2021a, 2021b).

### 4.1 Study of Strained TFT Based on Mass-Spring-Damper Model

The mechanical properties, including the displacement field, strain field, stress field within the domain of a two-dimensional ZnO TFT were simulated by the finite element analysis (FEA) model and the mass-spring-damper (MSD) model, respectively. A comparison study of the MSD and FEA models in terms of their computational performance (model convergence speed, memory usage) was conducted. A discussion of the reasonableness of the boundary conditions set in the simulation experiment was highlighted. The post-stress transconductance and output characteristics of the ZnO TFT were also presented.

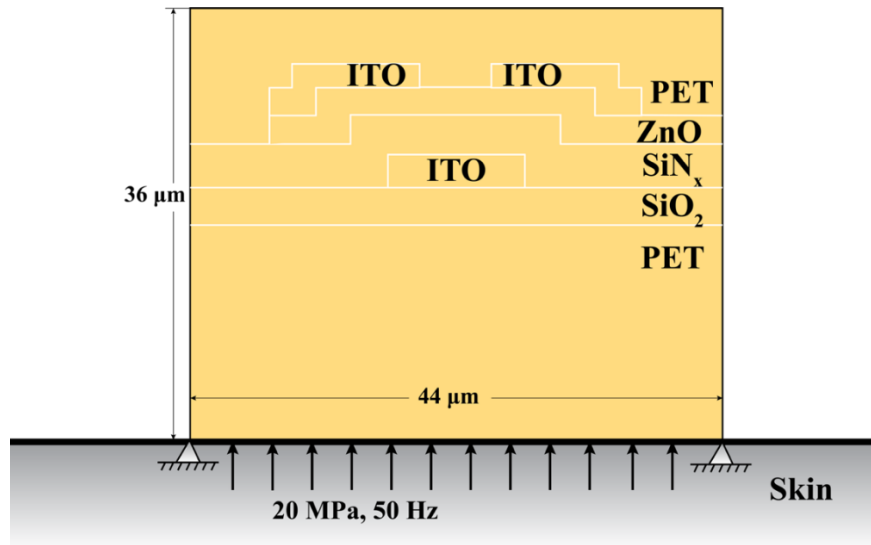


Figure 4.1 Schematics of the structure and material types for an encapsulated TFT, the active (semiconductor) layer is ZnO (Y. Yang et al., 2020).

#### 4.1.1 Simulation Setup

The structure and materials of the 2D inverted staggered ZnO TFT are shown in Figure 4.1. Three terminal electrodes (gate, source, drain) are made from Indium-Tin-Oxide (ITO), the active layer is formed by ZnO, the dielectric is SiO<sub>2</sub>, and the top and bottom encapsulating layers are polyethylene (PET). The material properties including the elastic modulus and the density of different material layers are tabulated in Table 4.1. The longitudinal dimension is set to be 44  $\mu\text{m}$  and the total thickness is required to be 36  $\mu\text{m}$ . The thickness of different material layers is listed in the last column of Table 4.1. The ZnO channel length (the longitudinal distance between two top ITO electrodes) is 18  $\mu\text{m}$ .

Table 4.1. Material properties and layer thickness for different material layers (Y. Yang et al., 2020).

Material	$E$ (GPa)	Density ( $\text{g}/\text{cm}^3$ )	Layer Thickness ( $\mu\text{m}$ )
ITO	112.0	7.1	2.0
ZnO	137.0	5.6	2.0
SiN <sub>x</sub>	250.0	3.1	3.0
SiO <sub>2</sub>	70.0	2.2	3.0
PET	5.0	1.4	18.0(bottom)\12.0(top)

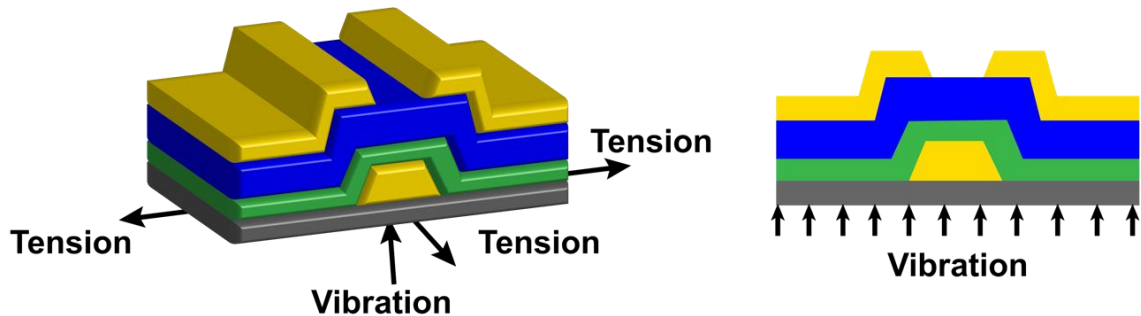


Figure 4.2 The inverted staggered TFT under two types of external loadings, surface tension and normal vibration can be considered as two major sources of boundary excitation when the TFT is attached to the surface of human or animal skin (the top and bottom encapsulating layers are not shown) (Y. Yang et al., 2020).

In this study, it is assumed that the inverted staggered ZnO TFT is conformally attached to the human or animal skin. As shown in Figure 4.2, two different contact stresses are present when the encapsulating layer is in contact with the skin surface: a tangential tension along the contact surface (caused by the sliding of the bottom encapsulating layer against the epidermis) and a normal vibrational stress (or hydrostatic pressure as it is called) perpendicular to the skin surface. If the thickness of the substrate is more than ten microns, the adhesions and bonding forces at the skin-substrate interface is infinitesimal (Nawrocki et al., 2018), and, it implies that the shear tensile force (tensions) at the skin-substrate interface can be neglected. Therefore, for the two different types of boundary excitations shown in Figure 4.2, only the normal vibrational stress will be considered in the simulation study. To further validate the reasonableness of the choice of the boundary excitations, the forearm skin of patients is described by a three-stage cascaded model (Khatyr et al., 2004), in which the strain-stress relation on the skin surface is given by Equation (4.1).

$$\sigma = \frac{\varepsilon}{\frac{1}{E_e} + \frac{1 - \exp(-t/\tau)}{E_{ve}} + A[1 - \sum_{i=1}^5 a_i \exp(-t/b_i)]} \quad (4.1)$$

The channel of TFT is assumed to be aligned along the longitudinal direction of the patient's arm. The average Young's modulus on the skin surface was reported as  $E_1 = 0.657$  MPa (Khatyr et al., 2004).  $E_1$  can be treated as the initial elastic stage Young's modulus of the skin in Khatyr's model, i.e.,  $E_e \approx E_1 = 0.657$  MPa. Then, it is inferred from Equation (4.1) that the magnitude of the tensile stress on the surface can be bounded by Equation (4.2), where  $E_{eff}$  is the effective elastic modulus of the forearm skin along the longitudinal direction, and  $E_{eff}$  is smaller than  $E_e$ ,  $E_{ve}$  and  $1/A$ .

$$\sigma = E_{eff} \cdot \varepsilon \leq E_e \cdot \varepsilon \quad (4.2)$$

Thus, taking the elastic modulus suggested by Khatyr et al. (2004), it is found that the tensile stress on the forearm skin surface is  $\sigma \leq E_e \cdot \varepsilon \approx 0.657 \times 0.6 = 0.4$  MPa. To compare the influence of the two types of boundary conditions on the TFT's outputs, the contour plots of the longitudinal stress in the TFT are simulated via COMSOL. As shown in Figure 4.3, the channel stress induced by the boundary tensile stress is way less than that induced by the boundary vibrational excitation. In view of this, it can be assumed that the TFT in contact with the human or animal skin is impacted by the normal vibrational excitations only. This observation is in agreement with what is claimed in the beginning of this section.



As shown in Figure 4.1, the TFT-skin contact model requires that the bottom layer of the inverted staggered TFT is attached to the skin surface with two fixed endpoints. A continuously sinusoidally distributed vibrational force (i.e., skin surface vibrations) with intensity of 20 MPa and frequency of 50 Hz is applied to the skin-substrate interface. 20 MPa and 50 Hz in the TFT-skin contact model is selected by referring to values reported by Kandel *et al.* (2012) and Pawlaczyk *et al.* (2013), in which the child skin elastic modulus is estimated around 70 MPa and the adult skin is about 60 MPa. Besides, Pawlaczyk *et al.* (2013) claimed that the new-borns' before-bursting ultimate skin deformation was 75% and the elderly's is 60%. Following Hooke's law, the ultimate intensity of normal pressure (stress) is approximately 52.5 MPa for newborns and 36 MPa for elderly. Because 20 MPa is less than 36 MPa, the normal vibrational excitation can take 20 MPa as an intermediate intensity for the case of simulation studies with acceptable accuracy.

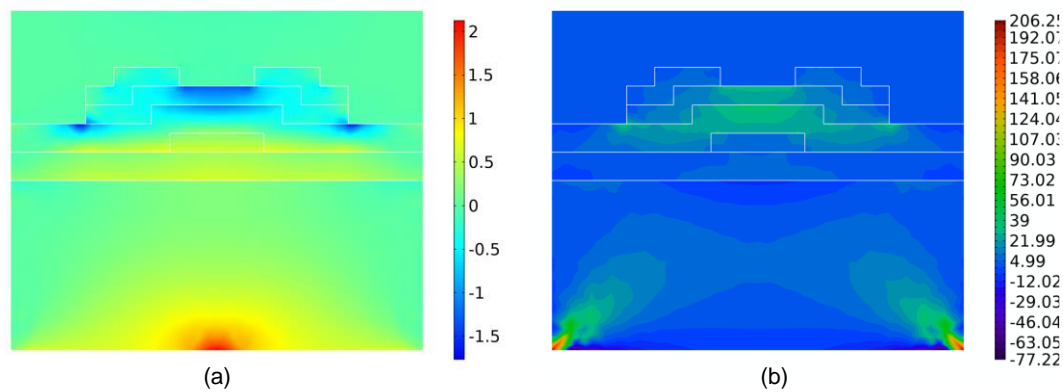


Figure 4.3 (a) Stress distribution in the TFT under symmetric tensile stress at the skin-substrate interface (in MPa); (b) Stress distributions in the TFT with vibrational excitations at the skin-substrate interface (in MPa) (Y. Yang et al., 2020).

In addition, the sinusoidal vibration with its frequency being 50 Hz is assumed in the simulation since the normal stress at the skin-substrate interface will not be a constant value in real scenarios. It is guaranteed in the sinusoidal vibrations that the intensity of interfacial normal stress can be decomposed into a continuous spectrum ranging from 0 to 20 MPa. In the real cases, 20 MPa may not be the exact stress intensity value at the skin-substrate interface, however, 20 MPa can be considered as an intermediate intensity of the normal vibrations at the interface when the strain happens to be 60%. Since the maximum elastic modulus of the skin was

reported to be less than 100 MPa, the normal stress should be smaller than 60 MPa, which is an upper bound but not the least upper bound of the normal vibrational intensity at the skin-substrate interface. In the following sections, the simulation of the MSD model for a ZnO TFT is presented and the strain induced shifts on TFT's transconductance characteristics are discussed.

The mass, stiffness and damping coefficients for cellular units of the MSD model are determined by the constitutive equation of the material. In the 2D MSD model, these parameters can be evaluated as follows:  $m_{j,k} = \rho V / N_c$ , where  $\rho$  is the density of materials,  $V$  is the volume of the layer, and  $N_c$  is the cellular units' total number in the layer. Spring stiffness  $k_{j,k}$  has four direction-dependent components. The dimensional analysis proves that the values of the stiffness components are proportional to elastic modulus of the layer. The MSD model allows the spring stiffness to coincide in magnitude with the layer's elastic modulus. The damping coefficient  $c_{j,k}$  also has four components, which can be determined by Equations (3.24), (3.25) and (3.26). Let  $M$  and  $N$  be the size of cellular units in the row and column directions, respectively. For example, the MSD parameters for the PET layer with different MSD sizes are obtained and recorded in Table 4.2. The units for  $m_{j,k}$  are in  $10^{-9}$  kg/s<sup>2</sup>, the units for four components of  $k_{j,k}$  are in  $10^{-3}$  kg/s, and the units for four components of  $c_{j,k}$  are in  $10^{-3}$  kg/s.

Table 4.2. The MSD parameters of the PET layer under different MSD sizes (assume damping ratio  $\zeta = 0.005$ ) (Y. Yang et al., 2020).

$M \times N$	$m_{j,k}$	$k_{j,k,1}, k_{j,k,3}$	$k_{j,k,2}, k_{j,k,4}$	$c_{j,k,1}$	$c_{j,k,3}$	$c_{j,k,2}, c_{j,k,4}$
$44 \times 36$	1.4	5	2.5	4.58	4.58	2.29
$88 \times 72$	0.35	5	2.5	2.29	2.29	1.15
$132 \times 108$	0.156	5	2.5	1.53	1.53	0.76
$176 \times 144$	0.0875	5	2.5	1.15	1.15	0.57
$220 \times 180$	0.056	5	2.5	0.92	0.92	0.46
$264 \times 216$	0.0389	5	2.5	0.76	0.76	0.38
$308 \times 252$	0.0286	5	2.5	0.65	0.65	0.33
$352 \times 288$	0.0219	5	2.5	0.57	0.57	0.29
$396 \times 324$	0.0173	5	2.5	0.51	0.51	0.25
$440 \times 360$	0.014	5	2.5	0.46	0.46	0.23
$484 \times 396$	0.012	5	2.5	0.42	0.42	0.21
$528 \times 432$	0.010	5	2.5	0.38	0.38	0.19
$572 \times 468$	0.008	5	2.5	0.35	0.35	0.18
$616 \times 504$	0.007	5	2.5	0.33	0.33	0.16

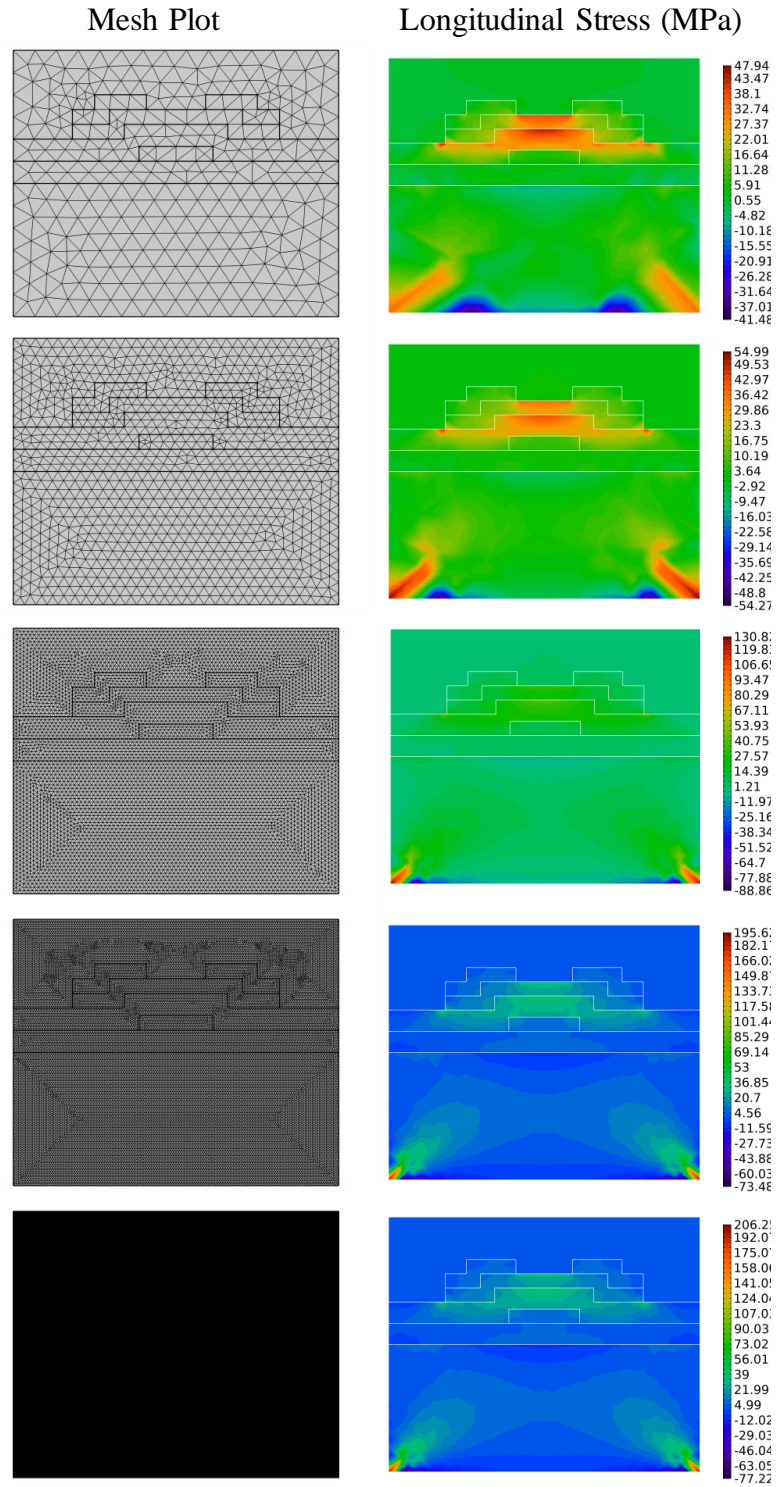


Figure 4.4 The mesh plots (left) generated by COMSOL and its corresponding stress distributions (right) in the longitudinal direction (Y. Yang et al., 2020).

#### 4.1.2 Comparison of FEA and MSD Models

In the simulation study, COMSOL was utilized to generate mesh of the FEA model, the mesh size can be tuned in the software. To address the convergence issue, a mesh refinement study was conducted. Five mesh groups and their associated simulated longitudinal stress were shown in Figure 4.4. The numeric values of the mesh sizes and the FEA simulation results solved by an 8-core Intel Core i9 CPU were presented in Table 4.3. When the mesh size decreases to smaller than  $0.295\ \mu\text{m}$ , the FEA model converges. As displayed in Table 4.3, the average channel stress in the longitudinal direction is around 20.35 MPa. In addition to the stress, the convergent total displacement field was simulated via FEA model, and the contour plot of the convergent total displacement was shown in Figure 4.5.

Table 4.3. Mesh sizes and simulation results of the FEA model under five groups of meshes (Y. Yang et al., 2020).

Mesh Size ( $\mu\text{m}$ )	Average Stress (MPa)	Simulation Time (s)
2.950	28.63	10
1.540	25.57	14
0.572	23.16	135
0.295	20.38	564
0.088	20.33	6035

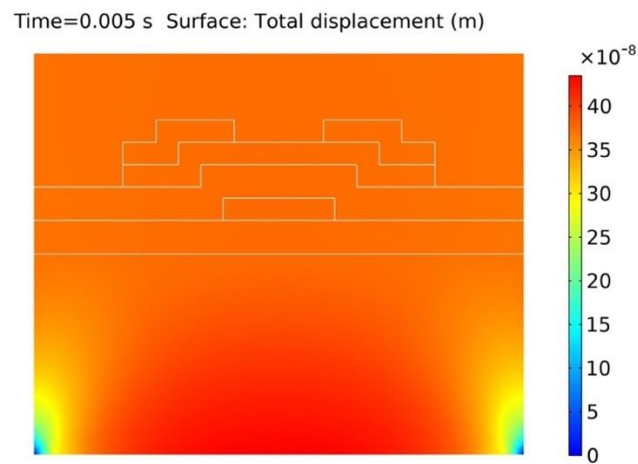


Figure 4.5 The total displacement of the ZnO TFT from FEA model (Y. Yang et al., 2020).

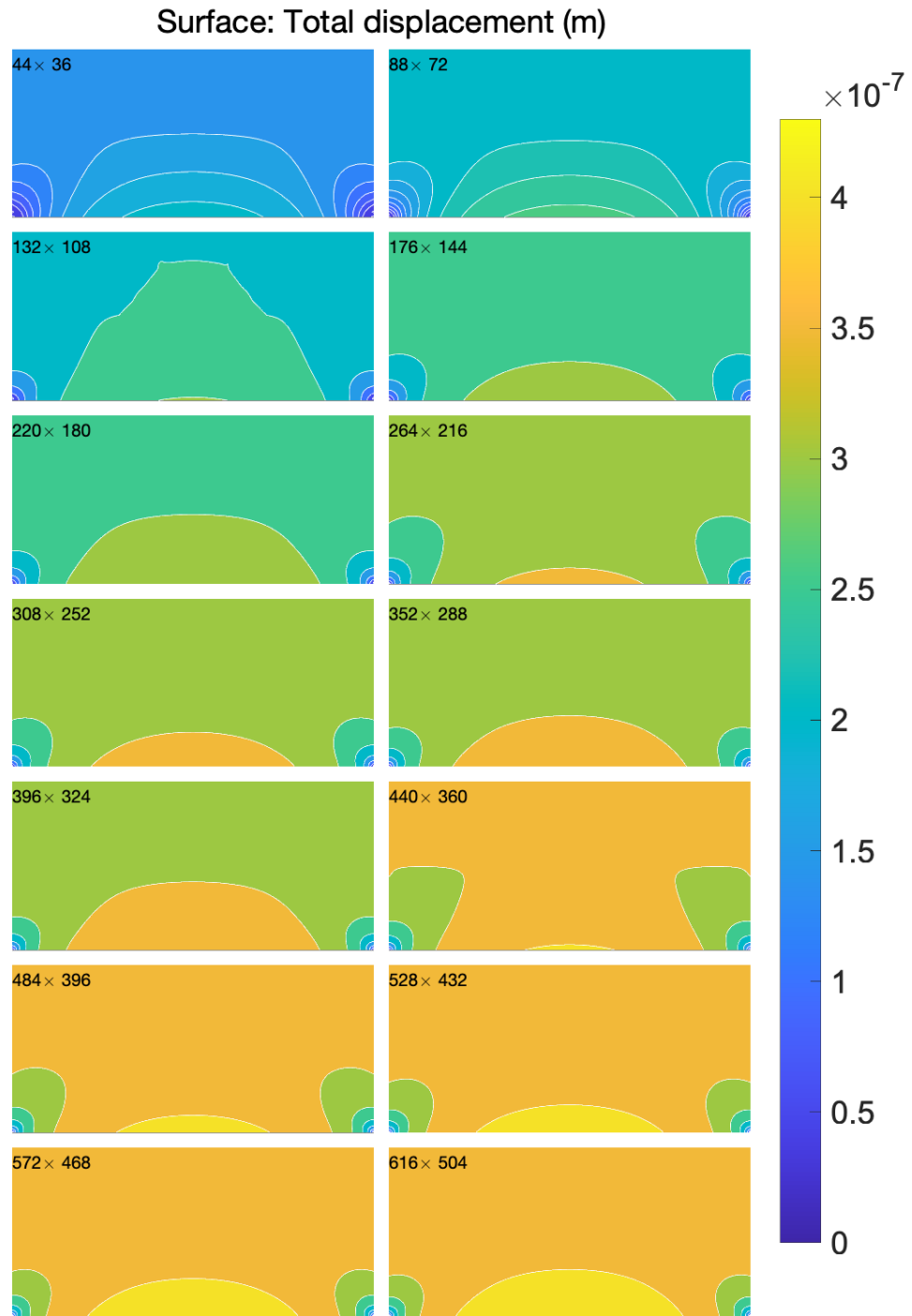


Figure 4.6 The total displacement fields simulated via 14 MSD models of different sizes ranging from  $44 \times 36$  to  $616 \times 504$  (Y. Yang et al., 2020).

Table 4.2 gives the model parameters for 14 sets of MSD models of different sizes, and the size of cellular units in the MSD model is denoted by  $M \times N$ . The total displacement fields simulated through 14 sets of MSD models of different sizes are shown in Figure 4.6.

If the size of MSD model is increased by several times over, the displacement field obtained by the MSD model with finer cellular units becomes more and more like the total displacement field obtained from the FEA model. Compared to the FEA model, the MSD model has more succinct formulation because the MSD dynamics can be originally collated into matrix equations. Since the coefficient matrices in the matrix representation of the MSD model are all sparse, it means that the MSD model can save a lot of computer memory compared to the FEA model. Based on this study, it is found that the FEA model needs over 10 GB of memory in general during its calculations to drive the solution converge. Nevertheless, for an MSD model at a size where convergent results can be obtained, for example, the  $616 \times 504$  MSD model, less than 4 GB of computer memory is needed to generate a comparable result to the FEA model.

In addition, the MSD model can significantly reduce the computational complexity as long as a suitable numerical algorithm is chosen. Farmago *et al.* (2011) stated that the computational complexity of the FEA model is  $\sim \mathcal{O}(NW^2)$ , where  $W$  is the bandwidth of the banded stiffness matrix and  $N$  is the grid numbers,  $N \sim 1/(\text{mesh size})^2$ . Indeed, the pattern of variation of the simulation time of the FEA model with the number of meshes recorded in Table 4.3 does match this theoretical time complexity. For the MSD model, efficient iterative algorithms, such as Gauss-Seidel, SOR, GMRES can be applied to invert the sparse matrices in the MSD model. Through simulation experiments, it can be found that the MSD model can take less than 2 minutes to get a convergent result. In addition to improvements in time complexity and space complexity, the MSD model can also provide analytic expressions to approximate boundary conditions and complex interface physical relationships, as well as to achieve the model reduction of the high-order dynamics, which is beneficial for the estimation of mechanical strains and fault detection in engineering applications.

#### 4.1.3 Strain-Induced Shifts of Mobility and Threshold Voltage

Figure 4.7 presents the relationship curves that exhibit the linear dependence of the average channel stress on the total displacement. The stress is positive when the channel is under tension and the stress is negative when the channel is under compression. Within a small

displacement ( $\sim 10^{-6}\text{m}$ ), the linear relationship between stress and displacement is considered to arise from stems from Equation (3.5).

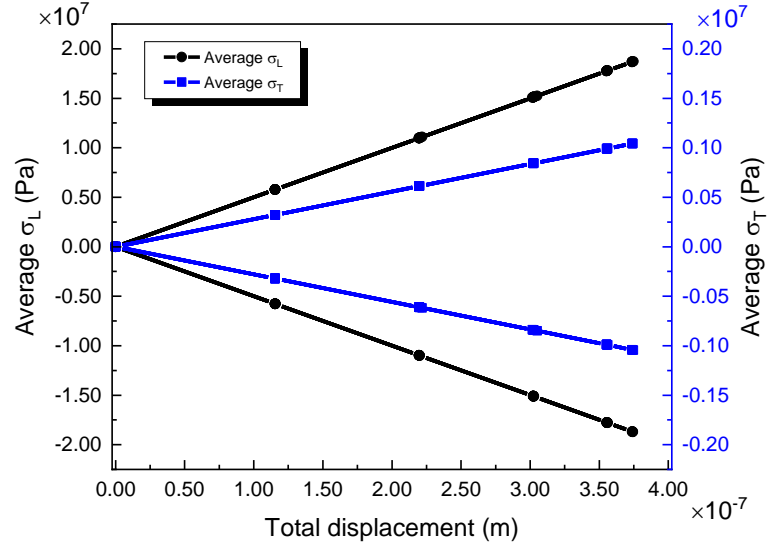


Figure 4.7 The linear relationship between stress and displacement for ZnO, the stress is positive (negative) when the channel is under tension (compression) (Y. Yang et al., 2020).

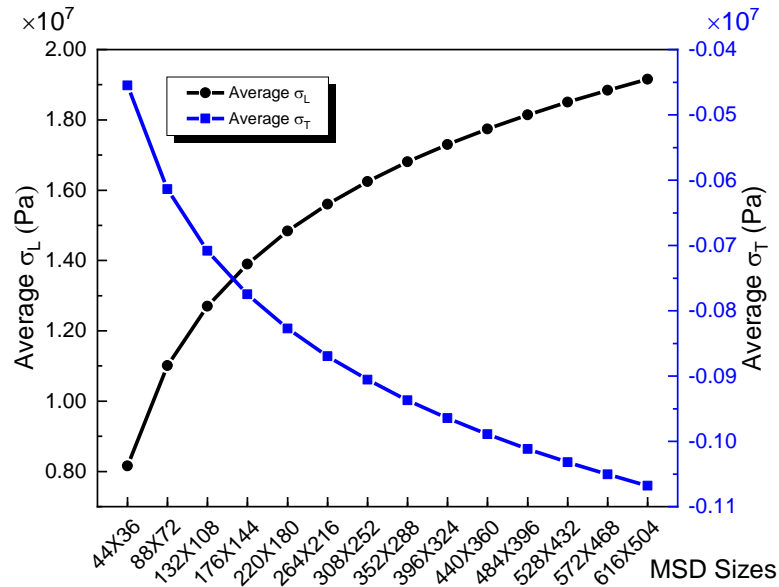


Figure 4.8 The average longitudinal stress (y axis to the left) and average transversal stress (y axis to the right) obtained by MSD models with different sizes (Y. Yang et al., 2020).

Given the linear relationship between stress and displacement in the ZnO channel, it is possible to obtain the average channel stress under the different MSD sizes. Figure 4.8 demonstrates the convergence of the average longitudinal stress and the average transversal stress with the size of MSD model. This convergence trend further illustrates the validity of the MSD model for stress/strain characterizations. Figure 4.9 gives the relative change of the mobility and the absolute change of the threshold voltage over a half period of the boundary excitation. It can be found that the relative change of  $\mu_{eff}$  is less than 0.03% and the absolute change of  $V_{th}$  is less than  $1.5 \times 10^{-4}$  V, which are very small numbers that can be neglected. Therefore, the ignorable strain-induced shifts of the mobility and the threshold voltage implies that the strain effects on the overall characteristics of the ZnO TFT may also be trivial.

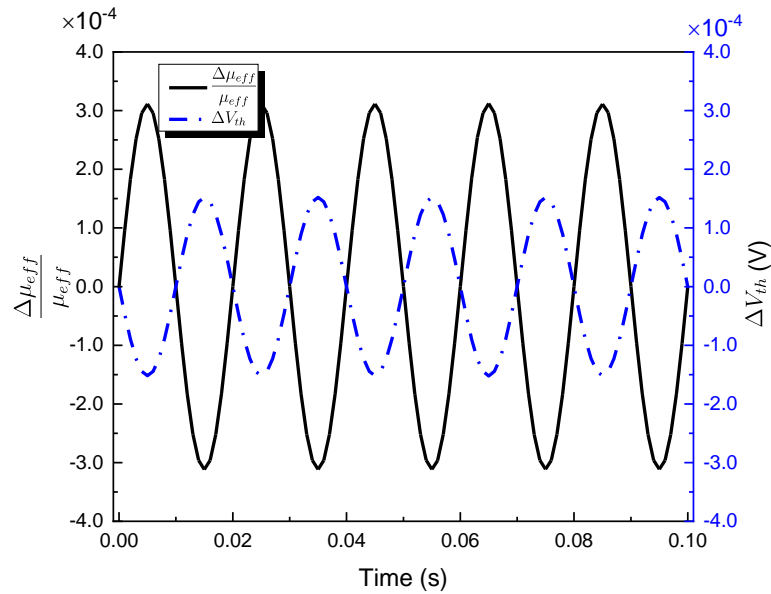


Figure 4.9 The strain-induced shifts on the carrier mobility (y axis to the left) and the threshold voltage (y axis to the right) in an inverted staggered ZnO TFT when it is under a sinusoidal vibrational boundary excitation (Y. Yang et al., 2020).

Table 4.4. The strain-free parameters of ZnO (Siddiqui, 2012).

	$\mu_{eff}$	$V_{th}$	$\epsilon_0$	$\epsilon_r$	$t_{ox}$	$C_{ox}$
ZnO	110	2	$8.8542 \times 10^{-12}$	3.3378	0.2	$1.478 \times 10^{-8}$



#### 4.1.4 Strain Effects on ZnO-TFT Characteristics

Since the ZnO is an n-type semiconductor and the TFT is operating in enhancement mode, Equations (3.37) and (3.38) can be used to obtain the transconductance and output characteristic curves of the transistor. The strain-free parameters of the ZnO-TFT are specified in Table 4.4, where  $\mu_{eff}$  is the non-strain carrier effective mobility in  $\text{cm}^2/(\text{Vs})$ ,  $V_{th}$  is the zero-strain threshold voltage in Volt. The vacuum permittivity  $\epsilon_0$  is in  $\text{m}^{-3}\text{s}^4\text{A}^2/\text{kg}$ ,  $\epsilon_r$  is the relative permittivity of ITO,  $t_{ox}$  is the thickness of the oxidized ZnO layer in  $\mu\text{m}$ , and  $C_{ox} = \epsilon_0\epsilon_r/t_{ox}$  is the per unit area gate oxide capacitance in  $\text{F}/\text{cm}^2$ . Moreover, it is assumed that the gate oxide layer and the ZnO layer have the same thickness in the simulation study.

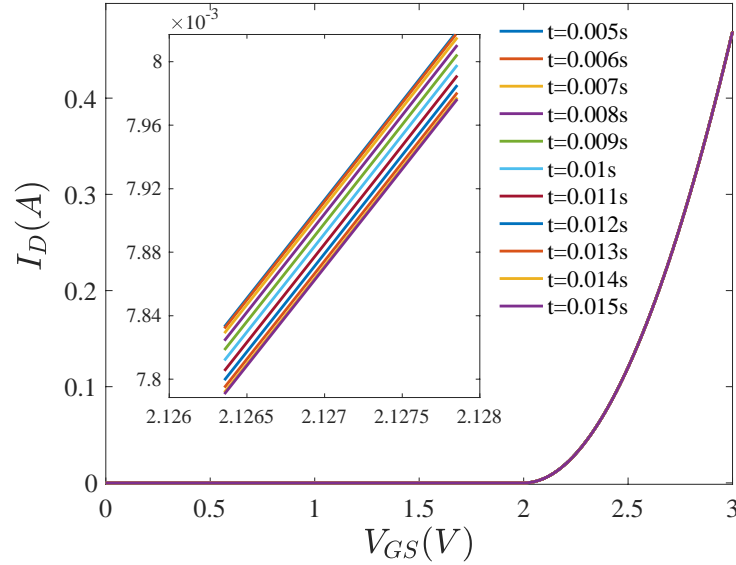


Figure 4.10 The transconductance curves of the ZnO-TFT under a sinusoidal boundary excitation, the transconductance is evaluated at  $t=0.005\sim 0.015\text{s}$ , which is half a period of the boundary excitation (Y. Yang et al., 2020).

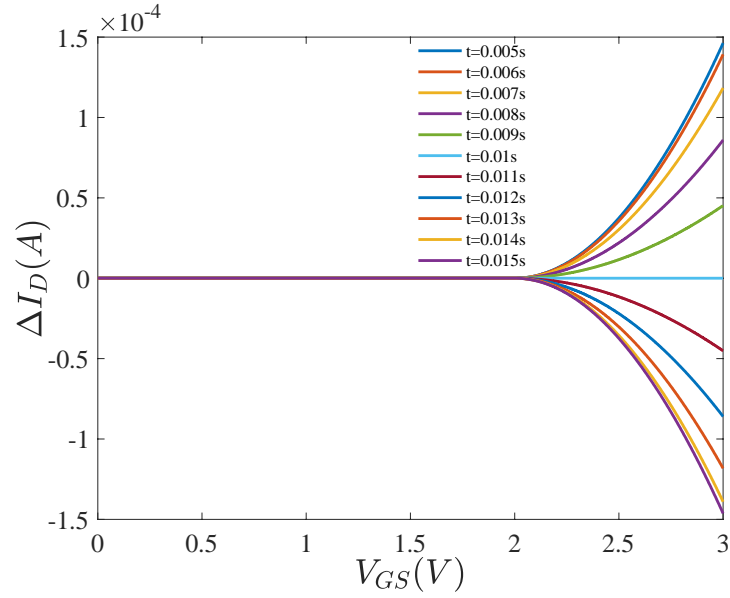


Figure 4.11 The curves of drain current shifts with gate-source voltage at different moments within a boundary excitation cycle, the drain current shifts are evaluated at  $t=0.005\sim 0.015\text{s}$  (Y. Yang et al., 2020).

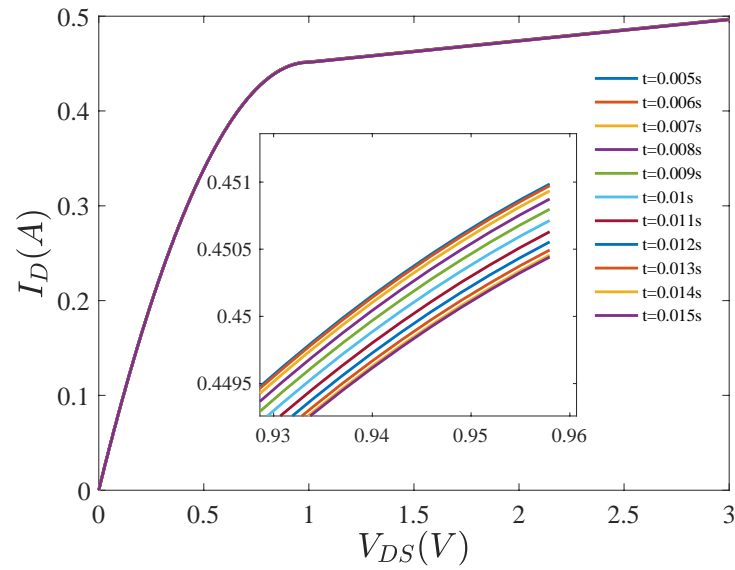


Figure 4.12 The output curves of the ZnO-TFT under a sinusoidal boundary excitation, the transconductance is evaluated at  $t=0.005\sim 0.015\text{s}$  (Y. Yang et al., 2020).

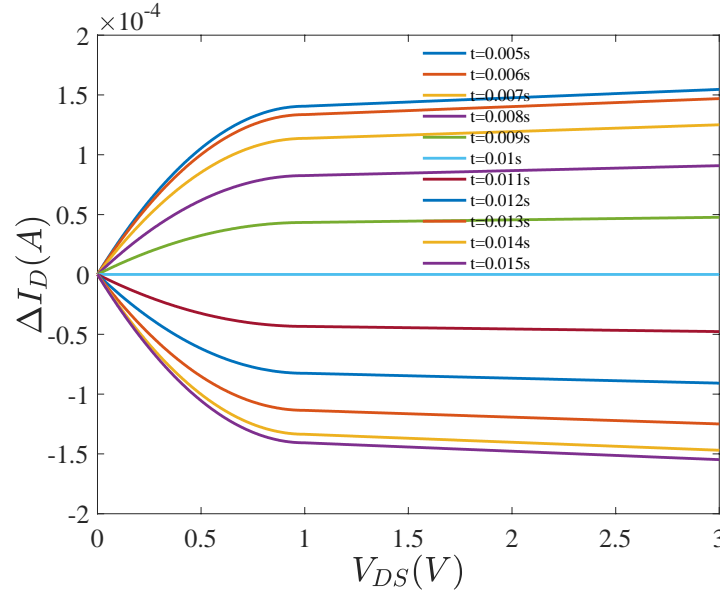


Figure 4.13 The curves of drain current shifts with drain-source voltage at different moments within a boundary excitation cycle, the drain current shifts are evaluated at  $t=0.005\sim0.015\text{s}$  (Y. Yang et al., 2020).

Considering the strain-induced shifts of the field-effect mobility and the threshold voltage, the transconductance and output curves of the ZnO-TFT can be obtained and plotted in Figure 4.10 and Figure 4.12, respectively. Figure 4.10 and Figure 4.12 depict the shapes of the transconductance and output characteristic curves over one cycle of the sinusoidal boundary excitation. To better observe the tiny changes in the characteristic curves, the curves of the drain current variations with respect to the gate-source voltage and the drain-source voltage at different moments in a boundary disturbance cycle are presented in Figure 4.11 and Figure 4.13, respectively. As shown in the figures, the drain current  $I_D$  will slightly deviate from the stress-free scenarios for less than 0.03%.

The small shifts of the TFT's transconductance and output characteristics can be ascribed to two reasons. First of all, the two endpoints of the skin-substrate interface are fixed so that the substrate will be prevented from slipping against the skin in the longitudinal and lateral directions. On the other hand, if the substrate (i.e., the PET encapsulating layer) is much thicker than the other material layers, the surface adhesions due to the bonding between the skin and the substrate is unimportant, thus allowing surface tensile stress to be ignored by the MSD model. Per the analysis, it is revealed that a secure way to maintain the electrical performance of TFTs

under mechanical deformation is to make the encapsulating layer much thicker. Adding the thickness of the encapsulating layer cannot only increase the cushioning against normal vibrations on the boundary, but also help relocate the neutral stress plane to the TFT's active layer so that the strain damage to the active layer can be reduced. This finding is extremely helpful for designing and making smart selections on the layout of flexible thin film sensors.

Original analysis uses 20 MPa as an intermediate value of the skin-substrate interfacial vibrational intensity. If an upper-bound vibrational intensity (e.g., 60 MPa) is assumed on the skin-TFT interface, the strain effects on the field-effect mobility and the threshold voltage should be reanalyzed to compare them with the results in the 20 MPa context. In the case of 60 MPa, the MSD simulations show that the relative change is 0.1% for  $\mu_{eff}$  and 0.024% for  $V_{th}$ . The transconductance and output curves are shifted only by less than 0.1%. Therefore, it can conclude that the electrical performance of the inverted staggered ZnO-TFT will not be severely impaired by the mechanical deformation due to contact with the skin.

#### 4.2 Study of Bendable OFETs Based on Generalized Solid-State Model

In this study, a novel generalized solid-state model was proposed for a DNTT-based (a p-type OSC) OFET. The field-effect mobility of the OFET is required to be enhanced in the low-field region and degraded in the high-field region due to the influence of trap states and different scattering mechanisms resulting in the saturation of carriers' drift velocity. The generalized current-voltage equations were derived for the first time to provide a unified description of the transconductance and output characteristics of inorganic and organic FETs. The bending induced shifts of the field-effect mobility and the threshold voltage follow a group of semiempirical equations by analogously utilizing the deformation potential theory developed for inorganic TFTs and MOSFETs. The model was validated by showing that it can agree very well with the measured data from a bendable DNTT OFET. This study is likely the first to investigate the physical modeling of a deformable OFET under bending. The models and approaches proposed in this study can facilitate the electrical characterization of OFETs and foster the EDA process of flexible thin-film electronics.

#### 4.2.1 Simulation Setup

Figure 3.5 depicts the fundamental components of a TCBG OFET. In the bending test, the encapsulated OFET is laminated onto a pre-stretched elastomer. Wrinkles at the interface of thin-but-hard OFET and thick-but-soft elastomer stack can be formed by relaxing the pre-stretched elastomer (Nawrocki, 2019), due to the conformal nature of the lamination related to the film thickness. More details about the bending tests and the OFET fabrication are presented in literatures (Nawrocki et al., 2016). A post-bent OFET can generate both the compressive and tensile stresses at the semiconductor-insulator interface. Less wrinkles will be formed in the thin film if the encapsulated OFET is much thinner than the elastomer layer, and according to the bending experiments, it implies that in the ideal case there will be only one bending arc in the thin film if the relative thickness of the OFET to the elastomer layer is very large. Because the encapsulated OFET has a total thickness of tens of nanometers, it is almost impossible to make only one bending arc in the thin film. Nevertheless, the number of wrinkles on the film can be reduced by increasing the thickness of the pre-stretched elastomer, and the estimated bending radius of the OFET is around 2  $\mu\text{m}$  by reading the SEM images. To experimentally validate the generalized solid-state model, a Silvaco Atlas based simulation is conducted to extract the model parameters. Silvaco Atlas is a software package that can solve the Poisson-Nernst-Planck (PNP) equations in a 2D mesh domain, in which the system boundary conditions can automatically be tackled by the software core (Silvaco International, 2016). The fitted model parameters and the basic properties of OSCs and dielectric materials are presented in Table 4.5.

Table 4.5. Fitted model parameters and basic material properties for the generalized solid-state model (Y. Yang et al., 2021a).

Symbol	Quantity	Values Specified in Simulation
$K_S$	DNTT's relative permittivity	3.0
$K_O$	Parylene's relative permittivity	3.9
$x_0$	Thickness of the insulator	64 nm = $6.4 \times 10^{-7}$ cm
$N_h$	Effective DoS at HOMO edges	$2 \times 10^{21}$ cm $^{-3}$
$L$	Length of channel	100 $\mu$ m
$W$	Width of channel	1000 $\mu$ m
$C_{OX}$	Dielectric capacitance per unit area	$5.3955 \times 10^{-8}$ F/cm $^2$
$\gamma$	Relative number of the trap states	Variable $\sim 1, 1.1, 1.2, 1.3$
$\Delta$	Activation energy of Poole-Frenkel mobility model	0.2 eV
$\beta$	Fitting parameter of PF model	$3.79 \times 10^{-2}$ eV $\cdot \sqrt{\text{cm}/V}$
$\gamma_{pf}$	Fitting parameter of PF model	$1 \times 10^{-5}$
$\mu_0$	Non-activated mobility of holes	0.5 cm $^2$ /(V $\cdot$ s)
$N1P$	Fitting parameter of Coulombic scattering model	$8.1 \times 10^{11}$
$N2P$	Fitting parameter of CSM	$4 \times 10^{13}$
$ALPHA_p$	Fitting parameter of CSM	3.4
$N_{TD}$	Edge intercept of TD trap states	$1 \times 10^{18} \sim 10^{23}$ cm $^{-3}$
$\gamma_{BHp}$	Dependent parameter	$4.05 \times 10^{-10}$ cm $^3$
$BETACT$	Fitting parameter of CT model	1
$v_{sat}$	Saturated velocity of CT model	640 cm/s
$y_a$	Nominal thickness of the accumulation layer	5 nm = $5 \times 10^{-7}$ cm
$N_{TD0}$	Edge intercept of ionized TD trap state concentration	$3.6 \times 10^{20}$ cm $^{-3}$
$d_s$	Substrate thickness	154 nm = $1.54 \times 10^{-5}$ cm
$d_f$	The active layer thickness	30 nm
$\chi$	Relative elastic modulus of active layer to substrate	15.36 GPa/2.8 GPa
$\eta$	Relative thickness of active layer to substrate	0.195
$\Pi(\theta, \varphi)$	Piezoresistive coefficient	$7.57 \times 10^{-9}$ Pa $^{-1}$
$\Xi_d$	Dilation deformation potentials at HOMO edges	210.5 eV
$\Xi_u$	Uniaxial deformation potentials at HOMO edges	330 eV
$I_{D0}$	Leakage current	$-4.139 \times 10^{-3}$ $\mu$ A ( Pre-bent ) $-5.24 \times 10^{-3}$ $\mu$ A (Post-bent)
$n$	Slope parameter	11.2/7.373 (Pre-/Post-bent)
$\alpha$	Fitting parameter	3.374/0.5551 (Pre-/Post-bent)

### 4.2.2 Surface Potentials

OFETs' analysis is completely different from MOSFETs. For instance, a p-channel MOSFET in enhancement mode will have an inversion layer formed at the dielectric-semiconductor interface if its gate electrode is connected to a negative voltage source. The current conduction between the drain and source electrodes is achieved by the transport of minority carriers (i.e., holes in p-channel/pnp MOSFET) through the inversion layer. For a p-channel OFET working in the enhancement mode, however, an accumulation layer will be formed at the dielectric-semiconductor interface under a negative applied bias  $V_{gs}$ , and the accumulation layer will allow the transport of majority carriers in p-channel OFET, i.e., holes to form current conduction between drain and source electrodes.

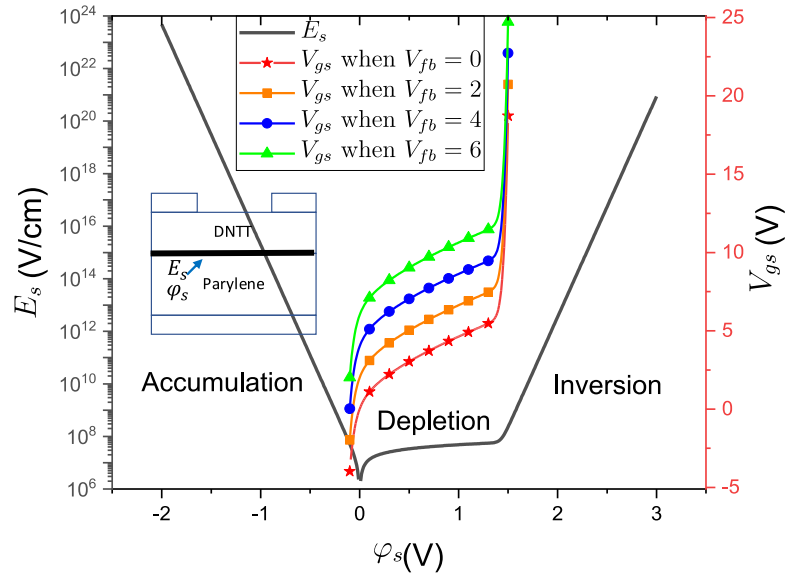


Figure 4.14 The surface electric field varies as a function of surface potential (y axis to the left), and the gate-source voltage varies as functions of surface potential when the flat-band voltage is fixed to different values (y axis to the right) (Y. Yang et al., 2021a).

Figure 4.14 demonstrates the relationships developed in Equations (3.50) and (3.52). As shown in Figure 4.14, a negative surface potential is required to form the accumulation layer in a p-channel OFET, and accordingly, when  $V_{fb} = 0$  it will result in a reversely biased gate-source voltage. In addition, it is also observed that the OFET may be operated in the depletion mode when the flat-band voltage is increased to a positive value, and this observation implies that the accumulation layer can be depleted and the OFET device can be turned off under a positive gate-

source voltage. In practical situations, the  $V_{gs}$  vs  $\varphi_s$  relationship may be slightly different from the plot of Equation (3.52). For instance, a nonideal OFET may shift its  $V_{gs}$ - $\varphi_s$  curves to the left of the ideal  $V_{gs}$ - $\varphi_s$  curves in Figure 4.14, and the nonideal OFET will be transitioned from accumulation to the depletion mode at a negative surface potential ( $\varphi_s < 0$ ) instead of zero. The OFETs' nonideality comes from the surface potentials' uneven distribution ( $\varphi_s$  varies along the channel direction), the nontrivial backside potentials and other neglected modeling errors. The simulation of this study will counterbalance the nonideality of OFETs by shifting the curves of  $\varphi_s$  uniformly to the left and utilizing gradual channel approximation to evaluate the varying  $\varphi_s$  along the channel direction.

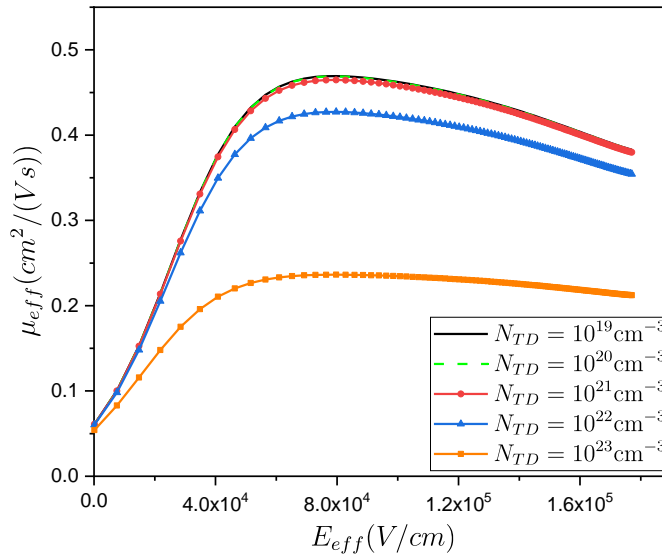


Figure 4.15 The overall effective (field-effect) mobility (after considering multiple scattering effects) of DNTT as a function of the effective electric field when the density of trap states is fixed to different values (Y. Yang et al., 2021a).

### 4.2.3 Overall Effective Mobility

The effective field-effect mobility of DNTT under different density of TD trap states is evaluated by Equation (3.57) and Figure 4.15 shows the simulated results. The first observation is that the overall hole mobility of DNTT is enhanced in the low-field region ( $E_{eff} < 4 \times 10^4$  V/cm). Because the high electric field intensity can accelerate the motion-impeding collisions among holes and semiconductor surface, the drift velocity of holes will be limited and finally becomes saturated. Since the hole mobility is proportional to the holes' drift velocity and



inversely proportional to the electrical field intensity, it can be predicted that the effective mobility of holes will decrease as the drift velocity becomes saturated and the electric field intensity increases. In Figure 4.15, the effective hole mobilities under different density of TD trap states are also compared. As displayed in Figure 4.15, it becomes evident for the TD trap states to take effects on the overall mobility of holes as the density of TD trap states  $N_{TD}$  goes beyond the effective DoS at the HOMO band edges, where  $N_h = 2 \times 10^{21} \text{cm}^{-3}$ . The decreasing of the effective mobility for increasing  $N_{TD}$  is a reasonable phenomenon because more trap states can intensify the scattering effects of ionized defects on mobile carriers.

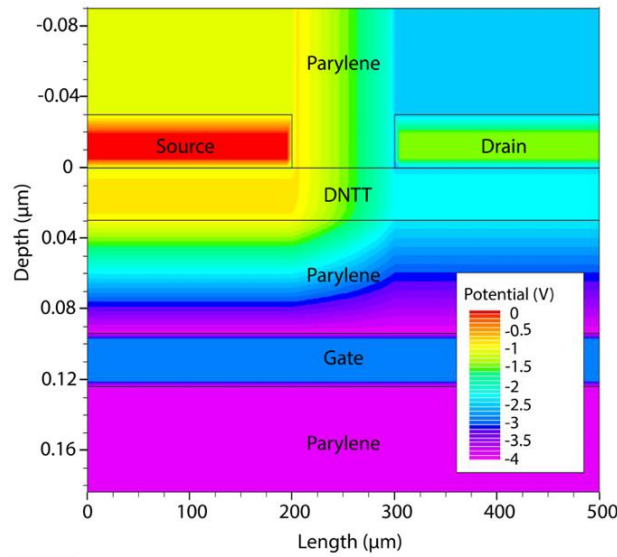


Figure 4.16 The contour plot of the electrostatic potentials when the OFET is working under applied bias  $V_{ds} = -1.5 \text{ V}$  and  $V_{gs} = -3 \text{ V}$  (Y. Yang et al., 2021a).

#### 4.2.4 Electrostatic Potentials, Current Flows and Hole Concentration

The simulated contour plots for the electrostatic potentials, the current flowlines and the hole concentration in a DNTT OFET with applied bias  $V_{ds} = -1.5 \text{ V}$  and  $V_{gs} = -3 \text{ V}$ , are shown in Figure 4.16, Figure 4.17 and Figure 4.18, respectively. Because the gradual channel approximation is applied to derive the generalized current-voltage equations, it can be observed in Figure 4.16 that the potential variations along the channel is more significant than its changes in the  $y$  direction. Since the channel thickness is much smaller than the channel length of the DNTT OFET, the parallel component of the electric field may be still much smaller than its

perpendicular component even if there is a substantial potential difference between the source and drain electrodes.

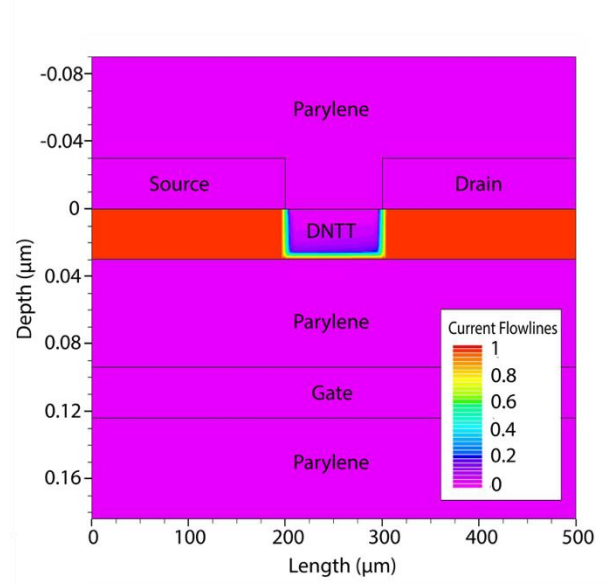


Figure 4.17 The contour plot of the current flowlines with the accumulation layer for carrier transport when the OFET is working under applied bias  $V_{ds} = -1.5$  V and  $V_{gs} = -3$  V (Y. Yang et al., 2021a).

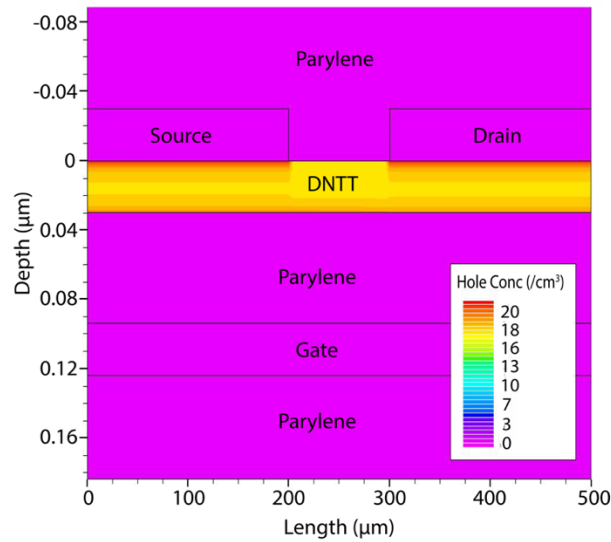


Figure 4.18 The contour plot of the hole concentration when the OFET is working under applied bias  $V_{ds} = -1.5$  V and  $V_{gs} = -3$  V (Y. Yang et al., 2021a).

As illustrated in Figure 3.5, an accumulation layer should be formed at the semiconductor-dielectric interface to provide a channel for charge carrier transport. Figure 4.17 displays the accumulation layer's simulated contours and implies that the accumulation layer's thickness in the DNTT OFET should be approximately 5 nm, which is similar to the reported values in several literatures (Gupta et al., 2009; Kaushik et al., 2016; Shim et al., 2010). The contours of the OFET's hole concentration in the steady state is depicted in Figure 4.18, which suggests that the recombination rate is substantially larger the generation rate of the holes.

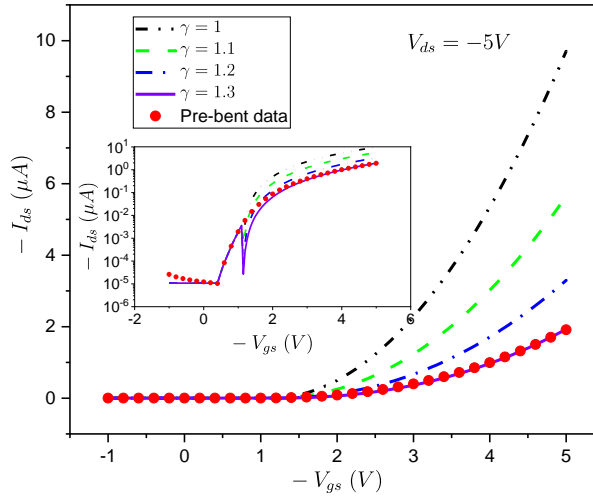


Figure 4.19 Drain current versus gate-source voltage (transconductance) characteristic curves under different  $\gamma$  values, the curve with  $\gamma = 1.3$  has the best agreement with the experimental data (Y. Yang et al., 2021a).

#### 4.2.5 Tuning of Model Parameters

The transconductance curves that plot the drain current against gate-source voltage under different  $\gamma$  values are shown in Figure 4.19. And the output curves that relate the drain current to the drain-source voltage under different  $\gamma$  values are given in Figure 4.20.. When the  $\gamma$  value is increased from 1.0 to 1.3, the DoS at the HOMO band edges is gradually emulated and exceeded by the density of trap states. The massive number of ionized trap centers will impede the hole transport and reduce the drain current flows in the channel. Because a great number of trap states (ionized defects) intensifies the defect-carrier collisions and reduces the drift velocity of mobile carriers, the drain current in the case of  $\gamma = 1.3$  becomes around 1/9 of the drain current in  $\gamma = 1$ . In addition, the pre-bent curve in the case of  $\gamma = 1.3$  also exhibits a better agreement with the

experimental measurements except for a very small neighborhood around the threshold voltage. This finding suggests that the generalized solid-state model with  $\gamma = 1.3$  can accurately account for the real density of trap states in the DNTT OFET. In practice, the OSC's density of trap states can be adjusted not only by  $\gamma$ , but also by  $N_{TD}$ .  $N_{TD}$  is the intercept density of trap states in the HOMO band edges. As mentioned in the carrier mobility modeling section,  $N_{TD}$  plays a significant role in regulating the magnitude of the carrier's overall mobility. The parameter  $\gamma$ , by another means, alters the OFET's transconductance characteristics by directly acting on the generalized current-voltage equations, and the actual value of  $\gamma$  needs to be determined by fitting the experimental data.

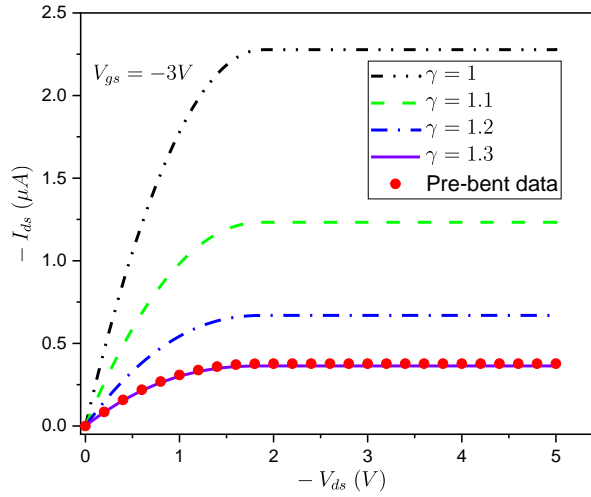


Figure 4.20 Drain current versus drain-source voltage (output) characteristic curves under different  $\gamma$  values, the curve with  $\gamma = 1.3$  has the best agreement with the experimental data (Y. Yang et al., 2021a).

#### 4.2.6 Comparison of Pre-bent and Post-bent OFET Characteristics

The comparison of the theoretically predicted (blue dashed lines and black solid) and the measured (green squares and red circles) transconductance characteristics are given in Figure 4.21, both of them include the pre-bent and post-bent characteristics of OFETs, with  $V_{ds}$  fixed to  $-5$  V. In the generalized solid-state model, the strain induced shifts of the threshold voltage and the carriers' field-effect mobility are taken care of by superimposing the results of Equations (3.68) and (3.69) to the parameters in Equations (3.62) and (3.65). It can be observed that the generalized solid-state model ( $\gamma = 1.3$ ) validated in the pre-bent case is also valid for the post-

bent case if the electromechanical coupling relationship takes the parameter values in Table 4.5. The generalized solid-state model for the pre-bent and post-bent cases are both established by assuming the density of ionized TD trap states  $N_{TD0} = 3.6 \times 10^{20} \text{ cm}^{-3}$ . The density of TD trap states  $N_{TD}$  is determined by  $N_{TD0}$  and  $\gamma$  according to Equation (3.48), and the DNTT's overall field-effect mobility is then regulated by  $N_{TD}$ . Nevertheless, the much better fitting performance of the generalized solid-state model at the high  $V_{gs}$  region, such as the linear and saturation regimes, should be noticed. The transconductance curves in the inset plot of Figure 4.21 shows that the generalized solid-state model cannot explain the transconductance in a small region between the subthreshold and the linear/saturation regimes. This is because when  $V_{gs}$  is small, the Fermi level is positioned closer to HOMO edges, leading to a further distance between LUMO edges and TD trap centers. This implies that at the low  $V_{gs}$  region two other types of trap states (i.e., GD, GA) will play more important roles than TD trap states. Therefore, the generalized solid-state model that only considers the TD trap states fails at the low  $V_{gs}$  region. However, because the OFET behaviors in the subthreshold regime is remedied by Equation (3.66), the generalized solid-state model (that involves the supplementary formula of the subthreshold regime) only loses its fitting accuracy within a small transitional  $V_{gs}$  region.

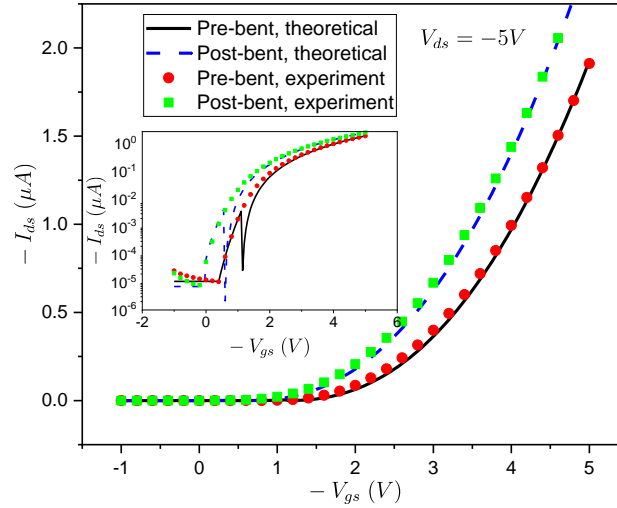


Figure 4.21 Comparison of the theoretically predicted ( $\gamma = 1.3$ ) and experimentally measured (symbols) drain current as a function of gate-source voltage (the transconductance curves) for fixed  $V_{ds} = -5 \text{ V}$ , both the pre-bent and post-bent cases are illustrated (Y. Yang et al., 2021a).

When  $V_{gs}$  is fixed to five different values, Figure 4.22 compares the theoretically predicted (solid black lines) and measured (colored symbols)  $I_{ds}$  versus  $V_{ds}$  output curves, for the case of a pre-bent OFET.

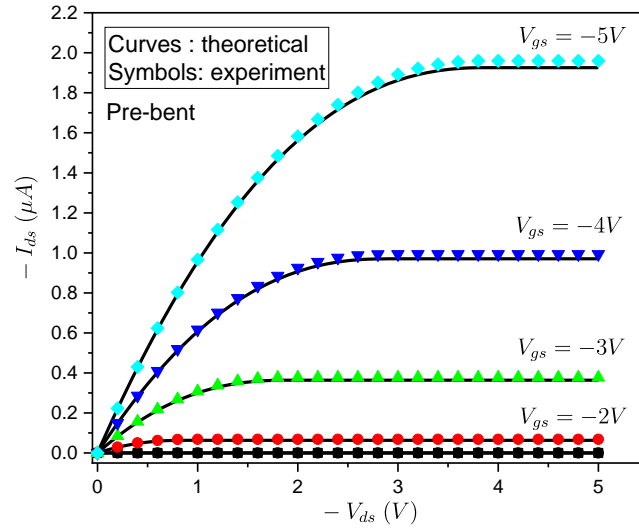


Figure 4.22 Comparison of the theoretically predicted ( $\gamma = 1.3$ ) and experimentally measured (symbols) drain current as a function of drain-source voltage (black lines) for fixed  $V_{gs} = 0, -1, -2, -3, -4, -5$  V, only the pre-bent case is illustrated (Y. Yang et al., 2021a).

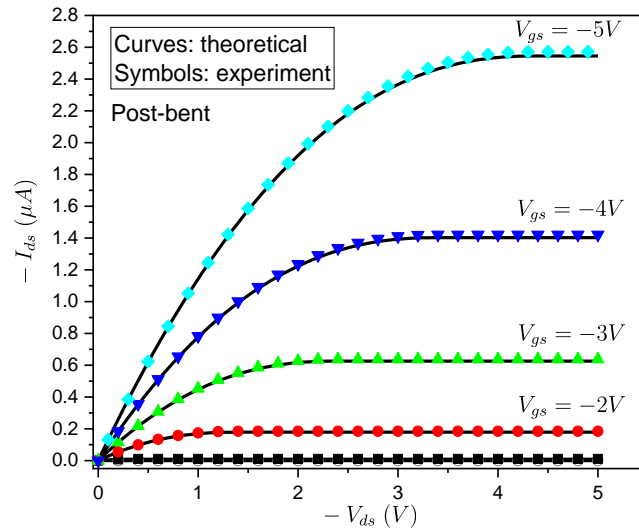


Figure 4.23 Comparison of the theoretically predicted ( $\gamma = 1.3$ ) and experimentally measured (symbols) drain current as a function of drain-source voltage (black lines) for fixed  $V_{gs} = 0, -1, -2, -3, -4, -5$  V, only the post-bent case is illustrated (Y. Yang et al., 2021a).

Similarly, the post-bent  $I_{ds}$  versus  $V_{ds}$  characteristics under different fixed  $V_{gs}$  is displayed in Figure 4.23. It can be seen that in both figures the theoretical predicted output curves ( $\gamma = 1.3$ ) can agree well with the experimental measurements. By comparing the pre-bent and the post-bent transconductance curves, it is found that the non-activated mobility  $\mu_{eff}$  can be enhanced from  $0.5 \text{ cm}^2/(\text{V} \cdot \text{s})$  in the pre-bent case to  $0.57 \text{ cm}^2/(\text{V} \cdot \text{s})$  in the post-bent case, with the average effective mobility changing from  $0.43 \text{ cm}^2/(\text{V} \cdot \text{s})$  to  $0.49 \text{ cm}^2/(\text{V} \cdot \text{s})$ . The post-bent threshold voltage  $V_{th} = -0.62 \text{ V}$ , however, is smaller than the pre-bent threshold voltage, which is  $-1.12 \text{ V}$ . Another important observation is that in the post-bent case  $I_{ds}$  is not zero any more for  $V_{gs} = -1 \text{ V}$ , because the threshold voltage shrinks to a value less than  $V_{gs}$  when the OFET is under bending.

#### 4.3 Study of Strained OSC Devices Based on Fractional Drift-Diffusion Model

Unlike the generalized solid-state model, which focuses on the drifting motion of carriers, the fractional drift-diffusion (Fr-DD) model considers both the drifting and the diffusive motion of carriers. The Fr-DD model is not only for OFETs, but can also be utilized to predict the transient and steady-state response of other electronic devices made from organic semiconductors. This section provided three numerical examples to illustrate the computational efficiency and accuracy of the Fr-DD model solver, and then presented an experimental validation of the Fr-DD model for a bendable OFET.

##### 4.3.1 Numerical Examples

Three numerical examples were devised to evaluate the accuracy and demonstrate the computational performance of the solver developed for the Fr-DD model. All of the numerical computations below were based on a MATLAB (R2019b) subroutine and performed on a laptop (MacBook Pro 2019) with Intel Core i9 CPU and 16 GB of RAM.

**Example 4.1** Consider the following single-carrier transport problem with fractional derivatives in both time and space for  $(x, y) \in \Omega$  and  $t > 0$ ,

$$-\Delta\varphi = \nabla \cdot \underline{u} = -n \quad (4.3)$$

$$\frac{\partial^\alpha n}{\partial t^\alpha} - k \nabla \cdot (\underline{un}) - \left( \frac{\partial^{\beta+1}}{\partial x^{\beta+1}} + \frac{\partial^{\beta+1}}{\partial y^{\beta+1}} \right) n = f(x, y, t) \quad (4.4)$$

where  $\Omega = (0,1) \times (0,1)$ ,  $0 < \alpha \leq 1$ , and  $0 < \beta \leq 1$ . The exact solution (ground truth) to this problem can be prescribed as Equations (4.5) and (4.6).

$$\varphi = -\frac{1}{2\pi^2} \exp(-2\pi^2 t) \sin(\pi x) \sin(\pi y) \quad (4.5)$$

$$n = \exp(-2\pi^2 t) \sin(\pi x) \sin(\pi y) \quad (4.6)$$

It can be shown that the above solution exists if and only if the nonlinear term on the right hand side of Equation (4.4) is given by

$$\begin{aligned} f(x, y, t) = & -2\pi^2 t^{1-\alpha} \mathcal{E}_{1,2-\alpha}(-2\pi^2 t) \sin(\pi x) \sin(\pi y) \\ & - \frac{k}{2} \exp(-4\pi^2 t) (\cos(2\pi x) \sin^2(\pi y) + \sin^2(\pi x) \cos(2\pi y)) \\ & - \exp(-2\pi^2 t) \left[ \pi^{\beta+1} \sin(\pi x + \frac{(\beta+1)\pi}{2}) \sin(\pi y) \right. \\ & \left. + \pi^{\beta+1} \sin(\pi y + \frac{(\beta+1)\pi}{2}) \sin(\pi x) \right] \end{aligned} \quad (4.7)$$

Example 4.1 is a benchmark problem constructed by the method of manufactured solutions (Roache, 2002). The exact solution at  $t = 0.02$  s is shown in Figure 4.24. The numerical solutions obtained by the solver developed in section 3.3.1 will be compared to the exact solution to evaluate the convergence order of the computation scheme. The error in this example is calculated by Equation (4.8).

$$e(\tau, \Delta x, k) = \frac{1}{N^2} \sqrt{\sum_{i=1}^N \sum_{j=1}^N |n_{i,j}^k - n(i\Delta x, j\Delta x, k\tau)|^2} \quad (4.8)$$

where  $N$  is the number of internal grid points, the spatial step size in the  $x$  and  $y$  dimensions are the same and given by  $\Delta x = \Delta y = 1/(N+1)$ .

To verify the convergence order in time, the spatial step size  $\Delta x$  should be made small enough, such as  $\Delta x = 0.01$  to ensure that the spatial discretization error is much smaller than the time discretization error. If the spatial step size is fixed and the temporal step size is varying, the numerical error and CPU time are recorded in Table 4.6 and Table 4.7. Table 4.6 compares three different combinations of  $\alpha$  and  $\beta$  with  $\beta$  fixed to 1. It is shown in Table 4.6 that the



convergence order in time is not a constant zero, which implies that the convergence order in time has a direct but no fixed relationship with the time-derivative order  $\alpha$ .

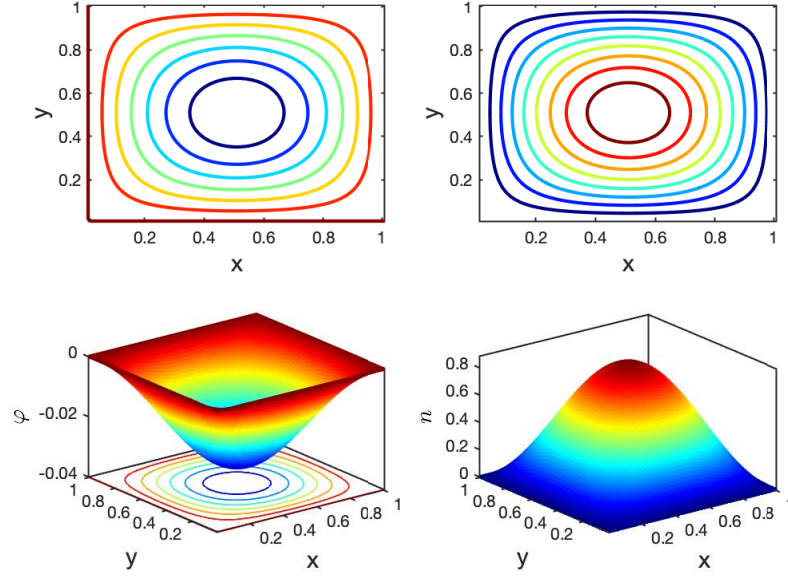


Figure 4.24 The contour plots (top) and surface plots (bottom) for the electrostatic potentials  $\varphi$  (left) and the electron concentration  $n$  (right) at  $t=0.02s$  (Y. Yang et al., 2021b).

Table 4.6. The errors, numerical convergence order in time and CPU time under different temporal step sizes  $\tau$  with fixed spatial step size  $\Delta x = 0.01$  and fixed space-derivative order  $\beta = 1$  (Y. Yang et al., 2021b).

$\tau$	$\alpha = 1, \beta = 1$				$\alpha = 0.9, \beta = 1$				$\alpha = 0.8, \beta = 1$		
	error	order	CPU Time		error	order	CPU Time		error	order	CPU Time
1/100	1.118e-4		15.8		7.443e-5		15.6		4.443e-5		16.1
1/200	5.416e-5	1.046	26.4		3.085e-5	1.271	26.2		1.277e-5	1.799	27.3
1/400	2.300e-5	1.236	49.0		8.391e-6	1.878	48.9		3.033e-6	2.074	49.6
1/800	6.886e-6	1.740	89.5		3.141e-6	1.418	88.7		1.103e-6	1.459	91.4
1/1600	2.005e-6	1.780	156.8		9.358e-7	1.747	155.2		3.946e-7	1.483	162.8

The analysis results for three groups of combined  $\alpha$  and  $\beta$  with  $\alpha$  fixed to 1 are presented in Table 4.7. It is shown in Table 4.7 that the convergence orders in time are all around zero no matter how the space-derivative order  $\beta$  changes. This finding implies that the convergence order in time has no direct relationship with  $\beta$ . The reason why different  $\beta$  changes the error but cannot change the convergence order in time is that the overall computational error is dominated by the error arising from the approximation of fractional integrals. If  $\beta$  is fixed to a value, the

approximation error for fractional integrals is determined by Equation (3.92), thus the overall error is also determined. Besides, another notable observation from Table 4.6 and Table 4.7 is that the speed at which the CPU time increases is less than the speed at which the temporal step size reduces. This slower increasing rate in CPU time means that the computational error can be reduced to any pre-required level at the cost of a relatively small increase in CPU time.

Table 4.7. The errors, numerical convergence order in time and CPU time under different temporal step sizes  $\tau$  with fixed spatial step size  $\Delta x = 0.01$  and fixed time-derivative order  $\alpha = 1$  (Y. Yang et al., 2021b).

$\tau$	$\alpha = 1, \beta = 0.9$			$\alpha = 1, \beta = 0.8$			$\alpha = 1, \beta = 0.7$		
	error	order	CPU Time	error	order	CPU Time	error	order	CPU Time
1/100	5.936e-4		18.2	8.205e-4		17.8	8.828e-4		18.7
1/200	5.639e-4	0.074	27.9	7.976e-4	0.040	28.7	8.590e-4	0.039	31.7
1/400	5.485e-4	0.040	55.8	7.860e-4	0.021	53.4	8.472e-4	0.020	58.4
1/800	5.407e-4	0.020	111.5	7.802e-4	0.011	104.2	8.413e-4	0.010	109.1
1/1600	5.368e-4	0.010	181.4	7.773e-4	0.005	194.5	8.384e-4	0.005	201.5

Table 4.8. The errors, numerical convergence order in space and CPU time under different spatial step sizes  $\Delta x$  with fixed temporal step size  $\tau = 1e - 5$  and fixed space-derivative order  $\beta = 1$  (Y. Yang et al., 2021b).

$\Delta x$	$\alpha = 1, \beta = 1$			$\alpha = 0.9, \beta = 1$			$\alpha = 0.8, \beta = 1$		
	error	order	CPU Time	error	order	CPU Time	error	order	CPU Time
0.2	1.605e-3		43.1	1.764e-3		41.2	2.037e-3		41.9
0.1	1.050e-4	3.934	106.5	8.078e-5	4.449	108.5	7.632e-5	4.738	116.7
0.05	1.084e-5	3.276	305.9	3.446e-5	1.229	298.7	5.169e-5	0.562	307.6

Table 4.9. The errors, numerical convergence order in space and CPU time under different spatial step sizes  $\Delta x$  with fixed temporal step size  $\tau = 1e - 5$  and fixed time-derivative order  $\alpha = 1$  (Y. Yang et al., 2021b).

$\Delta x$	$\alpha = 1, \beta = 0.9$			$\alpha = 1, \beta = 0.8$			$\alpha = 1, \beta = 0.7$		
	error	order	CPU Time	error	order	CPU Time	error	order	CPU Time
0.2	9.323e-3		48.3	1.346e-2		56.8	1.522e-2		52.2
0.1	4.146e-3	1.169	158.3	6.313e-3	1.092	170.4	7.220e-3	1.076	175.8
0.05	2.182e-3	0.926	343.2	3.296e-3	0.938	363.7	3.716e-3	0.958	396.4

To inspect the convergence order in space, a sufficiently small temporal step size  $\tau = 0.00001$  is taken to guarantee that the temporal discretization error can be ignored compared to a relatively larger spatial error. Similar to Table 4.6 and Table 4.7, the errors and CPU time for three groups of combined  $\alpha$  and  $\beta$  are given in Table 4.8 and Table 4.9. In Table 4.8,  $\beta$  is fixed

to 1 and  $\alpha$  takes different values. It is found that the convergence order in space is not a constant in  $\alpha$ , and the order decreases rapidly as the spatial step size decreases. In Table 4.9,  $\alpha$  is fixed to 1 and  $\beta$  takes three different values. It is shown in Table 4.9 that all the convergence orders in space are very close to 1, which reveals a linear dependency of the overall error on the spatial step size for  $\beta < 1$ . The CPU time in different spatial step size does not increase at a rate as similar as what is observed in Table 4.6 and Table 4.7. However, given that the growth rate of the number of discrete spatial grids is the square of the reduction rate of the spatial step size, the CPU time can still be considered to increase at a relatively slower rate compared to the growing rate of the spatial grid points. Based on all the observations above, it can be suggested that the overall computational error can be limited to a certain level at the expense of a relatively slower increase in the CPU time.

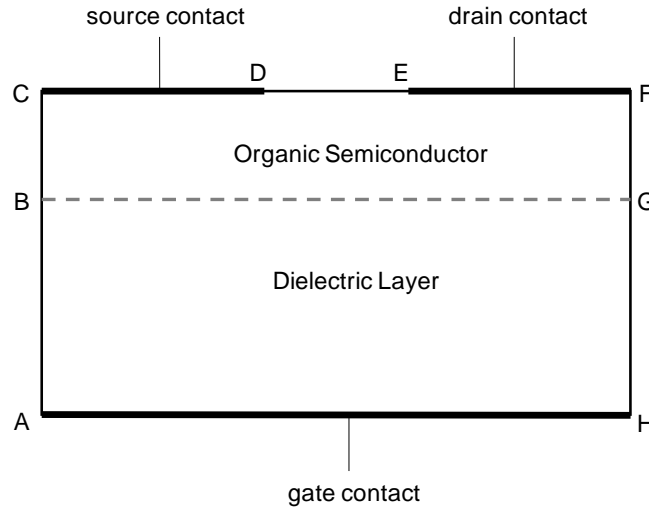


Figure 4.25 The geometry of a 2D top-contact bottom-gate (TCBG) OFET with the active layer made from a p-type organic semiconductor (Y. Yang et al., 2021b).

**Example 4.2** Consider the following steady-state single-carrier transport problem in a 2D p-type organic field effect transistor (OFET),

$$-\Delta\varphi = \nabla \cdot \underline{u} = \frac{qp}{\varepsilon_r \varepsilon_0} \quad (4.9)$$

$$0 = -\mu_p \nabla \cdot (\underline{u}p) + D_p \left( \frac{\partial^{\beta+1}}{\partial x^{\beta+1}} + \frac{\partial^{\beta+1}}{\partial y^{\beta+1}} \right) p + G_p \quad (4.10)$$

where the effective hole mobility  $\mu_p$  and diffusion coefficient  $D_p$  are constants for homogeneous materials. The net generation-recombination rate  $G_p \approx 0$  since the generation and recombination

activities are relatively unimportant in OFETs as a majority carrier device (Dev Dhar Dwivedi et al., 2020; Haubold et al., 2011). The solution domain is defined in Figure 4.25, where the size of the organic semiconductor (OSC) layer is  $500 \mu\text{m} \times 30 \text{ nm}$  and the size of the dielectric layer is  $500 \mu\text{m} \times 64 \text{ nm}$ . The parameters for OFET simulation are presented in Table 4.10, and the diffusion coefficient for the OSC is determined by Einstein's relation  $D_p = V_T \mu_p$ . The geometric sizes and the material types of the OFET domain are selected to be the same as those in section 3.2. In addition, the OFET in this numerical example is not encapsulated by an outer layer in order to simplify boundary conditions.

Table 4.10. The model parameters utilized for Example 4.2 (Y. Yang et al., 2021b).

$q$ (C)	$\epsilon_p$	$\epsilon_d$	$\mu_p$ (m <sup>2</sup> /Vs)	$V_T$ (V)
Basic electric charge	Relative permittivity for OSC	Relative permittivity for dielectric	Hole mobility for OSC	Thermal voltage
1.60217646e-19	3.0	3.9	4.5e-5	0.0255

Equations (4.9) and (4.10) are subject to proper boundary conditions. To make sure that the OFET is self-contained, the boundaries AB, BC, DE, FG and GH should be regulated by Neumann conditions, i.e.,  $\frac{\partial \varphi}{\partial n} = 0$  and  $\frac{\partial p}{\partial n} = 0$ , where  $n$  is the unit norm vector to the boundary. Assume that the metal-semiconductor (MS) contacts on CD and EF are ohmic contacts and the barrier voltage is zero, the potentials on CD and EF are specified by  $\varphi_{CD} = 0$  and  $\varphi_{EF} = -1.5 \text{ V}$ . Similarly, the boundary potential on AH is specified by  $\varphi_{AH} = -3.0 \text{ V}$ . These electrostatic potential values specified on the boundary are all selected properly, because the OFET has been proved to work normally under these boundary values (Y. Yang et al., 2021a). If the dielectric layer is assumed to be ideally isolated, the hole concentration on region ABGH can remain a constant zero. The OSC and the dielectric layer interface (BG) requires the continuity of the dielectric displacement, i.e.,  $\epsilon_p \frac{\partial \varphi}{\partial n} \Big|_{BG} = \epsilon_d \frac{\partial \varphi}{\partial n} \Big|_{BG}$ . The hole concentration on MS contacts (i.e., boundaries CD and EF) are assumed to satisfy Dirichlet conditions:  $p_{CD} = p_{EF} = 5e6 \text{ m}^{-3}$ .

Given these boundary conditions, the electrostatic potentials and hole concentration in the OFET domain can be solved by applying algorithm 2. However, it is worth noting that the numerical solutions in examples 4.1 and 4.2 can only be obtained for the cases where beta is not

less than 0.7 since the four generalized reversed state transition functions  $\hat{\Phi}_i(\Delta x)$  ( $i = 1, 2, 3, 4$ ) may blow up to infinity when  $\Delta x$  is small and  $\beta < 0.7$ . In the cases of  $\beta = 1$  and  $\beta = 0.8$ , the specified boundary conditions and obtain the simulated surface plots of electrostatic potentials and hole concentration in Figure 4.26. It can be observed that the electrostatic potential profile is not significantly affected by the selection of different  $\beta$ . Nevertheless, the profile of the hole concentration under different  $\beta$  are visibly shifted along the thickness direction. The different effects of  $\beta$  on  $\varphi$  and  $p$  are mainly due to the fact that  $\beta$  is only related to the intensity of the diffusive motion of the carriers.

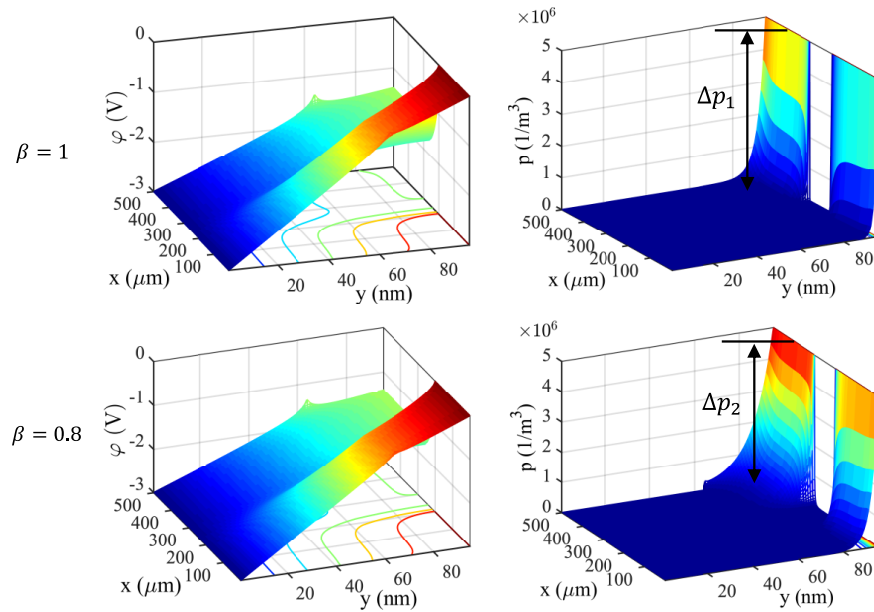


Figure 4.26 The simulated electrostatic potentials and hole concentration in the OFET for space-derivative order  $\beta = 1$  and  $\beta = 0.8$  (Y. Yang et al., 2021b).

The current density has drifting and diffusive components, i.e.,  $J = -q\mu_p p \nabla \varphi - qD_p {}^C\nabla_r^\beta p$ . The diffusive component is proportional to the fractional gradient operator  ${}^C\nabla_r^\beta p$ , where  ${}^C\nabla_r^\beta p = ({}_0^C D_x^\beta p \quad {}_0^C D_y^\beta p)$ . The fractional derivative can be approximated by  ${}_0^C D_y^\beta p \approx \frac{\Delta p}{\Delta y^\beta}$ . As can be seen in Figure 4.26, the concentration within a single step size complies with  $\Delta p_1 > \Delta p_2$  and  $\Delta y < \Delta y^{0.8}$ , thus it holds that  ${}_0^C D_y^1 p > {}_0^C D_y^{0.8} p$ . This result suggests that the carriers' diffusive motion will be enhanced when  $\beta$  is larger.

Because it is almost impossible to find an initial value condition consistent with the

boundary conditions in the OFET, the transient solution that can approach the steady-state solution over time can hardly be obtained for this example. To explore the effects of time-derivative order  $\alpha$  on the transient dynamics, a 2D photon-agitated solar cell will be considered in the next example.

**Example 4.3** Consider the following single-carrier transport problem in a 2D p-type solar cell in both time and space for  $(x, y) \in \Omega$  and  $t > 0$ ,

$$-\Delta\varphi = \nabla \cdot \underline{u} = \frac{qp}{\varepsilon_r \varepsilon_0} \quad (4.11)$$

$$\frac{\partial^\alpha p}{\partial t^\alpha} = -\mu_p \nabla \cdot (\underline{u}p) + D_p \left( \frac{\partial^{\beta+1}}{\partial x^{\beta+1}} + \frac{\partial^{\beta+1}}{\partial y^{\beta+1}} \right) p + p(x, y, 0) \frac{t^{-\alpha}}{\Gamma(1-\alpha)} \quad (4.12)$$

where  $\Omega = (0, L) \times (0, L)$ ,  $0 < \alpha \leq 1$ , and  $0 < \beta \leq 1$ . The initial value condition is given by Equation (4.13),

$$p(x, y, 0) = \frac{10000p_0}{\sqrt{2\pi}L} \exp\left(-\frac{(x-0.5L)^2 + (y-0.5L)^2}{2 \times 10^{-8}L}\right) \quad (4.13)$$

and the boundary conditions are specified as  $p|_{\partial\Omega} = 0$ ,  $\frac{\partial\varphi}{\partial n}|_{\partial\Omega} = 0$ , where  $n$  is the unit normal vector to the boundary surfaces. The other system parameters for this solar cell are presented in Table 4.11. In this example, it is intentionally required that the kernel radius of the initial hole concentration is much smaller than the side length of the solution domain, i.e.,  $0.00001L \ll L$ , so that the boundary condition ( $p|_{\partial\Omega} = 0$ ) and the initial value condition can be consistent. The consistency guarantees the solvability of the transient dynamics of the solar cell problem.

Table 4.11. The model parameters utilized for Example 4.3 (Y. Yang et al., 2021b).

$L$ (m)	$\varepsilon_0$ (F/m)	$\varepsilon_r$	$\mu_p$ (m <sup>2</sup> /Vs)	$p_0$ (1/m <sup>3</sup> )
The side length of the domain	Vacuum permittivity	Relative permittivity for OSC	Hole mobility for OSC	Initial hole concentrations agitated by the light pulse
1e-6	8.854e-12	3.0	4.5e-5	1e22

In Example 4.3, the spatial and the temporal step sizes are set to be  $1e-8$  m and  $1e-6$  s, respectively. If  $\beta = 1$  and  $\alpha$  is taken different values in 0.8, 0.6 and 0.4, the transient solutions at  $t = 1e-5$  s can be easily obtained by applying algorithm 1. As shown in Figure 4.27(a), the hole concentration exhibits a decaying trend with the decrease of  $\alpha$ , while the electrostatic

potential remains almost unchanged for different  $\alpha$ . The decay trend observed in hole concentration can be explained as that the hole concentration with smaller  $\alpha$  will reduce more in a single step of time advancement (i.e.,  $\Delta p \approx C\tau^\alpha$ ). In the second setting, it is required that  $\alpha = 0.9$  and  $\beta = 1, 0.8$  and  $0.6$ . Similarly, the transient solution at  $t = 1e - 5$  s can be obtained in Figure 4.27(b). It is found in Figure 4.27(b) that the decaying rate for the hole concentration will be reduced as  $\beta$  decreases. This phenomenon is believed to be caused by the inactive diffusive motion of carriers under smaller  $\beta$ .

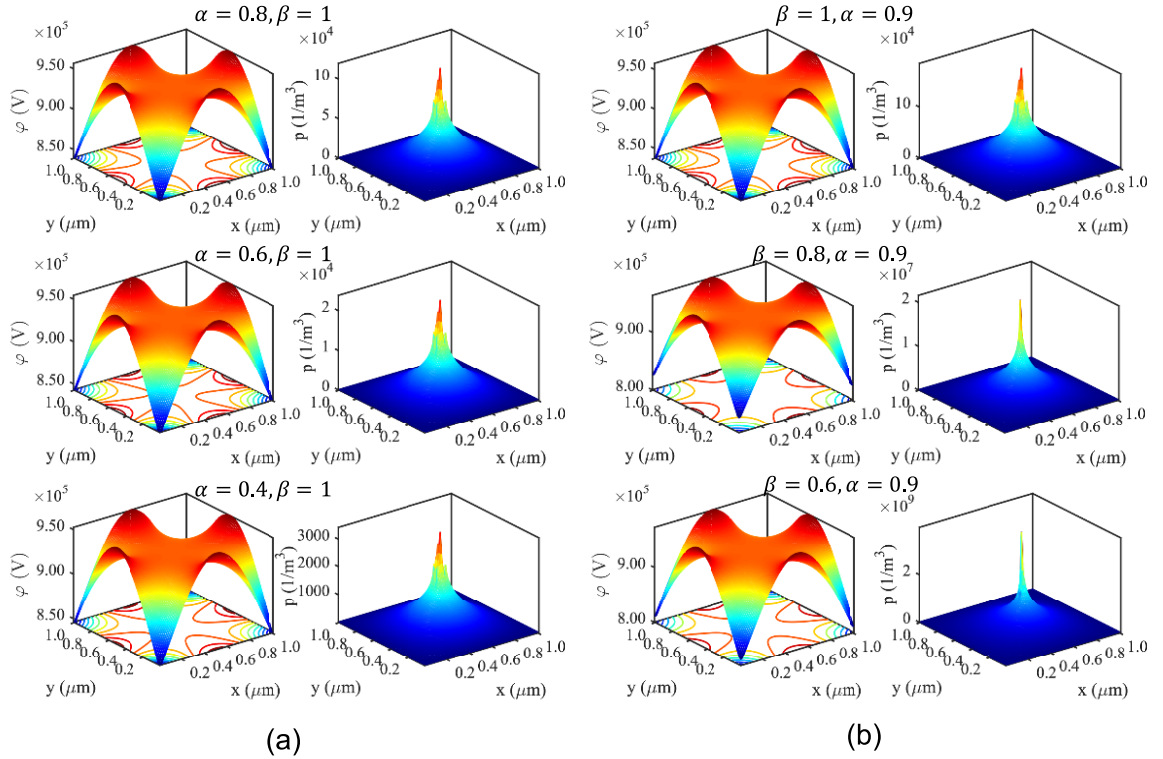


Figure 4.27 The simulated transient-state electrostatic potentials and hole concentration in the solar cell when (a) space-derivative order  $\beta = 1$  is fixed and  $\alpha = 0.8, 0.6$  and  $0.4$ , respectively; (b) time-derivative order  $\alpha = 0.9$  is fixed and  $\beta = 1, 0.8$  and  $0.6$ , respectively (Y. Yang et al., 2021b).

#### 4.3.2 Experimental Validation of the Fr-DD Model for Pre-bent OFET

In Example 4.2, the boundary conditions were simplified to better discuss the influence of  $\beta$  values on the carriers' diffusive motion. As an extended investigation on Example 4.2, this section provided the experimental validation of the Fr-DD model for the OFET. The fabrication

and the experimental characterization of the OFET was discussed in section 4.2.1. As shown in Figure 4.28, compared to the simplified structure of the OFET in Example 4.2, the complete structure of the OFET is encapsulated in an outer layer made from Parylene. The metallic electrodes have a thickness of 30 nm, and the other material properties are specified in Table 4.10. Besides the boundary conditions given in Example 4.2, the encapsulating layer should also be treated as an ideal insulator, where no charge carrier transport is permitted.

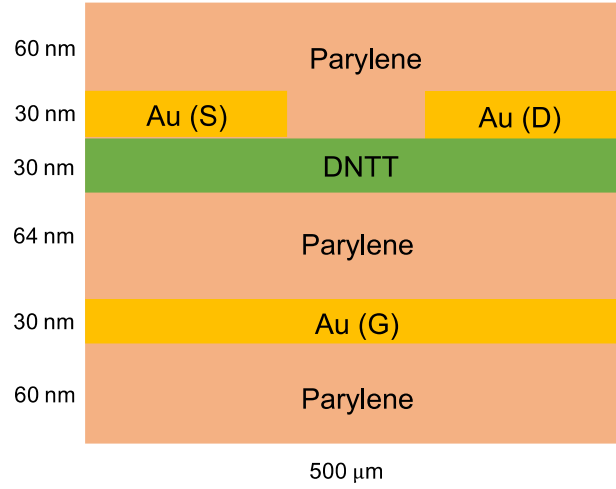


Figure 4.28 The solution domain of a 2D top-contact bottom-gate (TCBG) OFET device composed of a p-type organic semiconductor layer, a dielectric layer and encapsulating layers (top and bottom) (Y. Yang et al., 2021b).

Given that the length of the source electrode  $L_S$  and the drain electrode  $L_D$  are both  $200 \mu\text{m}$  and the width of the OFET (out-of-plane dimension)  $W$  is  $1000 \mu\text{m}$ , the net current flowing through the drain electrode can be evaluated by Equation (4.14),

$$\begin{aligned}
 I_{ds} &= W \int_0^{L_D} J_y(x) dx \approx W \sum_{i_D=1}^{L_D/\Delta x} JY_{i_D, j_D} \cdot \Delta x \\
 &= W \sum_{i_D=1}^{L_D/\Delta x} \frac{(\hat{\Phi}_1(\Delta y) p_{i_D, j_D-1} - p_{i_D, j_D}) q D_p}{j_{0+}^\beta \hat{\Phi}_1(\Delta y)} \cdot \Delta x
 \end{aligned} \tag{4.14}$$

where  $J_y$  is the component of the continuous current density that is normal to the Au-DNTT interface,  $i_D$  is the discrete index for grid points in the x direction and  $j_D$  is the discrete index for the grid points in the y direction. In this experiment, the spatial step sizes are  $\Delta x = 5 \mu\text{m}$  and



$\Delta y = 1$  nm, so it is known that  $j_D = 184$ . By evaluating the summation in Equation (4.14) over  $i_D = 1, \dots, 40$ , the drain current can be obtained.

The  $\beta$  value in the OFET model depends on the spatial coordinates and the electrode potentials, i.e.,  $\beta = A(x, y, V_{gs}, V_{ds})$ . The inhomogeneity of  $\beta$  exhibited in the solution domain is caused by the irregular crystalline structure of OSCs and the electronic polarization under different boundary conditions (Erker & Hofmann, 2019; Valeev et al., 2006). If the dependence of  $\beta$  on spatial coordinates is ignored and only the dependences on  $V_{gs}$  and  $V_{ds}$  are considered, the relationship curves in Figure 4.29(b) and Figure 4.30(b) for  $\beta = A(V_{gs}, V_{ds})$  can be generated by fitting the theoretical curves to the experimental data.

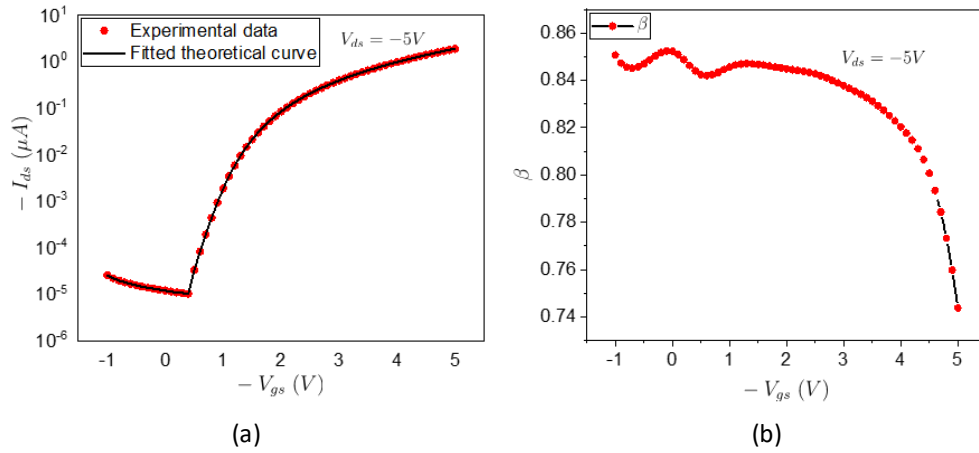


Figure 4.29 (a) The experimentally measured transconductance at a fixed  $V_{ds} = -5$  V compared with the fitted theoretical transconductance curve obtained from the Fr-DD model; (b) The adjusted pre-bent  $\beta$  values ( $\beta_b$ ) under different  $V_{gs}$  and a fixed  $V_{ds} = -5$  V (Y. Yang et al., 2021b).

When  $\beta$  is adjusted for a fixed  $V_{ds}$  and varying  $V_{gs}$  according to Figure 4.29(b), Equation (4.14) can be utilized to calculate the drain current  $I_{ds}$  under different  $V_{gs}$  and evaluate the theoretical transconductance. In Figure 4.29(a), it is found that the theoretical transconductance curve (solid black line) can agree well with the experimental measurements (red circles). Similarly, if  $\beta$  can be adjusted by the dependence curves in Figure 4.30(b), it can be seen that in Figure 4.30(a) the theoretical output curves (black solid lines) can well agree with the experimental data (Symbol, i.e., red circles, blue squares, etc.). These results confirm the validity

of the Fr-DD model for predicting the OFET characteristics, and also suggest the highly nonlinear dependence of  $\beta$  on the boundary potentials  $V_{gs}$  and  $V_{ds}$ . Due to the flexibility of adjusting  $\beta$ , the Fr-DD model avoids considering the involuted trap states in OSCs, thus greatly improving the modeling efficiency.

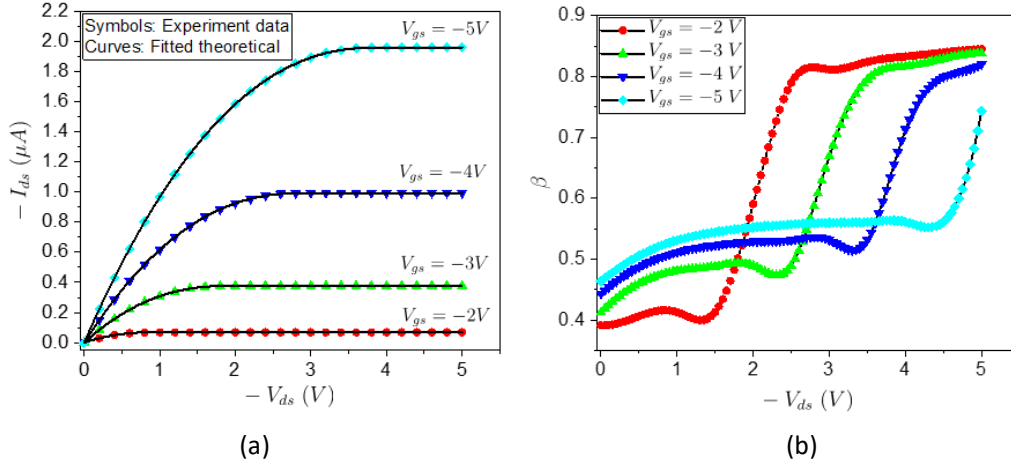


Figure 4.30 (a) The experimentally measured output curve (symbols) at a series of fixed  $V_{gs} = -5 \sim -2$  V compared with the fitted theoretical output curve (black solid lines) obtained from the Fr-DD model; (b) The adjusted pre-bent  $\beta$  values ( $\beta_b$ ) under different  $V_{ds}$  and a group of fixed  $V_{gs} = -5 \sim -2$  V (Y. Yang et al., 2021b).

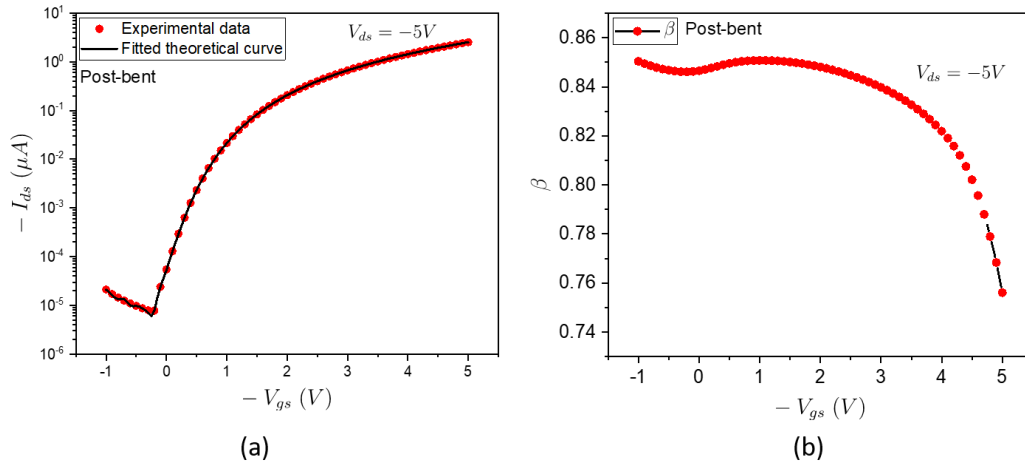


Figure 4.31 (a) The experimentally measured transconductance at a fixed  $V_{ds} = -5$  V compared with the fitted theoretical transconductance curve obtained from the Fr-DD model; (b) The adjusted post-bent  $\beta$  values ( $\beta_e$ ) under different  $V_{gs}$  and a fixed  $V_{ds} = -5$  V.

### 4.3.3 Experimental Validation of the Fr-DD Model for Post-bent OFET

The parameter  $\beta$  of the Fr-DD model of the post-bent OFET is different from the parameter  $\beta$  of the Fr-DD model of the pre-bent OFET. This section was dedicated to finding the connection between the pre-bent and post-bent parameter  $\beta$ , and establishing the relationship between  $\beta$  and  $\varepsilon$ . Following similar steps to those used to obtain Figure 4.29, the experimentally measured and the theoretically fitted transconductance for the post-bent OFET can be presented in Figure 4.31(a). Correspondingly, the dependence curve  $\beta = A(V_{gs}, V_{ds})$  at a fixed value of  $V_{ds}$  is shown in Figure 4.31(b).

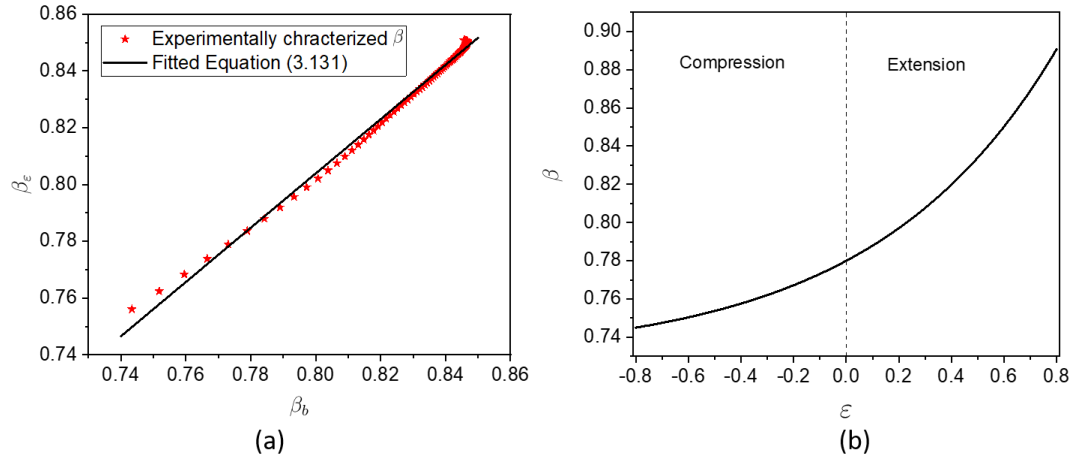


Figure 4.32 (a) The experimentally characterized post-bent  $\beta_\varepsilon$  as a function of the pre-bent  $\beta_b$  (red stars), the solid curve is obtained by fitting Equation (3.131) to the experimental data; (b) The relationship curve for the fitted Equation (3.131) when strain-free (pre-bent)  $\beta_b = 0.78$ .

Given that the values of  $\beta_b$  and the values of  $\beta_\varepsilon$  are known and can be read from Figure 4.29(b) and Figure 4.31(b), it is convenient to visualize the relationship between  $\beta_\varepsilon$  and  $\beta_b$  as red stars in Figure 4.32(a). The pre-bent and post-bent  $\beta$  relationship (i.e.,  $\beta_\varepsilon$  vs  $\beta_b$ ) can lead to more useful treatment of Equation (3.131), which gives the correlation between  $\beta$  and the mechanical strain  $\varepsilon$ . By applying the least square method to the outputs of Equation (3.131), an approximated relationship curve for  $\beta_\varepsilon$  vs  $\beta_b$  (solid black line) can be obtained to fit the experimentally characterized  $\beta$  (red stars) in Figure 4.32(a). It is shown in Figure 4.32(a) that the fitted curve for Equation (3.131) demonstrates a high degree of agreement with the experimental characterized  $\beta$ , especially for  $\beta_b$  around 0.84, under which the OFET works exactly in the

subthreshold regime. The least square calculations render a set of values for the unknown parameters in Equation (3.131):  $\beta_a = 0.8884$ ,  $h = 1.44$  and  $\varepsilon_{max} = 0.7899$ . Given these parameters, the curve of the relationship between  $\beta$  and  $\varepsilon$  can be determined by Equation (3.131). In the case of  $\beta_b = 0.78$ , for example, the  $\beta$  vs  $\varepsilon$  relationship curve can be plotted in Figure 4.32(b). The curve shown in Figure 4.32(b) complies with the model developed in section 3.3.3 for the parameter  $\beta$  and mechanical strain  $\varepsilon$ , it can be found that when the bent OFET exhibits an overall tensile strain at the semiconductor-dielectric interface, the strain-induced  $\beta$  will be greater than  $\beta_b$  and will increase as the strain  $\varepsilon$  increases. The relationship between  $\beta$  and  $\varepsilon$  is reversed when the bent OFET has a compressive strain at the semiconductor-dielectric interface as a whole.

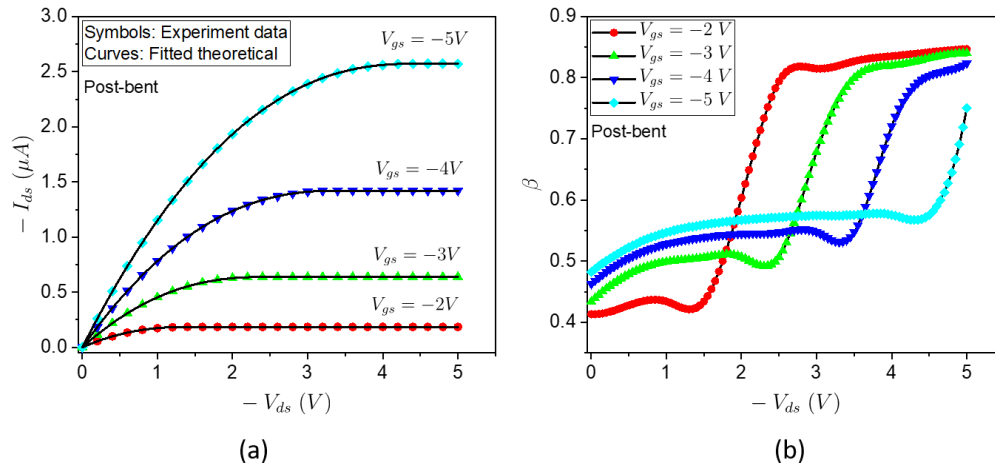


Figure 4.33 (a) The experimentally measured output curves (symbols) at a series of fixed  $V_{gs} = -5 \sim -2$  V compared with the theoretically predicted output curves (black solid lines) obtained from the Fr-DD model; (b) The cross-validated post-bent  $\beta$  values ( $\beta_\varepsilon$ ) under different  $V_{ds}$  and a group of fixed  $V_{gs} = -5 \sim -2$  V obtained by applying Equation (3.131) to the adjusted pre-bent  $\beta$  values ( $\beta_b$ ).

By applying Equation (3.131) to the pre-bent dependence of  $\beta$  on  $V_{ds}$ , the post-bent dependence of  $\beta$  on  $V_{ds}$  for fixed  $V_{gs} = -5 \sim -2$  V can be obtained in Figure 4.33(b) and cross-validated. As shown in Figure 4.33(a), if the Fr-DD model parameter  $\beta$  is adjusted according to the cross-validated  $\beta_\varepsilon = A(V_{ds})$  shown in Figure 4.33(b), the theoretical output characteristic curves (black solid lines) predicted by the Fr-DD model are in good agreement with the

experimental measurements. These findings suggest that the Fr-DD model is capable of characterizing undeformed OFETs without needing to take into account the multiple trap states, and can also predict the electrical characteristics of deformed OFETs in the whole  $V_{gs}$  regimes (linear, saturation and subthreshold regimes). It can therefore be assumed that the Fr-DD model can be extended to the prediction of post-strain electrical characteristics of other organic semiconductor devices as well.

#### 4.4 Summary

In chapter four, simulations were conducted to demonstrate the computational performance of the MSD model, generalized solid-state model and the Fr-DD model in the predictions of the strain induced characteristics of TFTs and OFETs. It is revealed that the MSD model can have much better performance than the FEA model in terms of computational efficiency and storage efficiency. When paired with an electromechanical coupling relationship, the MSD model can be used to investigate changes in the electrical response of TFTs on the skin surface. In the solid-state model for an OFET, the relative number of trap states in the generalized solid-state model can be reflected by the parameter  $\gamma$  in the generalized current-voltage equations. The generalized solid-state model for  $\gamma = 1.3$  was then verified by observing that the theoretical predicted curves for a bendable DNTT OFETs can have a good agreement with the experimental measurements in the linear and saturation regimes.

In the Fr-DD model, three numerical examples, including one benchmark example and two others constructed from the perspective of engineering applications were employed to demonstrate the algorithms' accuracy and computational performance. It is found in the first example that altering  $\alpha$  and  $\beta$  can impact the spatial convergence order, but only varying  $\alpha$  will affect the convergence order in time. The increase rate of CPU time is less than the shrinking rate of temporal step size and lower than the growth rate of spatial grid points. These findings suggest that the solver developed for the Fr-DD model has high precision and fast computational speed as it limits the computational error to a predefined satisfactory level (from  $\sim 10^{-4}$  to  $\sim 10^{-6}$ ) at a relatively small expense of CPU time (from  $\sim 20$  s to  $\sim 100$  s). The results reported in the other two numerical examples reveal the possibility of the Fr-DD model for the prediction and characterization of the transient-state and steady-state dynamics of any types of organic semiconductor device. Finally, the experimental validations were provided for the Fr-DD model

of a bendable OFET. The study in section 4.3 is the first to date exploration of the Fr-DD model solver laying the groundwork for future research into fractional drift diffusion modeling of flexible organic electronics.

## CHAPTER 5. CONCLUSION AND FUTURE WORK

In this dissertation, three electromechanical models for the deformable OFETs were created and analyzed using the pure mathematical tools, physical theories, engineering numerical simulations, and experimental validation techniques. The first one is the mass-spring-damper (MSD) model that focuses on the modeling of mechanical stress and strain in thin-film structure with arbitrary geometry and boundary excitations. The second model is the generalized solid-state model that considers the massive density of trap states in the semiconductor band structure. When equipped with an electromechanical coupling relationship, the generalized solid-state model was demonstrated to successfully characterize the electrical characteristics of a bendable OFET before and after bending. The third model is the fractional drift-diffusion (Fr-DD) model, which investigates the fractional-order drifting and diffusive transport behaviors of carriers in organic semiconductor devices. In addition to the generalized drifting and diffusive descriptions of OFETs, the Fr-DD model is capable of characterizing and predicting the post-bent response of the OFETs by considering another electromechanical coupling relationship that gives the dependence of the Fr-DD model parameter  $\beta$  on the mechanical strain  $\varepsilon$  at the semiconductor-dielectric interface. The summary of contributions for the scientific community and the recommendations for future work of the three electromechanical models for organic semiconductor or generic flexible electronic devices are discussed in this chapter.

### 5.1 Contribution

The three main contributions of this work to the community of flexible electronics, organic field effect transistors, and multiphysics modeling include:

- The dissertation proposed the MSD model to address the issue of the excessive consumption of computational and computer memory resources in the mechanical modelling of flexible electronic devices. By simulating the internal stress-strain field of a ZnO-TFT attached to a skin surface, it is found that the MSD model has greatly improved the computational efficiency by 30% and resource utilization by 60% compared to the conventional FEA model.
- The dissertation studied the effect of different trap state levels in organic semiconductors

on the carrier hopping through the energy band and developed a generalized solid-state model to account for and quantify the trap states in organic semiconductors. The generalized solid-state model is applicable to any field-effect transistor (FET) with different structures or semiconductor materials, including inorganic TFTs and MOSFETs.

- The dissertation derived an electromechanical coupling relationship to explain the effect of mechanical strain on carrier mobility and threshold voltage in FETs. Combined with this electromechanical coupling relationship, the generalized solid-state model well characterized the transconductance and output of bendable OFETs in the linear and saturation regimes. The parameters of the physically based generalized solid-state model and the electromechanical coupling relationship can be extracted very easily from the limited experimental data.
- The dissertation also created the Fr-DD model that can be used to describe the transient and steady-state dynamics of arbitrary organic semiconductor devices. The dissertation developed two algorithms for solving the Fr-DD model and verified the consistency and convergence of the algorithms with rigorous mathematical analysis. The proposed algorithms were shown to have high accuracy and fast convergence through several benchmark and engineering numerical examples.
- The dissertation proposed an electromechanical coupling relationship between the Fr-DD model parameter  $\beta$  and mechanical strain  $\varepsilon$ . This relationship allows the Fr-DD model to characterize the transient and steady-state response of an organic semiconductor device undergoing mechanical deformation.

## 5.2 Recommendations

Two significant research issues to further enrich the developed electromechanical models for OFETs are discussed in this section.

- The electromechanical coupling relationship developed for the generalized solid-state model will be further tested on OFETs under different bending radii. In this dissertation, simulations were conducted to validate the effectiveness of the proposed electromechanical coupling relationship and generalized solid-state model for a bendable OFET with a fixed bending radius. However, the bending radius of the OFET in the practical situations is dynamically changing, so in the future work, the proposed



electromechanical coupling relationship will be further improved based on simulations and experimental measurements of bendable OFETs with different bending radii.

- The electromechanical model presented in the dissertation will be extended to the modelling and simulation of flexible organic electrochemical transistors (OECTs). The OECT is a transistor in which the current conduction is controlled by the injection of ions from a liquid electrolyte into the thin-film channel at the semiconductor-electrolyte interface. The flexible OECT can more closely match the form factor of the detecting surface and allow for more conformal surface contact. Modelling and simulation of flexible OECTs, which have a more complex internal structure but operate in a similar mechanism to OFETs, often present more unforeseen challenges. Therefore, the application and extension of the models and methods in this dissertation to flexible OECTs will bring convenience and improvements to the characterization of flexible sensors and actuators.

## REFERENCES

- Alam, M. A., Dodabalapur, A., & Pinto, M. R. (1997). A two-dimensional simulation of organic transistors. *IEEE Transactions on Electron Devices*, 44(8), 1332–1337. <https://doi.org/10.1109/16.605477>
- Alaria, A., Khan, A. M., Suthar, D. L., & Kumar, D. (2019). Application of Fractional Operators in Modelling for Charge Carrier Transport in Amorphous Semiconductor with Multiple Trapping. *International Journal of Applied and Computational Mathematics*, 5(6), 167. <https://doi.org/10.1007/s40819-019-0750-8>
- Alius, H., Rempp, H., Yu, Z., & Gneiting, T. (2014). *A New MOSFET Model for the Simulation of Circuits under Mechanical Stress*.
- Ana, F., & Din, N. ud. (2018). Design and performance investigation of short channel bottom-contact organic thin-film transistors. *Journal of Computational Electronics*, 17(3), 1315–1323. <https://doi.org/10.1007/s10825-018-1170-4>
- Ana, F., & Najeeb-ud-Din. (2019). An analytical modeling approach to the electrical behavior of the bottom-contact organic thin-film transistors in presence of the trap states. *Journal of Computational Electronics*, 18(2), 543–552. <https://doi.org/10.1007/s10825-019-01314-6>
- Antoniadis, H., & Schiff, E. A. (1991). Unraveling the  $\mu\tau$ -mystery in a-Si:H. *Journal of Non-Crystalline Solids*, 137–138(PART 1), 435–438. [https://doi.org/10.1016/S0022-3093\(05\)80148-6](https://doi.org/10.1016/S0022-3093(05)80148-6)
- Aziz, M. J. (1998). Pressure and stress effects on diffusion in Si. *Defect and Diffusion Forum*, 153–155, 1–10. <https://doi.org/10.4028/www.scientific.net/ddf.153-155.1>
- Aziz, Michael J., Zhao, Y., Gossmann, H. J., Mitha, S., Smith, S. P., & Schiferl, D. (2006). Pressure and stress effects on the diffusion of B and Sb in Si and Si-Ge alloys. *Physical Review B - Condensed Matter and Materials Physics*, 73(5), 054101. <https://doi.org/10.1103/PhysRevB.73.054101>
- Bank, R. E., Rose, D. J., & Fichtner, W. (1983). Numerical Methods for Semiconductor Device Simulation. *IEEE Transactions on Electron Devices*, 30(9), 1031–1041. <https://doi.org/10.1109/T-ED.1983.21257>
- Bardeen, J., & Shockley, W. (1950). Deformation potentials and mobilities in non-polar crystals. *Physical Review*, 80(1), 72–80. <https://doi.org/10.1103/PhysRev.80.72>
- Bauchau, O. A., & Craig, J. I. (2009). *Constitutive behavior of materials* (pp. 53–99). Springer. [https://doi.org/10.1007/978-90-481-2516-6\\_2](https://doi.org/10.1007/978-90-481-2516-6_2)

- Benson, D. A., Meerschaert, M. M., & Revielle, J. (2013). Fractional calculus in hydrologic modeling: A numerical perspective. *Advances in Water Resources*, 51, 479–497. <https://doi.org/10.1016/j.advwatres.2012.04.005>
- Bittle, E. G., Basham, J. I., Jackson, T. N., Jurchescu, O. D., & Gundlach, D. J. (2016). Mobility overestimation due to gated contacts in organic field-effect transistors. *Nature Communications*, 7(1), 1–7. <https://doi.org/10.1038/ncomms10908>
- Blaszczyk, T., Siedlecki, J., & Ciesielski, M. (2018). Numerical algorithms for approximation of fractional integral operators based on quadratic interpolation. *Mathematical Methods in the Applied Sciences*, 41(9), 3345–3355. <https://doi.org/10.1002/mma.4828>
- Bolintineanu, D. S., Sayyed-Ahmad, A., Davis, H. T., & Kaznessis, Y. N. (2009). Poisson-Nernst-Planck Models of Nonequilibrium Ion Electrodifffusion through a Protegrin Transmembrane Pore. *PLoS Computational Biology*, 5(1), e1000277. <https://doi.org/10.1371/journal.pcbi.1000277>
- Bradley, A. T., Jaeger, R. C., Suhling, J. C., & O'Connor, K. J. (2001). Piezoresistive characteristics of short-channel MOSFETs on (100) silicon. *IEEE Transactions on Electron Devices*, 48(9), 2009–2015. <https://doi.org/10.1109/16.944190>
- Brown, M. A. (2007). *Measuring Stress in Thin-Film - Substrate Systems Featuring Spatial Nonuniformities of Film Thickness and/or Misfit Strain* [California Institute of Technology]. <https://doi.org/10.7907/9GD9-A088>
- Cardoso, G. W. A., Leal, G., Da Silva Sobrinho, A. S., Fraga, M. A., & Massi, M. (2014). Evaluation of piezoresistivity properties of sputtered ZnO thin films. *Materials Research*, 17(3), 588–592. <https://doi.org/10.1590/S1516-14392014005000080>
- Cartea, Á., & del-Castillo-Negrete, D. (2007). Fractional diffusion models of option prices in markets with jumps. *Physica A: Statistical Mechanics and Its Applications*, 374(2), 749–763. <https://doi.org/10.1016/j.physa.2006.08.071>
- Caughey, D. M., & Thomas, R. E. (1967). Carrier Mobilities in Silicon Empirically Related to Doping and Field. *Proceedings of the IEEE*, 55(12), 2192–2193. <https://doi.org/10.1109/PROC.1967.6123>
- Chang, J., Lin, Z., Zhang, C., & Hao, Y. (2017). Organic Field-Effect Transistor: Device Physics, Materials, and Process. In *Different Types of Field-Effect Transistors - Theory and Applications*. InTech. <https://doi.org/10.5772/intechopen.68215>
- Chen, H. C., Huang, K. T., & Lo, Y. M. (2012). Measurement of residual stress for ITO/PET substrates by the double beam shadow moiré interferometer. *Applied Optics*, 51(10), 1566–1571. <https://doi.org/10.1364/AO.51.001566>
- Chen, R. C., & Liu, J. L. (2003). Monotone iterative methods for the adaptive finite element solution of semiconductor equations. *Journal of Computational and Applied Mathematics*, 159(2), 341–364. [https://doi.org/10.1016/S0377-0427\(03\)00538-7](https://doi.org/10.1016/S0377-0427(03)00538-7)

- Choo, K. Y., & Muniandy, S. V. (2015). Fractional dispersive transport in inhomogeneous organic semiconductors. *International Journal of Modern Physics: Conference Series*, 36, 1560008. <https://doi.org/10.1142/s2010194515600083>
- Choo, K. Y., Muniandy, S. V., Woon, K. L., Gan, M. T., & Ong, D. S. (2017). Modeling anomalous charge carrier transport in disordered organic semiconductors using the fractional drift-diffusion equation. *Organic Electronics*, 41, 157–165. <https://doi.org/10.1016/j.orgel.2016.10.041>
- Choudhary, A., Kumar, D., & Singh, J. (2016). A fractional model of fluid flow through porous media with mean capillary pressure. *Journal of the Association of Arab Universities for Basic and Applied Sciences*, 21, 59–63. <https://doi.org/10.1016/j.jaubas.2015.01.002>
- Corzo, D., Tostado-Blázquez, G., & Baran, D. (2020). Flexible Electronics: Status, Challenges and Opportunities. *Frontiers in Electronics*, 1, 2. <https://doi.org/10.3389/felec.2020.594003>
- Crystalline and Amorphous Solids: Explanation, Differences*. (2021). <https://dlpng.com/png/7056595>
- Del-Castillo-Negrete, D. (2006). Fractional diffusion models of nonlocal transport. *Physics of Plasmas*, 13(8), 082308. <https://doi.org/10.1063/1.2336114>
- Dev Dhar Dwivedi, A., Kumar Jain, S., Dhar Dwivedi, R., & Dadhich, S. (2020). Numerical Simulation and Compact Modeling of Thin Film Transistors for Future Flexible Electronics. In *Hybrid Nanomaterials - Flexible Electronics Materials*. IntechOpen. <https://doi.org/10.5772/intechopen.90301>
- Dimitrakopoulos, C. D., & Malenfant, P. R. L. (2002). Organic Thin Film Transistors for Large Area Electronics. *Advanced Materials*, 14(2), 99–117. [https://doi.org/10.1002/1521-4095\(20020116\)14:2<99::AID-ADMA99>3.0.CO;2-9](https://doi.org/10.1002/1521-4095(20020116)14:2<99::AID-ADMA99>3.0.CO;2-9)
- Dimitrakopoulos, C. D., & Mascaro, D. J. (2001). Organic thin-film transistors: A review of recent advances. *IBM Journal of Research and Development*, 45(1), 11–27. <https://doi.org/10.1147/rd.451.0011>
- Ding, G., Li, J., & Gao, G. (2015). Band structure engineering of multiple band degeneracy for enhanced thermoelectric power factors in MTe and MSe (M = Pb, Sn, Ge). *RSC Advances*, 5(112), 91974–91978. <https://doi.org/10.1039/c5ra18369c>
- Drude, P. (1900). Zur Elektronentheorie der Metalle; II. Teil. Galvanomagnetische und thermomagnetische Effecte. *Annalen Der Physik*, 308(11), 369–402. <https://doi.org/10.1002/andp.19003081102>
- Duhamel, J. M. C. (1837). Some memoire sur les phenomenes thermo-mechanique. *J. Ecole Polytech*, 15(25), 1–57. <https://www.scopus.com/record/display.uri?eid=2-s2.0-0041169154&origin=inward>

- Dumke, W. P. (1956). Deformation potential theory for n-type Ge. *Physical Review*, 101(2), 531–536. <https://doi.org/10.1103/PhysRev.101.531>
- Dwivedi, A. D. D., Jain, S. K., Dwivedi, R. D., & Dadhich, S. (2019). Numerical simulation and compact modeling of low voltage pentacene based OTFTs. *Journal of Science: Advanced Materials and Devices*, 4(4), 561–567. <https://doi.org/10.1016/j.jsamd.2019.10.006>
- Ebisawa, F., Kurokawa, T., & Nara, S. (1983). Electrical properties of polyacetylene/polysiloxane interface. *Journal of Applied Physics*, 54(6), 3255–3259. <https://doi.org/10.1063/1.332488>
- El-Amin, M. F. (2021). Derivation of fractional-derivative models of multiphase fluid flows in porous media. *Journal of King Saud University - Science*, 33(2), 101346. <https://doi.org/10.1016/j.jksus.2021.101346>
- Ela, A. H. A. El, & Afifi, H. H. (1979). Hopping transport in organic semiconductor system. *Journal of Physics and Chemistry of Solids*, 40(4), 257–259. [https://doi.org/10.1016/0022-3697\(79\)90100-8](https://doi.org/10.1016/0022-3697(79)90100-8)
- Erker, S., & Hofmann, O. T. (2019). Fractional and integer charge transfer at semiconductor/organic interfaces: The role of hybridization and metallicity. *Journal of Physical Chemistry Letters*, 10(4), 848–854. <https://doi.org/10.1021/acs.jpclett.8b03857>
- Evans, L. C. (2010). *Partial differential equations* (2nd ed.). American Mathematical Society.
- Even, J., Pedesseau, L., Tea, E., Almosni, S., Rolland, A., Robert, C., Jancu, J. M., Cornet, C., Katan, C., Guillemoles, J. F., & Durand, O. (2014). Density functional theory simulations of semiconductors for photovoltaic applications: Hybrid organic-inorganic perovskites and III/V heterostructures. *International Journal of Photoenergy*, 2014. <https://doi.org/10.1155/2014/649408>
- Fadlallah, M., Billiot, G., Eccleston, W., & Barclay, D. (2007). DC/AC unified OTFT compact modeling and circuit design for RFID applications. *Solid-State Electronics*, 51(7), 1047–1051. <https://doi.org/10.1016/j.sse.2007.05.018>
- Farmago, I., Shmigelskyi, P., Spiewak, P., & Ciupinski, L. (2011, February 23). Evaluation of computational complexity of finite element analysis. *2011 11th International Conference The Experience of Designing and Application of CAD Systems in Microelectronics (CADSM)*. <https://ieeexplore.ieee.org/document/5744437>
- Feng, X., Huang, Y., & Rosakis, A. J. (2007). On the stoney formula for a thin film/substrate system with nonuniform substrate thickness. *Journal of Applied Mechanics, Transactions ASME*, 74(6), 1276–1281. <https://doi.org/10.1115/1.2745392>
- Fischetti, M. V., & Laux, S. E. (1996). Band structure, deformation potentials, and carrier mobility in strained Si Ge, and SiGe alloys. *Journal of Applied Physics*, 80(4), 2234–2252. <https://doi.org/10.1063/1.363052>

- Forgerini, F. L., & Marchiori, R. (2014). A brief review of mathematical models of thin film growth and surfaces. A possible route to avoid defects in stents<sup>1</sup>. Forgerini FL, Marchiori R. A brief review of mathematical models of thin film growth and surfaces. A possible route to avoid defects in s. In *Biomatter* (Vol. 4, p. e28871). <https://doi.org/10.4161/biom.28871>
- Francisco Gómez-Aguilar, J., Yépez-Martínez, H., Calderón-Ramón, C., Cruz-Orduña, I., Fabricio Escobar-Jiménez, R., Olivares-Peregrino, V. H., Machado, J. A. T., & Lopes, A. M. (2015). Modeling of a Mass-Spring-Damper System by Fractional Derivatives with and without a Singular Kernel. *Entropy*, 17, 6289–6303. <https://doi.org/10.3390/e17096289>
- Fukuda, K., Hikichi, K., Sekine, T., Takeda, Y., Minamiki, T., Kumaki, D., & Tokito, S. (2013). Strain sensitivity and durability in p-type and n-type organic thin-film transistors with printed silver electrodes. *Scientific Reports*, 3(1), 1–6. <https://doi.org/10.1038/srep02048>
- Garnier, F., Horowitz, G., Peng, X., & Fichou, D. (1990). An all-organic “soft” thin film transistor with very high carrier mobility. *Advanced Materials*, 2(12), 592–594. <https://doi.org/10.1002/adma.19900021207>
- Gartland, E. (1993). On the uniform convergence of the Scharfetter-Gummel discretization in one dimension. *SIAM Journal on Numerical Analysis*, 30(3), 749–758. <https://doi.org/10.1137/0730037>
- Giannini, S., Carof, A., & Blumberger, J. (2018). Crossover from Hopping to Band-Like Charge Transport in an Organic Semiconductor Model: Atomistic Nonadiabatic Molecular Dynamics Simulation. *Journal of Physical Chemistry Letters*, 9(11), 3116–3123. <https://doi.org/10.1021/acs.jpcclett.8b01112>
- Gill, W. D. (1972). Drift mobilities in amorphous charge-transfer complexes of trinitrofluorenone and poly-n-vinylcarbazole. *Journal of Applied Physics*, 43(12), 5033–5040. <https://doi.org/10.1063/1.1661065>
- Giustino, F. (2014). Materials Modelling using Density Functional Theory: Properties and Predictions. In *Journal of Chemical Information and Modeling* (Vol. 53).
- Grünewald, M., Thomas, P., & Würtz, D. (1980). A Simple Scheme for Evaluating Field Effect Data. *Physica Status Solidi (B)*, 100(2), K139–K143. <https://doi.org/10.1002/pssb.2221000253>
- Gunda, M., Kumar, P., & Katiyar, M. (2017). Review of Mechanical Characterization Techniques for Thin Films Used in Flexible Electronics. In *Critical Reviews in Solid State and Materials Sciences* (Vol. 42, Issue 2, pp. 129–152). Taylor and Francis Inc. <https://doi.org/10.1080/10408436.2016.1186006>
- Gupta, D., Jeon, N., & Yoo, S. (2008). Modeling the electrical characteristics of TIPS-pentacene thin-film transistors: Effect of contact barrier, field-dependent mobility, and traps. *Organic Electronics*, 9(6), 1026–1031. <https://doi.org/10.1016/j.orgel.2008.08.005>

- Gupta, D., Katiyar, M., & Gupta, D. (2009). An analysis of the difference in behavior of top and bottom contact organic thin film transistors using device simulation. *Organic Electronics*, 10(5), 775–784. <https://doi.org/10.1016/j.orgel.2009.03.012>
- Hamilton, M. C., Martin, S., & Kanicki, J. (2004). Field-effect mobility of organic polymer thin-film transistors. *Chemistry of Materials*, 16(23), 4699–4704. <https://doi.org/10.1021/cm049613r>
- Han, Y., Koganemaru, M., Ikeda, T., Miyazaki, N., Choi, W., & Tomokage, H. (2010). Impacts of uniaxial mechanical stress on high frequency performance of MOSFETs. *Electronics System Integration Technology Conference, ESTC 2010 - Proceedings*. <https://doi.org/10.1109/ESTC.2010.5642994>
- Harris, K. D., Elias, A. L., & Chung, H. J. (2016). Flexible electronics under strain: a review of mechanical characterization and durability enhancement strategies. In *Journal of Materials Science* (Vol. 51, Issue 6, pp. 2771–2805). Springer New York LLC. <https://doi.org/10.1007/s10853-015-9643-3>
- Harrison, W. A. (2004). Elementary Electronic Structure. In *Elementary Electronic Structure*. <https://doi.org/10.1142/5432>
- Haubold, H. J., Mathai, A. M., & Saxena, R. K. (2011). Mittag-leffler functions and their applications. In *Journal of Applied Mathematics* (Vol. 2011). <https://doi.org/10.1155/2011/298628>
- Heidari, H., Navaraj, W. T., Toldi, G., & Dahiya, R. (2016). Device modelling of bendable MOS transistors. *Proceedings - IEEE International Symposium on Circuits and Systems, 2016-July*, 1358–1361. <https://doi.org/10.1109/ISCAS.2016.7527501>
- Heidari, H., Wacker, N., & Dahiya, R. (2017). Bending induced electrical response variations in ultra-thin flexible chips and device modeling. *Cite as: Appl. Phys. Rev*, 4, 31101. <https://doi.org/10.1063/1.4991532>
- Herring, C., & Vogt, E. (1956). Transport and deformation-potential theory for many-valley semiconductors with anisotropic scattering. *Physical Review*, 101(3), 944–961. <https://doi.org/10.1103/PhysRev.101.944>
- Hesam, P., Irfanoglu, A., & Hacker, T. J. (2019). A Method to Estimate Effective Viscous Damping Ratio and Restoring Force From the Dynamic Response Data of Structures. *Frontiers in Built Environment*, 5, 19. <https://doi.org/10.3389/fbuilt.2019.00019>
- Horowitz, G. (1998). Organic Field-Effect Transistors. *Advanced Materials*, 10(5), 365–377. [https://doi.org/10.1002/\(SICI\)1521-4095\(199803\)10:5<365::AID-ADMA365>3.0.CO;2-U](https://doi.org/10.1002/(SICI)1521-4095(199803)10:5<365::AID-ADMA365>3.0.CO;2-U)
- Horowitz, G. (2004). Organic thin film transistors: From theory to real devices. *Journal of Materials Research*, 19(7), 1946–1962. <https://doi.org/10.1557/JMR.2004.0266>

- Horowitz, G. (2009). *Interfaces in Organic Field-Effect Transistors* (pp. 113–153). Springer, Berlin, Heidelberg. [https://doi.org/10.1007/12\\_2009\\_7](https://doi.org/10.1007/12_2009_7)
- Hu, G., Orkoulas, G., & Christofides, P. D. (2009). Stochastic modeling of film porosity in thin film deposition. *Proceedings of the American Control Conference*, 4771–4778. <https://doi.org/10.1109/ACC.2009.5160138>
- Huang, H., Qian, Z., & Yang, J. (2019). I-V characteristics of a piezoelectric semiconductor nanofiber under local tensile/compressive stress. *Journal of Applied Physics*, 126(16), 164902. <https://doi.org/10.1063/1.5110876>
- Humbare, R., Wankhede, S., & Kumar, V. (2020). *Flexible Electronics Market Size, Share & Growth / Analysis - 2027*. <https://www.alliedmarketresearch.com/flexible-electronics-market>
- Hur, T. B., Hwang, Y. H., Kim, H. K., & Lee, I. J. (2006). Strain effects in ZnO thin films and nanoparticles. *Journal of Applied Physics*, 99(6), 064308. <https://doi.org/10.1063/1.2183391>
- Ishii, H., Inoue, J. I., Kobayashi, N., & Hirose, K. (2018). Quantitative mobility evaluation of organic semiconductors using quantum dynamics based on density functional theory. *Physical Review B*, 98(23), 235422. <https://doi.org/10.1103/PhysRevB.98.235422>
- Iyiola, O. S., & Zaman, F. D. (2014). A fractional diffusion equation model for cancer tumor. *AIP Advances*, 4(10), 107121. <https://doi.org/10.1063/1.4898331>
- Janotti, A., & Van De Walle, C. G. (2007). Absolute deformation potentials and band alignment of wurtzite ZnO, MgO, and CdO. *Physical Review B - Condensed Matter and Materials Physics*, 75(12), 121201. <https://doi.org/10.1103/PhysRevB.75.121201>
- Janotti, A., & Van De Walle, C. G. (2009). Fundamentals of zinc oxide as a semiconductor. *Reports on Progress in Physics*, 72(12). <https://doi.org/10.1088/0034-4885/72/12/126501>
- Jayamohan, J., & Mujeeb, A. (2003). Application of photo elasticity for the measurement of internal stresses in indeterminate structures. *2014 1st International Conference on Computational Systems and Communications, ICCSC 2014*, 392–396. <https://doi.org/10.1109/COMPSC.2014.7032685>
- Jensen, J. S. (2003). Phononic band gaps and vibrations in one- and two-dimensional mass-spring structures. *Journal of Sound and Vibration*, 266(5), 1053–1078. [https://doi.org/10.1016/S0022-460X\(02\)01629-2](https://doi.org/10.1016/S0022-460X(02)01629-2)
- Jerome, J. W. (1985). CONSISTENCY OF SEMICONDUCTOR MODELING: AN EXISTENCE/STABILITY ANALYSIS FOR THE STATIONARY VAN ROOSBROECK SYSTEM. *SIAM Journal on Applied Mathematics*, 45(4), 565–590. <https://doi.org/10.1137/0145034>
- Jerome, J. W. (1996). Analysis of Charge Transport. In *Analysis of Charge Transport*. Springer Berlin Heidelberg. <https://doi.org/10.1007/978-3-642-79987-7>



- Jerome, J. W., & Kerkhoven, T. (1991). Finite element approximation theory for the drift diffusion semiconductor model. *SIAM Journal on Numerical Analysis*, 28(2), 403–422. <https://doi.org/10.1137/0728023>
- Jiménez, S., Usero, D., Vázquez, L., & Velasco, M. (2017). Fractional Diffusion Models for the Atmosphere of Mars. *Fractal and Fractional*, 2(1), 1. <https://doi.org/10.3390/fractalfract2010001>
- Kalb, W. L., & Batlogg, B. (2010). Calculating the trap density of states in organic field-effect transistors from experiment: A comparison of different methods. *Physical Review B - Condensed Matter and Materials Physics*, 81(3), 035327. <https://doi.org/10.1103/PhysRevB.81.035327>
- Kaltenbrunner, M., Sekitani, T., Reeder, J., Yokota, T., Kuribara, K., Tokuhara, T., Drack, M., Schwödiauer, R., Graz, I., Bauer-Gogonea, S., Bauer, S., & Someya, T. (2013). An ultra-lightweight design for imperceptible plastic electronics. *Nature*, 499(7459), 458–463. <https://doi.org/10.1038/nature12314>
- Kandel, E. R., Schwartz, J. H., Jessell, T. M., Siegelbaum, S. A., & Hudspeth, A. J. (2013). *Principles of Neural Science* (5 ed.). McGraw-Hill Education.
- Kaushik, B. K., Brijesh Kumar, Prajapati, S., & Mittal, P. (2016). *Organic Thin-Film Transistor Applications : Materials to Circuits* (1st ed., Vol. 1). CRC Press.
- Kerkhoven, T. (1988). On the Effectiveness of Gummel’s Method. *SIAM Journal on Scientific and Statistical Computing*, 9(1), 48–60. <https://doi.org/10.1137/0909005>
- Khatyr, F., Imberdis, C., Vescovo, P., Varchon, D., & Lagarde, J. M. (2004). Model of the viscoelastic behaviour of skin in vivo and study of anisotropy. *Skin Research and Technology*, 10(2), 96–103. <https://doi.org/10.1111/j.1600-0846.2004.00057.x>
- Klepach, D., & Zohdi, T. I. (2014). Strain assisted diffusion: Modeling and simulation of deformation-dependent diffusion in composite media. *Composites Part B: Engineering*, 56, 413–423. <https://doi.org/10.1016/j.compositesb.2013.08.035>
- Kniepert, J., Schubert, M., Blakesley, J. C., & Neher, D. (2011). Photogeneration and recombination in P3HT/PCBM solar cells probed by time-delayed collection field experiments. *Journal of Physical Chemistry Letters*, 2(7), 700–705. <https://doi.org/10.1021/jz200155b>
- Kohanoff, J. (2006). Electronic structure calculations for solids and molecules: Theory and computational methods. In *Electronic Structure Calculations for Solids and Molecules: Theory and Computational Methods* (Vol. 9780521815918). <https://doi.org/10.1017/CBO9780511755613>

- Kovalchuk, M. V., Kazimirov, A. Y., & Zheludeva, S. I. (1995). Surface-sensitive X-ray diffraction methods: physics, applications and related X-ray and SR instrumentation. *Nuclear Inst. and Methods in Physics Research, B*, 101(4), 435–452. [https://doi.org/10.1016/0168-583X\(95\)00377-0](https://doi.org/10.1016/0168-583X(95)00377-0)
- Kyndiah, A., Leonardi, F., Tarantino, C., Cramer, T., Millan-Solsona, R., Garreta, E., Montserrat, N., Mas-Torrent, M., & Gomila, G. (2020). Bioelectronic Recordings of Cardiomyocytes with Accumulation Mode Electrolyte Gated Organic Field Effect Transistors. *Biosensors and Bioelectronics*, 150. <https://doi.org/10.1016/j.bios.2019.111844>
- Lee, A. Y., Song, J. K., Oh, H. R., Kim, H. A., Kim, S. Y., Kwon, A. R., Park, E. S., Lim, C. H., Eckert, J., & Lee, M. H. (2017). Strain dependence of diffusion in Zr-based bulk amorphous alloy. *Journal of Applied Physics*, 122(24), 245105. <https://doi.org/10.1063/1.5001112>
- Lee, H., Choi, T. K., Lee, Y. B., Cho, H. R., Ghaffari, R., Wang, L., Choi, H. J., Chung, T. D., Lu, N., Hyeon, T., Choi, S. H., & Kim, D. H. (2016). A graphene-based electrochemical device with thermoresponsive microneedles for diabetes monitoring and therapy. *Nature Nanotechnology*. <https://doi.org/10.1038/nnano.2016.38>
- Lee, M. H., Hsieh, B. F., & Chang, S. T. (2013). Electrical properties correlated with redistributed deep states in a-Si:H thin-film transistors on flexible substrates undergoing mechanical bending. *Thin Solid Films*, 528, 82–85. <https://doi.org/10.1016/j.tsf.2012.10.097>
- Lee, Y. C., Liu, T. S., Wu, C. I., & Lin, W. Y. (2012). Investigation on residual stress and stress-optical coefficient for flexible electronics by photoelasticity. *Measurement: Journal of the International Measurement Confederation*, 45(3), 311–316. <https://doi.org/10.1016/j.measurement.2011.11.017>
- Lejaeghere, K., Bihlmayer, G., Björkman, T., Blaha, P., Blügel, S., Blum, V., Caliste, D., Castelli, I. E., Clark, S. J., Dal Corso, A., De Gironcoli, S., Deutsch, T., Dewhurst, J. K., Di Marco, I., Draxl, C., Dułak, M., Eriksson, O., Flores-Livas, J. A., Garrity, K. F., ... Cottenier, S. (2016). Reproducibility in density functional theory calculations of solids. *Science*, 351(6280). <https://doi.org/10.1126/science.aad3000>
- Li, C., Qian, D., & Chen, Y. (2011). On Riemann-Liouville and Caputo derivatives. *Discrete Dynamics in Nature and Society*, 2011. <https://doi.org/10.1155/2011/562494>
- Li, H., Shi, W., Song, J., Jang, H. J., Dailey, J., Yu, J., & Katz, H. E. (2019). Chemical and Biomolecule Sensing with Organic Field-Effect Transistors. In *Chemical Reviews* (Vol. 119, Issue 1, pp. 3–35). American Chemical Society. <https://doi.org/10.1021/acs.chemrev.8b00016>
- Li, L., Marien, H., Genoe, J., Steyaert, M., & Heremans, P. (2010). Compact model for organic thin-film transistor. *IEEE Electron Device Letters*, 31(3), 210–212. <https://doi.org/10.1109/LED.2009.2039744>

- Li, S. S. (2007). Scattering Mechanisms and Carrier Mobilities in Semiconductors. In *Semiconductor Physical Electronics* (pp. 211–245). Springer New York.  
[https://doi.org/10.1007/0-387-37766-2\\_8](https://doi.org/10.1007/0-387-37766-2_8)
- Li, Y. (2007). A two-dimensional thin-film transistor simulation using adaptive computing technique. *Applied Mathematics and Computation*, 184(1 SPEC. ISS.), 73–85.  
<https://doi.org/10.1016/j.amc.2005.12.073>
- Lim, J. S., Thompson, S. E., & Fossum, J. G. (2004). Comparison of threshold-voltage shifts for uniaxial and biaxial tensile-stressed n-MOSFETs. *IEEE Electron Device Letters*, 25(11), 731–733. <https://doi.org/10.1109/LED.2004.837581>
- Lin, Y. Y., Gundlach, D. J., Nelson, S. F., & Jackson, T. N. (1997). Pentacene-based organic thin-film transistors. *IEEE Transactions on Electron Devices*, 44(8), 1325–1331.  
<https://doi.org/10.1109/16.605476>
- Liu, C., Huang, K., Park, W. T., Li, M., Yang, T., Liu, X., Liang, L., Minari, T., & Noh, Y. Y. (2017). A unified understanding of charge transport in organic semiconductors: The importance of attenuated delocalization for the carriers. *Materials Horizons*, 4(4), 608–618.  
<https://doi.org/10.1039/c7mh00091j>
- Locci, S., Morana, M., Orgiu, E., Bonfiglio, A., & Lugli, P. (2008). Modeling of short-channel effects in organic thin-film transistors. *IEEE Transactions on Electron Devices*, 55(10), 2561–2567. <https://doi.org/10.1109/TED.2008.2003022>
- Lomov, A. A., Bushuev, V. A., & Karavanskii, V. A. (2000). Study of surface and interface roughnesses in porous silicon by high-resolution x-ray methods. *Crystallography Reports*, 45(5), 842–847. <https://doi.org/10.1134/1.1312933>
- Lu, B., & Zhou, Y. C. (2011). Poisson-Nernst-Planck equations for simulating biomolecular diffusion-reaction processes II: Size effects on ionic distributions and diffusion-reaction rates. *Biophysical Journal*, 100(10), 2475–2485. <https://doi.org/10.1016/j.bpj.2011.03.059>
- Lynch, C. S. (1995). Strain compensated thin film stress gauges for stress wave measurements in the presence of lateral strain. *Review of Scientific Instruments*, 66(12), 5582–5589.  
<https://doi.org/10.1063/1.1146024>
- Machado, J. A. T., & Kiryakova, V. (2017). The Chronicles of Fractional Calculus. In *Fractional Calculus and Applied Analysis* (Vol. 20, Issue 2). <https://doi.org/10.1515/fca-2017-0017>
- Macias, M., & Sierociuk, D. (2013). Modeling of electrical drive system with flexible shaft based on fractional calculus. *Proceedings of the 2013 14th International Carpathian Control Conference, ICC 2013*, 222–227.  
<https://doi.org/10.1109/CarpathianCC.2013.6560542>
- Magin, R. L. (2006). *Fractional calculus in bioengineering*. Begell House Publishers.

- Magin, R. L. (2010). Fractional calculus models of complex dynamics in biological tissues. *Computers and Mathematics with Applications*, 59(5), 1586–1593. <https://doi.org/10.1016/j.camwa.2009.08.039>
- Maiti, T. K., Hayashi, T., Chen, L., Mori, H., Kang, M. J., Takimiya, K., Miura-Mattausch, M., & Mattausch, H. J. (2014). A surface potential based organic thin-film transistor model for circuit simulation verified with DNTT high performance test devices. *IEEE Transactions on Semiconductor Manufacturing*, 27(2), 159–168. <https://doi.org/10.1109/TSM.2014.2304736>
- Maldon, B., & Thamwattana, N. (2020). A Fractional Diffusion Model for Dye-Sensitized Solar Cells. *Molecules*, 25(13), 2966. <https://doi.org/10.3390/molecules25132966>
- Manasevit, H. M., Gergis, I. S., & Jones, A. B. (1982). Electron mobility enhancement in epitaxial multilayer Si-Si 1-xGex alloy films on (100) Si. *Applied Physics Letters*, 41(5), 464–466. <https://doi.org/10.1063/1.93533>
- Martynyuk, V., & Ortigueira, M. (2015). Fractional model of an electrochemical capacitor. *Signal Processing*, 107, 355–360. <https://doi.org/10.1016/j.sigpro.2014.02.021>
- Mason, W. P., & Thurston, R. N. (1957). Use of Piezoresistive Materials in the Measurement of Displacement, Force, and Torque. *Journal of the Acoustical Society of America*, 29(10), 1096–1101. <https://doi.org/10.1121/1.1908710>
- Meer, P. R. van der., Staveren, A. van, & Roermund, A. H. M. van. (2004). *Low-power deep sub-micron CMOS logic : sub-threshold current reduction*. Kluwer Academic.
- Meixner, R. M., Göbel, H. H., Qiu, H., Ucurum, C., Klix, W., Stenzel, R., Yildirim, F. A., Bauhofer, W., & Krautschneider, W. H. (2008). A physical-based PSPICE compact model for poly(3-hexylthiophene) organic field-effect transistors. *IEEE Transactions on Electron Devices*, 55(7), 1776–1781. <https://doi.org/10.1109/TED.2008.925339>
- Mitkowski, W., & Skruch, P. (2013). Fractional-order models of the supercapacitors in the form of RC ladder networks. *Bulletin of the Polish Academy of Sciences: Technical Sciences*, 61(3), 581–587. <https://doi.org/10.2478/bpasts-2013-0059>
- Moin, P. (2010). *Fundamentals of engineering numerical analysis* (2nd ed.). Cambridge University Press.
- Mozar, A. J., Dennler, G., Sariciftci, N. S., Westerling, M., Pivrikas, A., Asterbacka, R., & Juka, G. (2005). Time-dependent mobility and recombination of the photoinduced charge carriers in conjugated polymer/fullerene bulk heterojunction solar cells. *Physical Review B - Condensed Matter and Materials Physics*, 72(3), 035217. <https://doi.org/10.1103/PhysRevB.72.035217>
- Mulliken, R. S. (1950). Overlap Integrals and Chemical Binding. *Journal of the American Chemical Society*, 72(10), 4493–4503. <https://doi.org/10.1021/ja01166a045>

- Muntasir, T., & Chaudhary, S. (2015). Understanding defect distributions in polythiophenes via comparison of regioregular and regiorandom species. *Journal of Applied Physics*, 118(20), 205504. <https://doi.org/10.1063/1.4936326>
- Nan, C. (2013). *Numerical Modeling of Flexible ZnO Thin-Film Transistors Using COMSOL Multiphysics* [University of Waterloo]. <http://hdl.handle.net/10012/7660>
- Nawrocki, R. A. (2019). Super- and Ultrathin Organic Field-Effect Transistors: from Flexibility to Super- and Ultraflexibility. *Advanced Functional Materials*, 29(51), 1906908. <https://doi.org/10.1002/adfm.201906908>
- Nawrocki, R. A., Jin, H., Lee, S., Yokota, T., Sekino, M., & Someya, T. (2018). Self-Adhesive and Ultra-Conformable, Sub-300 nm Dry Thin-Film Electrodes for Surface Monitoring of Biopotentials. *Advanced Functional Materials*, 28(36). <https://doi.org/10.1002/adfm.201803279>
- Nawrocki, R. A., Matsuhisa, N., Yokota, T., & Someya, T. (2016). 300-nm Imperceptible, Ultraflexible, and Biocompatible e-Skin Fit with Tactile Sensors and Organic Transistors. *Advanced Electronic Materials*, 2(4), 1500452. <https://doi.org/10.1002/aelm.201500452>
- Necliudov, P. V., Shur, M. S., Gundlach, D. J., & Jackson, T. N. (2000). Modeling of organic thin film transistors of different designs. *Journal of Applied Physics*, 88(11), 6594–6597. <https://doi.org/10.1063/1.1323534>
- Ni, D., & Christofides, P. D. (2005). Multivariable Predictive Control of Thin Film Deposition Using a Stochastic PDE Model. *Industrial & Engineering Chemistry Research*, 44(8), 2416–2427. <https://doi.org/10.1021/ie0490511>
- Noyan, I. C., Cohen, J. B., Noyan, I. C., & Cohen, J. B. (1987a). Determination of Strain and Stress Fields by Diffraction Methods. In *Residual Stress* (pp. 117–163). Springer New York. [https://doi.org/10.1007/978-1-4613-9570-6\\_5](https://doi.org/10.1007/978-1-4613-9570-6_5)
- Noyan, I. C., Cohen, J. B., Noyan, I. C., & Cohen, J. B. (1987b). Fundamental Concepts in X-ray Diffraction. In *Residual Stress* (pp. 75–116). Springer New York. [https://doi.org/10.1007/978-1-4613-9570-6\\_4](https://doi.org/10.1007/978-1-4613-9570-6_4)
- Oba, F., & Kumagai, Y. (2018). Design and exploration of semiconductors from first principles: A review of recent advances. In *Applied Physics Express* (Vol. 11, Issue 6, p. 060101). Japan Society of Applied Physics. <https://doi.org/10.7567/APEX.11.060101>
- Oh, J., Kim, J. H., Lee, S. Y., Kim, M. S., Kim, J. M., Park, K., & Kim, Y. S. (2018). Bending Performance of Flexible Organic Thin-Film Transistors With/Without Encapsulation Layer. *IEEE Transactions on Device and Materials Reliability*, 18(1), 1–4. <https://doi.org/10.1109/TDMR.2017.2780267>

- Ojha, A., Chauhan, Y. S., & Mohapatra, N. R. (2016). A channel stress-profile-based compact model for threshold voltage prediction of uniaxial strained HKMG nMOS transistors. *IEEE Journal of the Electron Devices Society*, 4(2), 42–49. <https://doi.org/10.1109/JEDS.2016.2524536>
- Orenstein, J., & Kastner, M. (1981). Photocurrent transient spectroscopy: Measurement of the density of localized states in a -As<sub>2</sub>Se<sub>3</sub>. *Physical Review Letters*, 46(21), 1421–1424. <https://doi.org/10.1103/PhysRevLett.46.1421>
- Pawlaczyk, M., Lelonkiewicz, M., & Wieczorowski, M. (2013). Age-dependent biomechanical properties of the skin. In *Postepy Dermatologii i Alergologii* (Vol. 30, Issue 5, pp. 302–306). <https://doi.org/10.5114/pdia.2013.38359>
- People, R., Bean, J. C., Lang, D. V., Sergeant, A. M., Störmer, H. L., Wecht, K. W., Lynch, R. T., & Baldwin, K. (1984). Modulation doping in GexSi<sub>1-x</sub>/Si strained layer heterostructures. *Applied Physics Letters*, 45(11), 1231–1233. <https://doi.org/10.1063/1.95074>
- Perumal, C., Ishida, K., Shabanpour, R., Boroujeni, B. K., Petti, L., Munzenrieder, N. S., Salvatore, G. A., Carta, C., Troster, G., & Ellinger, F. (2013). A compact a-IGZO TFT model based on MOSFET SPICE Level=3 template for Analog/RF circuit designs. *IEEE Electron Device Letters*, 34(11), 1391–1393. <https://doi.org/10.1109/LED.2013.2279940>
- Pierret, R. F. (1996). Semiconductor Device Fundamentals. In *New York*. Addison-Wesley. <https://doi.org/10.1007/BF00198606>
- Pikus, G. L., & Bir, G. E. (1974). Symmetry and strain-induced effects in semiconductors. In *Materials Research*.
- Podlubny, I. (1999). *Fractional differential equations : an introduction to fractional derivatives, fractional differential equations, to methods of their solution and some of their applications*. Academic Press.
- Pods, J., Schönke, J., & Bastian, P. (2013). Electrodiffusion models of neurons and extracellular space using the poisson-nernst-planck equations - Numerical simulation of the intra- and extracellular potential for an axon model. *Biophysical Journal*, 105(1), 242–254. <https://doi.org/10.1016/j.bpj.2013.05.041>
- Polyanin, A. D., & Nazaikinskii, V. E. (2016). *Handbook of linear partial differential equations for engineers and scientists* (2nd ed.). Chapman and Hall/CRC.
- Prasad, R., Kothari, K., & Mehta, U. (2019). Flexible fractional supercapacitor model analyzed in time domain. *IEEE Access*, 7, 122626–122633. <https://doi.org/10.1109/ACCESS.2019.2938543>
- Quintana, J. J., Ramos, A., & Nuez, I. (2006). Identification of the fractional impedance of ultracapacitors. *IFAC Proceedings Volumes (IFAC-PapersOnline)*, 2(PART 1), 432–436. <https://doi.org/10.3182/20060719-3-pt-4902.00073>

- Quintero, S. M. M., Quirino, W. G., Triques, A. L. C., Valente, L. C. G., Braga, A. M. B., Achete, C. A., & Cremona, M. (2006). Thin film stress measurement by fiber optic strain gage. *Thin Solid Films*, 494(1–2), 141–145. <https://doi.org/10.1016/j.tsf.2005.08.215>
- Roache, P. J. (2002). Code verification by the method of manufactured solutions. *Journal of Fluids Engineering, Transactions of the ASME*, 124(1), 4–10. <https://doi.org/10.1115/1.1436090>
- Rogalski, M. S., & Palmer, S. B. (2014). Solid state physics. In *Solid State Physics*. <https://doi.org/10.1201/9781482283037>
- Rogers, J. A., Bao, Z., Baldwin, K., Dodabalapur, A., Crone, B., Raju, V. R., Kuck, V., Katz, H., Amundson, K., Ewing, J., & Drzaic, P. (2001). Paper-like electronic displays: Large-area rubber-stamped plastic sheets of electronics and microencapsulated electrophoretic inks. *Proceedings of the National Academy of Sciences of the United States of America*, 98(9), 4835–4840. <https://doi.org/10.1073/pnas.091588098>
- Root, S. E., Savagatrup, S., Printz, A. D., Rodriguez, D., & Lipomi, D. J. (2017). Mechanical Properties of Organic Semiconductors for Stretchable, Highly Flexible, and Mechanically Robust Electronics. In *Chemical Reviews* (Vol. 117, Issue 9, pp. 6467–6499). American Chemical Society. <https://doi.org/10.1021/acs.chemrev.7b00003>
- Rowe, J. E., Cardona, M., & Pollak, F. H. (1968). Valence band symmetry and deformation potentials of ZnO. *Solid State Communications*, 6(4), 239–242. [https://doi.org/10.1016/0038-1098\(68\)90043-4](https://doi.org/10.1016/0038-1098(68)90043-4)
- Ruedenbebg, K., O-Ohata, K., & Wilson, D. G. (1966). Overlap integrals between atomic orbitals. *Journal of Mathematical Physics*, 7(3), 539–546. <https://doi.org/10.1063/1.1704964>
- Sakrajda, P., & Sławomir Wiraszka, M. (2018). Fractional-Order Diffusion Model for Social Networks. *SSRN Electronic Journal*. <https://doi.org/10.2139/ssrn.3271330>
- Scher, H., & Montroll, E. W. (1975). Anomalous transit-time dispersion in amorphous solids. *Physical Review B*, 12(6), 2455–2477. <https://doi.org/10.1103/PhysRevB.12.2455>
- Schischke, K., Nissen, N. F., & Schneider-Ramelow, M. (2020). Flexible, stretchable, conformal electronics, and smart textiles: Environmental life cycle considerations for emerging applications. In *MRS Communications* (Vol. 10, Issue 1, pp. 69–82). Cambridge University Press. <https://doi.org/10.1557/mrc.2019.157>
- Sedra, A. S., & Smith, K. C. (2015). *Microelectronic circuits*. (7th ed.). Oxford University Press. [http://unisabana22.gsl.com.mx:80/F?func=service&doc\\_library=CNA01&local\\_base=CNA01&doc\\_number=000268486&sequence=000001&line\\_number=0001&func\\_code=DB\\_RECORDS&service\\_type=MEDIA](http://unisabana22.gsl.com.mx:80/F?func=service&doc_library=CNA01&local_base=CNA01&doc_number=000268486&sequence=000001&line_number=0001&func_code=DB_RECORDS&service_type=MEDIA)
- Sheu, Y.-M. (2007). *Layout Dependent Effect on Advanced MOSFETs* [National Chiao-Tung University]. <https://ir.nctu.edu.tw/bitstream/11536/76857/1/180701.pdf>

- Shichman, H., & Hodges, D. A. (1968). Modeling and Simulation of Insulated-Gate Field-Effect Transistor Switching Circuits. *IEEE Journal of Solid-State Circuits*, 3(3), 285–289. <https://doi.org/10.1109/JSSC.1968.1049902>
- Shim, C. H., Maruoka, F., & Hattori, R. (2010). Structural analysis on organic thin-film transistor with device simulation. *IEEE Transactions on Electron Devices*, 57(1), 195–200. <https://doi.org/10.1109/TED.2009.2035540>
- Shin, H., Tasch, A. F., Maziar, C. M., & Banerjee, S. K. (1989). A New Approach to Verify and Derive a Transverse-Field-Dependent Mobility Model for Electrons in MOS Inversion Layers. *IEEE Transactions on Electron Devices*, 36(6), 1117–1124. <https://doi.org/10.1109/16.24356>
- Shuai, Z., Wang, L., & Song, C. (2012). *Deformation Potential Theory* (pp. 67–88). Springer, Berlin, Heidelberg. [https://doi.org/10.1007/978-3-642-25076-7\\_4](https://doi.org/10.1007/978-3-642-25076-7_4)
- Sibatov, R. T., & Uchaikin, V. V. (2007). Fractional differential kinetics of charge transport in unordered semiconductors. *Semiconductors*, 41(3), 335–340. <https://doi.org/10.1134/S1063782607030177>
- Sibatov, Renat T, & Uchaikin, V. V. (2009). Fractional differential approach to dispersive transport in semiconductors. *Physics-Uspekhi*, 52(10), 1019–1043. <https://doi.org/10.3367/ufne.0179.200910c.1079>
- Siddiqui, J. J. (2012). *Investigation of Electrical Instabilities and Interface Charge in Zinc Oxide Thin-Film Transistors with High-k Dielectrics*. [University of Michigan, Horace H. Rackham School of Graduate Studies]. <http://hdl.handle.net/2027.42/93842>
- Sierociuk, D., Dzielinski, A., Sarwas, G., Petras, I., Podlubny, I., & Skovranek, T. (2013). Modelling heat transfer in heterogeneous media using fractional calculus. *Philosophical Transactions of the Royal Society A: Mathematical, Physical and Engineering Sciences*, 371(1990). <https://doi.org/10.1098/rsta.2012.0146>
- Silvaco International. (2016). *Atlas Users Manual*. <https://dynamic.silvaco.com/dynamicweb/jsp/downloads/DownloadManualsAction.do?req=silen-manuals&nm=atlas>
- Singh, T. B., Sariciftci, N. S., & Grote, J. G. (2009). *Bio-Organic Optoelectronic Devices Using DNA* (pp. 73–112). Springer, Berlin, Heidelberg. [https://doi.org/10.1007/12\\_2009\\_6](https://doi.org/10.1007/12_2009_6)
- Sjöberg, M., & Kari, L. (2002). Non-linear behavior of a rubber isolator system using fractional derivatives. *Vehicle System Dynamics*, 37(3), 217–236. <https://doi.org/10.1076/vesd.37.3.217.3532>
- Smith, C. S. (1954). Piezoresistance effect in germanium and silicon. *Physical Review*, 94(1), 42–49. <https://doi.org/10.1103/PhysRev.94.42>



- Son, D., Lee, J., Qiao, S., Ghaffari, R., Kim, J., Lee, J. E., Song, C., Kim, S. J., Lee, D. J., Jun, S. W., Yang, S., Park, M., Shin, J., Do, K., Lee, M., Kang, K., Hwang, C. S., Lu, N., Hyeon, T., & Kim, D. H. (2014). Multifunctional wearable devices for diagnosis and therapy of movement disorders. *Nature Nanotechnology*, 9, 397–404. <https://doi.org/10.1038/nnano.2014.38>
- Sun, G. (2007). *Strain Effects on Hole Mobility of Silicon and Germanium p-Type Metal-Oxide-Semiconductor Field-Effect-Transistors* [University of Florida]. <http://purl.fcla.edu/fcla/etd/UFE0018960>
- Sun, Y., Thompson, S. E., & Nishida, T. (2007). Physics of strain effects in semiconductors and metal-oxide-semiconductor field-effect transistors. *Journal of Applied Physics*, 101(10), 104503. <https://doi.org/10.1063/1.2730561>
- Sun, Yongke, Thompson, S. E., & Nishida, T. (2010). Strain effect in semiconductors: Theory and device applications. In *Strain Effect in Semiconductors: Theory and Device Applications*. Springer US. <https://doi.org/10.1007/978-1-4419-0552-9>
- Tan, G. L., Yuan, X. L., Zhang, Q. M., Ku, W. H., & Shey, A. J. (1989). Two-Dimensional Semiconductor Device Analysis Based on New Finite-Element Discretization Employing the S-G Scheme. *IEEE Transactions on Computer-Aided Design of Integrated Circuits and Systems*, 8(5), 468–478. <https://doi.org/10.1109/43.24875>
- Thompson, S. E., Armstrong, M., Auth, C., Cea, S., Chau, R., Glass, G., Hoffman, T., Klaus, J., Ma, Z., McIntyre, B., Murthy, A., Obradovic, B., Shifren, L., Sivakumar, S., Tyagi, S., Ghani, T., Mistry, K., Bohr, M., & El-Mansy, Y. (2004). A logic nanotechnology featuring strained-silicon. In *IEEE Electron Device Letters* (Vol. 25, Issue 4, pp. 191–193). <https://doi.org/10.1109/LED.2004.825195>
- Tiedje, T., & Rose, A. (1981). A physical interpretation of dispersive transport in disordered semiconductors. *Solid State Communications*, 37(1), 49–52. [https://doi.org/10.1016/0038-1098\(81\)90886-3](https://doi.org/10.1016/0038-1098(81)90886-3)
- Tsekov, R. (2018). Brownian motion of a classical particle in quantum environment. *Physics Letters, Section A: General, Atomic and Solid State Physics*, 382(33), 2230–2232. <https://doi.org/10.1016/j.physleta.2017.06.037>
- Tserbak, C., Polatoglou, H. M., & Theodorou, G. (1993). Unified approach to the electronic structure of strained Si/Ge superlattices. *Physical Review B*, 47(12), 7104–7124. <https://doi.org/10.1103/PhysRevB.47.7104>
- Upreti, T., Wang, Y., Zhang, H., Scheunemann, D., Gao, F., & Kemerink, M. (2019). Experimentally Validated Hopping-Transport Model for Energetically Disordered Organic Semiconductors. *Physical Review Applied*, 12(6), 064039. <https://doi.org/10.1103/PhysRevApplied.12.064039>

- Valeev, E. F., Coropceanu, V., Da Silva Filho, D. A., Salman, S., & Brédas, J. L. (2006). Effect of electronic polarization on charge-transport parameters in molecular organic semiconductors. *Journal of the American Chemical Society*, 128(30), 9882–9886. <https://doi.org/10.1021/ja061827h>
- Van De Walle, C. G. (1989). Band lineups and deformation potentials in the model-solid theory. *Physical Review B*, 39(3), 1871–1883. <https://doi.org/10.1103/PhysRevB.39.1871>
- Van Roosbroeck, W. (1950). Theory of the Flow of Electrons and Holes in Germanium and Other Semiconductors. *Bell System Technical Journal*, 29(4), 560–607. <https://doi.org/10.1002/j.1538-7305.1950.tb03653.x>
- Vidor, F. F., Meyers, T., & Hilleringmann, U. (2016). Inverter circuits using ZnO nanoparticle based thin-film transistors for flexible electronic applications. *Nanomaterials*, 6(9). <https://doi.org/10.3390/nano6090154>
- Wacker, N., Richter, H., Hassan, M. U., Rempp, H., & Burghartz, J. N. (2011). Compact modeling of CMOS transistors under variable uniaxial stress. *Solid-State Electronics*, 57(1), 52–60. <https://doi.org/10.1016/j.sse.2010.12.003>
- Wang, S., Ha, M., Manno, M., Daniel Frisbie, C., & Leighton, C. (2012). Hopping transport and the Hall effect near the insulator-metal transition in electrochemically gated poly(3-hexylthiophene) transistors. *Nature Communications*, 3(1), 1–7. <https://doi.org/10.1038/ncomms2213>
- Wang, Z., Chen, S., Duan, X., Sun, D., & Gong, X. (2012). Strain induced quantum effect in semiconductors. *Journal of the Physical Society of Japan*, 81(7). <https://doi.org/10.1143/JPSJ.81.074712>
- Weinan, E., & Lu, J. (2014). Mathematical theory of solids: From quantum mechanics to continuum models. *Discrete and Continuous Dynamical Systems- Series A*, 34(12), 5085–5097. <https://doi.org/10.3934/dcds.2014.34.5085>
- Wen, S. H., Li, A., Song, J., Deng, W. Q., Han, K. L., & Goddard, W. A. (2009). First-principles investigation of anisotropic hole mobilities in organic semiconductors. *Journal of Physical Chemistry B*, 113(26), 8813–8819. <https://doi.org/10.1021/jp900512s>
- Wondmagegn, W., & Pieper, R. (2009). Simulation of top-contact pentacene thin film transistor. *Journal of Computational Electronics*, 8(1), 19–24. <https://doi.org/10.1007/s10825-009-0265-3>
- Wong, A. K., Dunn, S. A., & Sparrow, J. G. (1988). Residual stress measurement by means of the thermoelastic effect. *Nature*, 332(6165), 613–615. <https://doi.org/10.1038/332613a0>
- Wu, Yanfei, Chew, A. R., Rojas, G. A., Sini, G., Haugstad, G., Belianinov, A., Kalinin, S. V., Li, H., Risko, C., Brédas, J. L., Salleo, A., & Frisbie, C. D. (2016). Strain effects on the work function of an organic semiconductor. *Nature Communications*, 7(1), 1–9. <https://doi.org/10.1038/ncomms10270>

- Wu, Yixuan, Nan, P., Chen, Z., Zeng, Z., Lin, S., Zhang, X., Dong, H., Chen, Z., Gu, H., Li, W., Chen, Y., Ge, B., & Pei, Y. (2020). Manipulation of Band Degeneracy and Lattice Strain for Extraordinary PbTe Thermoelectrics. *Research*, 2020, 1–12. <https://doi.org/10.34133/2020/8151059>
- Xue, D. (2017). *Fractional-order control systems : fundamentals and numerical implementations*. De Gruyter.
- Yang, S. M., & Tao, W. X. (2006). *Heat Transfer (Chinese version)* (4th ed.). Higher Education Press.
- Yang, Y., Nawrocki, R. A., Voyles, R. M., & Zhang, H. H. (2021a). Modeling of the electrical characteristics of an organic field effect transistor in presence of the bending effects. *Organic Electronics*, 88, 106000. <https://doi.org/10.1016/j.orgel.2020.106000>
- Yang, Y., Nawrocki, R., Voyles, R., & H. Zhang, H. (2020). Modeling of an Internal Stress and Strain Distribution of an Inverted Staggered Thin-Film Transistor Based on Two-Dimensional Mass-Spring-Damper Structure. *Computer Modeling in Engineering & Sciences*, 125(2), 515–539. <https://doi.org/10.32604/cmes.2020.010165>
- Yang, Y., Nawrocki, R., Voyles, R., & Zhang, H. H. (2021b). A Fractional Drift Diffusion Model for Organic Semiconductor Devices. *CMC-Computers, Materials & Continua*, NA(NA).
- Yang, Y., & Zhang, H. H. (2019). Fractional Calculus with its Applications in Engineering and Technology. In *Synthesis Lectures on Mechanical Engineering* (1 ed., Vol. 3, Issue 1). Morgan & Claypool Publishers LLC. <https://doi.org/10.2200/s00902ed1v01y201902mec017>
- Yuan, Y. (2005). Finite difference fractional step methods for the transient behavior of a semiconductor device. *Acta Mathematica Scientia*, 25(3), 427–438. [https://doi.org/10.1016/s0252-9602\(05\)60006-9](https://doi.org/10.1016/s0252-9602(05)60006-9)
- Yuan, Y., Yang, Q., Li, C., & Sun, T. (2017). Numerical method of mixed finite volume-modified upwind fractional step difference for three-dimensional semiconductor device transient behavior problems. *Acta Mathematica Scientia*, 37(1), 259–279. [https://doi.org/10.1016/S0252-9602\(16\)30129-1](https://doi.org/10.1016/S0252-9602(16)30129-1)
- Zhang, J., Liu, Y., Guo, L., Liu, N., Xiao, H., Chen, C., & Wu, G. (2015). Flexible Oxide-Based Thin-Film Transistors on Plastic Substrates for Logic Applications. *Journal of Materials Science and Technology*, 31(2), 171–174. <https://doi.org/10.1016/j.jmst.2014.07.009>
- Zheng, Q., Chen, D., & Wei, G.-W. (2011). Second-order Poisson Nernst-Planck solver for ion channel transport. *Journal of Computational Physics*, 230(13), 5239–5262. <https://doi.org/10.1016/j.jcp.2011.03.020>

- Zheng, X., Geng, H., Yi, Y., Li, Q., Jiang, Y., Wang, D., & Shuai, Z. (2014). Understanding Lattice Strain-Controlled Charge Transport in Organic Semiconductors: A Computational Study. *Advanced Functional Materials*, 24(35), 5531–5540. <https://doi.org/10.1002/adfm.201400261>
- Zhu, C., Wu, H. C., Nyikayaramba, G., Bao, Z., & Murmann, B. (2019). Intrinsically Stretchable Temperature Sensor Based on Organic Thin-Film Transistors. *IEEE Electron Device Letters*, 40(10), 1630–1633. <https://doi.org/10.1109/LED.2019.2933838>
- Zwicker, G., & Jacobi, K. (1985). Experimental band structure of ZnO. *Solid State Communications*, 54(8), 701–704. [https://doi.org/10.1016/0038-1098\(85\)90591-5](https://doi.org/10.1016/0038-1098(85)90591-5)

## **PUBLICATIONS**

### **Book**

Yang, Y., & Zhang, H. H. (2019). Fractional Calculus with its Applications in Engineering and Technology. Synthesis Lectures on Mechanical Engineering, 3(1), 1–107. <https://doi.org/10.2200/s00902ed1v01y201902mec017>

### **Book chapter**

Yang, Y., Zhang, H. H., & Voyles, R. M. (2019). Rotary inverted pendulum system tracking and stability control based on input-output feedback linearization and PSO-optimized fractional order PID controller. In Automatic Control, Mechatronics and Industrial Engineering (pp. 79–84). CRC Press. <https://doi.org/10.1201/9780429468605-11>

### **Journal publications**

Yang, Y., Nawrocki, R. A., Voyles, R. M., & Zhang, H. H. (2021a). Modeling of the electrical characteristics of an organic field effect transistor in presence of the bending effects. Organic Electronics, 88, 106000. <https://doi.org/10.1016/j.orgel.2020.106000>

Yang, Y., Nawrocki, R., Voyles, R., & H. Zhang, H. (2020). Modeling of an Internal Stress and Strain Distribution of an Inverted Staggered Thin-Film Transistor Based on Two-Dimensional Mass-Spring-Damper Structure. Computer Modeling in Engineering & Sciences, 125(2), 515–539. <https://doi.org/10.32604/cmes.2020.010165>

Yang, Y., Zhang, H. H., Yu, W., & Tan, L. (2020). Optimal design of discrete-time fractional-order PID controller for idle speed control of an IC engine. International Journal of Powertrains, 9(1–2), 79–97. <https://doi.org/10.1504/IJPT.2020.108412>

Yang, Y., & Zhang, H. H. (2018). Stability Study of LQR and Pole-Placement Genetic Algorithm Synthesized Input-Output Feedback Linearization Controllers for a Rotary Inverted Pendulum System. International Journal of Engineering Innovation & Research, 7(1), 2277–5668.

Yang, Y., Nawrocki, R., Voyles, R., & Zhang, H. H. (2021b). A Fractional Drift Diffusion Model for Organic Semiconductor Devices. CMC-Computers, Materials & Continua, (In Press).

### **Conference publications**

Yang, Y., Bai, H., Nawrocki, R., Voyles, R., & Zhang, H. (2021). Fractional Drift-Diffusion Model of Organic Field Effect Transistors Including Effects of Bending Stress for Smart Materials. Proceedings of the ASME 2021 Conference on Smart Materials, Adaptive Structures and Intelligent Systems (In Review).